CHARACTERIZATION AND MODELING OF MICROWAVE SPIRAL INDUCTORS AND TRANSFORMERS

XU DAOXIAN (B. Science)

DEPARTMENT OF ELECTRONICS

PEKING UNIVERSITY, CHINA

A THESIS SUBMITTED

FOR THE DEGREE OF DOCTOR OF PHILOSOPHY

DEPARTMENT OF ELECTRICAL AND COMPUTER ENGINEERING

NATIONAL UNIVERSITY OF SINGAPORE

2005

ACKNOWLEDGEMENT

I would like to express my sincere gratitude to my supervisors, A. Prof. Ooi Ban Leong, Prof. Kooi Pang Shyan, and Dr. Lin Fujiang, for their valuable guidance, advice, and strong support during my postgraduate program. Without their thorough guidance, this thesis would not have been completed.

I am also very grateful to Prof. Xu Qunji for his encouragement and useful discussion.

My gratitude is also extended to my fellow laboratory members, especially for the assistance and the helpful opinions from Mr. Wu Bin, Mr. Sing Cheng Hong, and Mr. Hui So Chi.

Last but not least, I would like to thank my friends and family for their generous support and encouragement throughout my study and research during these years.

CONTENTS

ABSTRACT

Radio frequency (RF) circuits fabricated by monolithic microwave integrated circuit technologies (such as GaAs/silicon MMIC) make extensive use of on-chip transmission lines to realize an inductance, the inductor being a key component in many high-performance circuit designs. In this thesis, several kinds of on-chip microwave spiral inductors are analyzed and modeled.

Some novel predictions of the series resistance and inductance of general spiral inductors are presented for in this thesis. The resistance of the inductor is observed to have an increasing function of frequency, whereas the inductance is a decreasing function of frequency. The non-uniform current in the spiral metallic trace, which is due to skin effect and eddy current, and the effect of ground plane, results in the frequency-dependent behavior for the resistance and inductance of the whole spiral inductor. In this thesis, some closed-form analytical formulae for the resistance and inductance calculations with detailed consideration of skin effect and eddy current are obtained.

In the approaches above, two different methods for the inductance calculation with non-uniform current distribution are also investigated and derived. These two methods, which are mainly based on the magnetic flux and magnetic energy respectively, are presented for the first time. Then, in the modeling of spiral inductor with partial element

equivalent circuit (PEEC) technique, two improved models with eddy current effects are proposed.

In this thesis, a new insight for the criteria of obtaining high *Q*-factor in symmetrical spiral inductors is discussed. These criteria are based on the overlap capacitance effects, and the electric and magnetic center (EMC). Compared with the non-symmetrical spiral inductors, the symmetrical structure can provide a relatively higher quality factor owing to reduced coupling capacitance. This characteristic is explained clearly with the concept of EMC of the spiral inductor.

With the new insight gain, a new equivalent circuit for the two-layer spiral inductors is thus proposed. This circuit incorporates the effect of eddy current of the two-layer spiral inductors in circuit modeling. Some improved expressions for the eddy current in the silicon substrate are also derived.

Finally, the research work is extended to cover the analysis of antenna, microwave transformers, and power dividers. As applications for the spiral inductor, a slot antenna with spiral EBG-fed, a modified EBG Wilkinson power divider, and a new type of transformer based on the balun network, are designed and presented in this thesis.

LIST OF FIGURES

LIST OF TABLES

LIST OF SYMBOLS

ε	Permittivity
ε_0	Permittivity of free space
μ	Permeability
μ_0	Permeability of free space
σ	Conductivity
δ	Skin depth
E	Electrical field intensity
B	Magnetic flux density
ϕ	Magnetic flux
f	Frequency
ω	Angular frequency
L	Inductance
M	Mutual inductance
R	Resistance
Z	Impedance
Y	Admittance
C	Capacitance
Q	Quality factor
i	Current
J	Current density

D	Outer dimension of spiral inductor
d	Inner dimension of spiral inductor
W	Metal width of spiral inductor
T	Metal thickness of spiral inductor
P	Metal pitch of spiral inductor
S	Spacing between the metallic traces of spiral inductor
q	Charge
U	Voltage
Φ	Potential

CHAPTER 1

INTRODUCTION

1.1 Background

During the past few years, more and more microwave design efforts have been focused on integrating voltage-controlled oscillator (VCO) cells, including the passive *LC* tank, into a single chip while achieving low phase-noise performance [1]. To ensure a very low phase-noise signal, the existence of a high-quality *LC* resonator for the VCO is demanded. The quality of the resonator circuit is dominated by the quality factor of the on-chip inductor. Hence, successful design of such a passive device in most of the available technologies remains a major issue.

On-chip microwave spiral inductors generally enhance the reliability and efficiency of silicon-integrated RF cells. They can offer circuit solutions with superior performance and contribute to a higher level of integration [2]-[3]. In low-noise amplifiers (LNA's), microwave integrated inductors can be used to achieve input-impedance matching without deteriorating the noise performance of the cell [4]. They can also be used as loads intending either to improve the gain capability of the amplifier or to reduce its power consumption [5].

The industry has already appreciated the benefits of high-quality integrated inductors and is willing to adapt the existing processes in order to achieve improved inductive elements. The inclusion of Au or Cu metallic layers, the increase of the thickness of metal alloys and dielectric materials, and the increase of the substrate resistivity [6] are among the changes that will help to accomplish quality-factor values of above 15 in silicon technologies. High-*Q*-factor on-chip spiral inductors can give the opportunity to implement reliable on-chip passive RF filters on silicon substrates.

Significant efforts have already been reported [6]-[25] in literature that aim to provide high-*Q*-factor inductors for critical RF applications. During this period, new structures such as 3-dimensional, multi-layer, vertical, and symmetrical inductors, were created. Multi-layer spiral inductor offers an increase in the total inductance, when compared with planar inductor occupying the same area. Through experiments, the symmetrical structure of a spiral inductor shows a relatively higher *Q*-factor than the asymmetrical one.

A first-time success in silicon technology is the ultimate target in every Radio Frequency Integrated Circuit (RF IC) design. This goal becomes more difficult to achieve as the frequency of operation increases. The inclusion of a poorly characterized element such as the integrated inductor in a design turns the whole process to an extremely risky matter. The aim of this work is to minimize the risk, the time, and the cost of the inclusion of integrated inductor structures in silicon RF IC design. This is achieved

through the systematic presentation of the properties and nature of the integrated spiral inductors, as well as the numerous design cases, parametric evaluation, and nomographs that will allow the engineer to gain insight in Si inductors.

1.2 Literature Review, Research Motivation, and Goals

1.2.1 Circuit Modeling for Microwave Spiral Inductors

In conventional IC technologies, inductors are not considered as standard components like transistors, resistors, or capacitors, whose equivalent circuit models are usually included in the process description. However, this situation is rapidly changing as the demand for RF IC's continues to grow [17], [20], and [26]-[28]. So, an accurate model for on-chip inductors is of great importance for silicon-based radio-frequency integrated circuits designers. Various approaches for modeling inductors on silicon have been reported in the past several years [29]-[46]. Most of these models are based on numerical techniques, curve fitting, or empirical formulae, and are therefore relatively inaccurate or not scalable over a wide range of layout dimensions and process parameters.

To gain a greater insight into the design of the spiral inductor, a compact, physical model is required. The partial element equivalent circuit (PEEC) technique has been applied successfully for many years to model the electrical properties of high-speed interconnect [36]-[38] and found suitable for the spiral inductor modeling [39]. The circuit model introduced firstly in references [40]-[41] presents the good physical inductor model, which maintains the relevant parasitic and their detailed effects. Then in

[42], another modified circuit model, in which some additional components were added, was introduced. The added components in the modified circuit model represent the loss mechanism of the substrate of spiral inductors.

A frequency-dependent circuit model is required by incorporating the eddy current effect for the spiral inductors. This is one of the most important goals for our research.

1.2.2 Series Resistance of Spiral Inductor with Current Redistribution

Spiral inductors implemented in silicon processes suffer from several power dissipation mechanisms, leading to poor inductor quality factor. The mechanisms include (*a*) I^2R losses from eddy current circulating below the spiral inductor in the semiconducting substrate, (*b*) from displacement current conducted through the turn-to-substrate capacitances and (*c*) the underlying substrate material, and (*d*) from the primary inductor current flowing through the thin metallic traces of the inductor itself [32], and [47]-[49]. Spiral inductors built by bipolar processes (or bipolar-derived BiCMOS) often exhibit higher *Q*-factor values (typically five to ten). This is mainly due to the relatively high substrate resistivities (e.g., $10-30\Omega-cm$), which reduce the eddy current but may still suffer from significant losses from the displacement current conducted through turn-to-substrate capacitances [27] and [32]. These losses can be mitigated by the introduction of a patterned ground shield [6] and [50] or by an umpatterned shield of the proper sheet resistance placed below the inductor [51], of course both at the expense of reduced self-resonance frequency.

The best approach to produce high-quality inductors in silicon involves (*a*) etching away the offending semiconducting material below the spiral inductor [7], (*b*) using a thick oxide layer to separate the spiral inductor from the substrate [23] and [52], (*c*) using a very high resistivity bulk [30], or (*d*) using an insulating substrate such as sapphire [53]. In some of these cases, inductor *Q*-factors of 20 or above were reported, with the highest values found in single turn spiral inductors with the inductance values of less than 5nH.

Unfortunately, for spiral inductors with higher inductances, multiple turns are required and the *Q*-factor often falls and is lower than the value that would be predicted from a simple calculation of inductor reactance divided by *dc* series resistance. The limitation on *Q*-factor can be traced to an increase in effective resistance of the metallic trace at high frequencies due to the phenomenon of current redistribution [22] and [45].

The concept of current redistribution in the metallic trace of spiral inductor can mainly be traced from two aspects: skin effect and eddy current. Skin effect is the universal phenomenon in RF IC, and eddy current, which leads to the current crowding, is also well-known and the general mechanisms involved were cited and elucidated in several papers, such as references [22], and [45]-[46]. But little information is available in the literature to quantitatively predict the eddy current without resorting to numerical simulations [46]. The authors of [2] developed a first-order analytical model for the major current crowding mechanisms and derived some useful approximate formulae for calculating the eddy current.

In [41], a physical expression of the series resistance of a spiral inductor with skin effect was proposed and given as

$$R = \rho l / W T_{eff} , \tag{1.1}$$

where ρ, W, and l represent the resistivity, metallic width, and total length of the spiral inductor, respectively. T_{eff} is defined as an effective thickness:

$$T_{eff} = \delta(1 - e^{-T/\delta}), \tag{1.2}$$

where T and δ represent respectively the metal thickness and the skin depth. For frequencies below 2GHz, the skin depth effects are relatively small in most processes since the trace metal thickness is typically less than or equal to the skin depth. Above 2GHz, the alternating current (*ac*) resistance increases and approaches an asymptote proportional to the square root of frequency. In contrast to the skin effect in high frequency range, current crowding (eddy current in the metallic trace of the spiral inductor) is a strong function of frequency, resulting in an increasing resistance function and a concaving downward *Q*-factor function.

Kuhn's formulae in [2] provided a series of improved expressions, incorporating the eddy current, for the prediction of series resistance of a spiral inductor. But the skin effect on the resistance was neglected in the estimation. In our approach, we will provide some more accurate expressions of resistance with both the skin effect and the eddy current in spiral inductors.

1.2.3 Series Inductance of Spiral Inductor with Current Redistribution

Since an inductor is intended for storing magnetic energy only, an ideal expression of its inductance in terms of width, gap spacing and length is essential in terms of equivalent circuit modeling. A very accurate numerical solution can be obtained by using a three-dimensional (3-D) finite-element simulator such as MagNet [54], but 3-D simulators are computationally intensive and time-consuming. Other techniques for analysis include the Greenhouse method [40] and [55], Wheeler formula [56], and "Data Fitted Monomial Expression" [57]. Data fitted expressions usually lack the precise theoretical interpretation, while physical foundation for computing inductance is built on the concept of the self-inductance of a wire and the mutual inductance between a pair of wires.

The total inductance of a spiral inductor can be separated into two aspects, the self- and mutual inductances. A comprehensive collection of formulae and tables for inductance calculation was summarized by Grover in [58].

The partial inductance method has been widely applied to the calculation of inductance of spiral inductors [40]. The concept and computation of partial inductances were described in [59], and the working formulae were given elsewhere. Partial inductances conceptually involve magnetic flux between a conductor and infinity. This aspect presents obvious problems in structures of infinite length such as the conventional transmission line. Perhaps the most important quality of the partial inductance concept is the ability to break a complicated three dimensional problem into its constituent interactions. A very simple example of a loop and its partial inductances is given in Fig.

1.1. The equivalent circuit of the loop in Fig. 1.1 is specified in terms of partial inductances L_{ii} of the *i*-th segment and L_{ij} between the *i*-th and the *j*-th segments. If the loop is closed so that $I_1 = I_2 = I_3 = I_4$, then the total loop inductance can be obtained with conventional circuit theory as

$$L = \sum_{m=1}^{4}\sum_{n=1}^{4} L_{mn}. \tag{1.3}$$

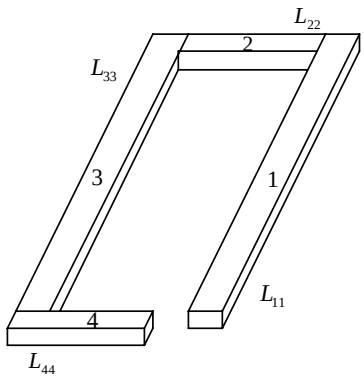

Fig. 1.1: Loop and partial inductance.

The mutual partial inductance can often be approximated for realistically spaced conductors by resolving the conductor cross sections into filaments and summing the results as

$$L_{ij} = \frac{1}{n_i n_j}\sum_{i=1}^{n_i}\sum_{j=1}^{n_j} L_{fij}, \tag{1.4}$$

where L_{fij} is the mutual inductance between the filaments.

The typical formula for the calculation of inductance of spiral inductor is [41]

$$L_{total} = L_{self} + M = 2l(\ln\frac{2l}{W+T} + 0.5 + \frac{W+T}{3l}) + 2lX, \tag{1.5}$$

where *l*, *W*, and *T* represent the total length, metal width, and metal thickness of the spiral inductor. *X* is the mutual inductance parameter, which can be computed using

$$X = \ln\left[\frac{l}{GMD} + \sqrt{1+(\frac{l}{GMD})^2}\right] - \sqrt{1+(\frac{l}{GMD})^2} + \frac{GMD}{l}. \qquad (1.6)$$

In equation (1.6), GMD denotes the geometric mean distance between the wires, which is approximately equal to the pitch of the wires. A more precise expression for the GMD is given as

$$\ln GMD = \ln P - \frac{W^2}{12P^2} - \frac{W^4}{60P^4} - \frac{W^6}{168P^6} - \frac{W^8}{360P^8} - \frac{W^{10}}{660P^{10}} - \cdots, \qquad (1.7)$$

where P is the inductor pitch. A commonly adopted assumption in the previous reported works on calculating inductance is that they usually neglected the frequency dependence of the inductance.

But, as eddy current and skin effect result in non-uniform current distribution in the metallic trace, the inductance of the trace may no longer be frequency-independent. Thus, we need to add to the redistributed magnetic flux the individual current element's contribution in order to achieve better inductance expressions for the spiral inductors.

Furthermore, when a current is established in a circuit or element of a circuit, the rise of current will induce an electromotive force that opposes the rise of current. Thus, energy has to be expended by the source, in order to keep the current flowing against the induced electromotive force. Similar phenomena will also occur for multi-circuit/element conditions with uniform current assumption in the circuits. The relationship between the total stored magnetic energy and the circuit inductance was proposed in [58]. As a result, we can introduce and expand the energy method into the non-uniform current distribution

conditions (as discussed previously) and establish a new type of inductance calculation method for the microwave spiral inductors.

1.2.4 High *Q*-factor Symmetrical Spiral Inductors

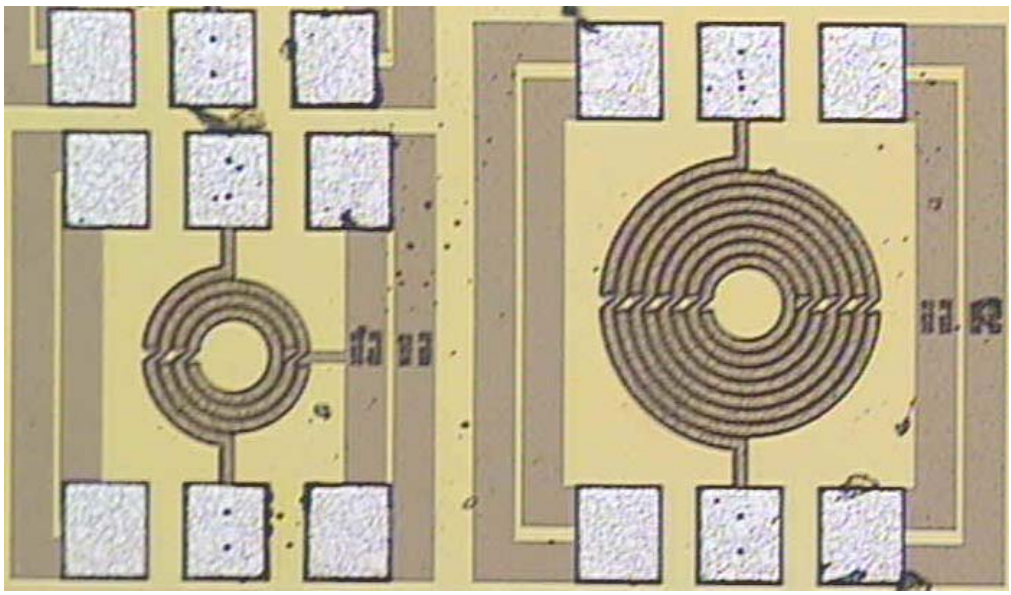

Fig. 1.2: Photograph of circular symmetrical spiral inductors.

At radio frequency (RF), the usage of on-chip silicon spiral inductors in *LC* tank circuits is limited by the achievable quality factor (*Q*). The quality factor is seriously affected by three major components. They are the crossover capacitance, the capacitance between the spiral trace and the substrate, and lastly, the substrate capacitance. In the physical modeling of an inductor [60]-[66], the series feed-forward capacitance results from the capacitance due to the overlaps between the spiral trace and the underpass [6] and [67].

To increase the overall *Q*-factor of the silicon spiral inductors, symmetrical spiral inductors (as shown in Fig. 1.2) are usually used, instead of the conventional, non-symmetrical spiral inductors. Although there were some detailed *Q*-factor expressions for

the conventional spiral inductors presented in [6], the detailed mechanism of how the symmetrical, arbitrarily-shaped spiral inductors can achieve high *Q*-factors about 6-7 is still a mystery. In our research, we attempt to provide a comprehensive explanation for why the symmetrical, arbitrarily-shaped spiral inductors help to improve the *Q*-factor characteristics over that of the corresponding conventional, non-symmetrical spiral inductors.

1.2.5 Multi-layer Spiral Inductors

Multi-layer inductors, especially in the form of spirals, have gained great importance in the design of integrated silicon RF transmitters and receivers [3], [17], [64], and [68]-[74]. The application of multi-layer inductors can provide a relatively higher *Q*-factor than single-layer inductors with the same inductance values [64]. And on the other hand, multi-layer spiral inductors were shown to offer an increase in the total inductance and maintain the same *Q*-factor, when compared to planar ones occupying the same areas [64], and [75]-[78].

The substrate effects on the performance of metal-insulator-metal (MIM) spiral inductors are critical to silicon RF IC's [51], and [80]-[82]. Their effects of substrate RF losses from the eddy current (displacement current) on the characteristics of silicon-based integrated inductors and transformers were studied experimentally in [80] and [83]. The purpose of my research is to numerically display the effects of the eddy current in the

substrate and incorporate them into the equivalent circuit model in the case of multilevel-spiral (MLS) inductors.

The most commonly used spiral inductor compact model is the standard “9-element” model [41]. In the research, a more accurate equivalent circuit for two-layer spiral inductors, particularly suited to be used in the design of RFIC’s, is presented. The contributions of the metallic traces and the eddy current in the substrate to the overall effects of the spiral inductors are modeled respectively in the circuit model.

1.2.6 EBG, Power Dividers, and Transformers

The theory of photonic band-gap (PBG) or electromagnetic band-gap (EBG) was developed initially for optical frequencies and can easily be applied to millimeters waves, microwaves, and antennas. Generally, EBG can diminish the propagation constant causing the wave to move slowly. Thus, they can be integrated into antenna and power divider designs.

Transformers have been widely used in RF circuits since the early days of telegraphy [84]. The operation of a passive transformer is based on the mutual inductance between two or more conductors, or windings (spiral metallic turns). Multifilament transformers can also be constructed on-chip and used to implement baluns and power dividers [84].

Coupled lines are useful and widely applied structures that provide the basis for many types of balun. The most commonly used balun is called Marchand balun [85] which is important in realizing balanced mixers [86]-[87], amplifiers, and phase shifters [88]-[92] by providing differential signals. The principle of operation of the Marchand balun was explained in literature in [85].

The well-known Wilkinson power divider and combiner are being used for the design of microwave power amplifiers [93]. Both the divider and the combiner have the same structure, which consists of two $\lambda/4$ branches and a termination resistor, where the λ is the wavelength of the transmission line. However, if the divider branches are made of normal transmission lines, the $\lambda/4$ length usually limits the minimum size of the power divider at low operating frequencies.

These motivate us to use the broadside coupling method (between top and bottom layers) of baluns to design a new type of LTCC transformer or power divider with coupling spiral inductors in different metallic layers. In this application design, the transmission lines in the conventional Wilkinson power divider are replaced by coupled spiral metallic lines and they can help to reduce the total area needed for the device.

1.3 Organization of the Thesis

This thesis is divided into seven chapters. Chapter 1 provides an introduction to the general microwave spiral inductors, symmetrical spiral inductors, and multi-layer spiral

inductors. Some original contributions and publications are also highlighted in this chapter.

In Chapter 2, an improved expression incorporating both skin effect and eddy current for the prediction of series resistance in the spiral inductor model is derived. Furthermore, two more accurate circuit models for the monolithic spiral inductors are also proposed with the PEEC technique. Better simulation results are confirmed by experimental data with our improved models.

In Chapter 3, with the partial inductance method, some improved expressions for the prediction of inductance for spiral inductor with non-uniform current distribution are derived. An alternate energy method that takes into account the non-uniform current distribution is also presented. These two methods for calculating the inductance are thus compared. In addition, the internal inductances of the metallic trace and the ground plane of the spiral inductor are analyzed in Chapter 3.

In Chapter 4, we provide a comprehensive explanation on how the symmetrical, arbitrarily-shaped spiral inductor helps to improve the *Q*-factor characteristics over that of the corresponding conventional, non-symmetrical spiral inductor. Our predictions on the high *Q*-factor symmetrical inductors are also confirmed by extensive simulation results.

In Chapter 5, we present a more accurate equivalent circuit for two-layer spiral inductors, particularly suited to be used in the design of RFIC's. The contributions of the metallic trace and the eddy current in the substrate to the overall effects of the inductor are modeled respectively by different parts in the circuit model. Our proposed equivalent circuit is validated by experimental data of a series of two-layer spiral inductors on silicon substrate, and the results are reported in this chapter.

In Chapter 6, we present a series of applications, including a modified triple-band slot antenna with EBG-fed, a modified EBG-fed CPW Wilkinson power divider, and a new type of transformer with spiral inductor traces which can provide well-balanced output signals. The slot antenna with EBG-fed can provide wider bandwidths than the conventional reference antenna. The new type of low-loss transformer can be used in the design of microwave power dividers or combiners. The return losses, insertion losses, and imbalance characters of it are in turn presented and analyzed.

Finally, in Chapter 7, some important conclusions and future works are drawn.

1.4 Original Contributions

In this thesis, we present a series of more accurate expressions for calculating the series resistances of spiral inductors by incorporating skin effect and eddy current effects. Two novel circuit models for spiral inductors are proposed with eddy current effects. Furthermore, the energy method is also improved to calculate the inductance with non-

uniform current distributions for spiral inductors. In our investigation, the internal inductances of the metallic trace and the ground plane are also included.

We also provide a comprehensive explanation on how the symmetrical, arbitrarily-shaped spiral inductor is able to improve the *Q*-factor characteristics over that of the corresponding conventional, non-symmetrical spiral inductor.

An improved equivalent circuit for the two-layer spiral inductors on silicon substrate, which incorporates the effects of eddy current in the substrate, is presented.

EBG, which can improve the device performances, is utilized in the designs of a triple-band slot antenna and a CPW Wilkinson power divider. Another type of modified transformer with spiral metallic traces, which can provide excellent balanced signals, is analyzed and their effects are demonstrated in this thesis.

The contributions made in my research are reported in the following publications:

1.4.1 Book Chapter

Ban-Leong Ooi and Dao-Xian Xu, *Encyclopedia of RF and Microwave Engineering*, John Wiley & Sons, Inc, 2004.

1.4.2 Journals

(1) Ban-Leong Ooi, Dao-Xian Xu, Pang-Shyan Kooi, and Fu-Jiang Lin, “An improved prediction of series resistances in spiral inductor modeling with eddy-current effect,” *IEEE Trans. Microwave Theory Tech.*, vol. 50, no. 9, pp. 2202-2206, Sep. 2002.

(2) B.-L. Ooi and D.-X. Xu, “Modified inductance calculation with current redistribution in spiral inductors,” *IEE Proceedings-Microwaves, Antennas and Propagation,* vol. 150, no. 6, pp. 445-450, Dec. 2003.

(3) Ban-Leong Ooi and Dao-Xian Xu, “A novel equivalent circuit model for two-layered spiral inductor with eddy-current effect in the substrate,” *Microwave and Optical Technology Letters,* vol. 40, no. 5, pp. 484-487, Mar. 20, 2004.

(4) Ban-Leong Ooi, Dao-Xian Xu, and Li-Hui Guo, “Efficient methods for inductance calculation with special emphasis on non-uniform current distributions,” *Microwave and Optical Technology Letters,* vol. 40, no. 5, pp. 432-436, Mar. 5, 2004.

(5) Ban-Leong Ooi, Dao-Xian Xu, Bin Wu, and Bo Chen, “A novel LTCC power combiner,” *Microwave and Optical Technology Letters,* vol. 42, no. 3, pp. 255-257, Aug. 5, 2004.

(6) Ban-Leong Ooi, Dao-Xian Xu, and Pang-Shyan Kooi, “Detailed analysis of high quality characteristics symmetrical octagonal spiral inductor on Si substrate,” *International Journal of RF and Microwave Computer-Aided Engineering,* vol. 15, no. 2, pp. 181-186, Mar. 2005.

1.4.3 Conferences

(1) Ban-Leong Ooi, Dao-Xian, Xu, Pang-Shyan Kooi, Fu-Jiang Lin, and So-Chi Hui, "Modified Inductance calculation with current redistribution in spiral inductors," *Proc. of 2002* 3*rd International Conference on Microwave and Millimeter Wave Technology Proceedings*, pp. 705-708, Aug. 2002.

(2) Ban-Leong Ooi, Dao-Xian Xu, and Pang-Shyan Kooi, "A comprehensive explanation on the high quality characteristics of symmetrical octagonal spiral inductor," *2003 IEEE Radio Frequency Integrated Circuit (RFIC) Symposium*, pp. 259-262, June 2003.

(3) Ooi Ban Leong, Daoxian Xu, and Guang Zhao, "A novel type of two-layer power divider based on the LTCC balun network design," *Proc. of 2004 Progress in Electromagnetics Research Symposium*, pp. 259, Nanjing, China, August 28-31, 2004.

(4) Ooi Ban Leong and Daoxian Xu, "Efficient methods for inductance calculation with non-uniform current distributions in spiral inductor," *Ninth International Conference on Communication Systems*, Singapore, Sept. 6-9, 2004.

(5) B. L. Ooi, X. D. Xu, and Irena Ang, "Triple-band slot antenna with spiral EBG feed," *2005 IEEE International Workshop on Antenna Technology*, pp. 329-332, Singapore, Mar. 7-9, 2005.

CHAPTER 2

IMPROVED MODELING AND PREDICTIONS OF RESISTANCE FOR SPIRAL INDUCTORS WITH EDDY CURRENT EFFECTS

2.1 Calculation of Eddy Current

Current crowding comes from the current redistribution due to the *B*-field of adjacent turn which induces eddy current. Non-uniform current distribution has been identified for those segments close to the center of the microwave spiral inductors [45].

The overall shape of the *B*-field value is a linear increase from a negative value on the outside turn to a positive peak on the inside turn. Simplified expression for the average normal *B*-field in terms of *n* (numbering from *n* = 1 at the outside turn) is given as [2]

$$B(n) \approx B_0\left(\frac{n-N_0}{N-N_0}\right) \approx 0.65\frac{\mu_0}{P} I_{ex}\left(\frac{n-N_0}{N-N_0}\right). \quad (2.1)$$

Herein, N is the total number of turns, B_0 is the field at the innermost turn (N), N_0 is the turn number where the B-field falls to zero and reverses direction, μ_0 is the permeability of free space, P is the turn pitch as illustrated in Fig. 2.1, and I_{ex} refers to the excitation current.

Although the numerically computed data shows that the B-field is approximately linear across each lateral metallic trace, the assumption of B as a function of n only will simplify the subsequent analysis as we only pay attention to the integration value across each whole trace [2].

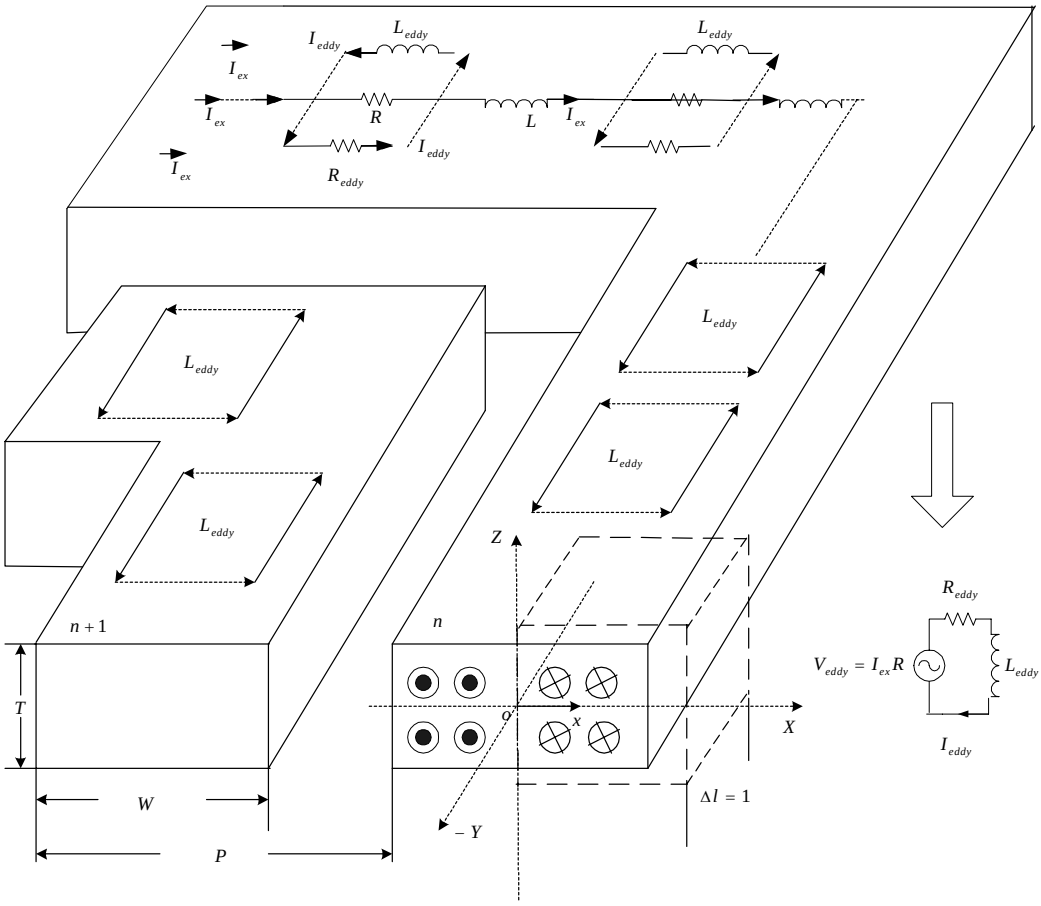

Fig. 2.1: Simplified illustration of eddy current effects.

For on-chip spiral inductors, the line segments can be treated as microstrip transmission lines, as shown in Fig. 2.1. In this case, the high frequency current recedes to the surface of the wire, which is above the ground plane [32] and [34]. The attenuation of the current density (J in A/m^2) as a function of distance (z) away from the surface can be expressed by the function [41]:

$$J = \begin{cases} J_0 e^{(z-T/2)/\delta}, T/2 \geq z \geq 0 \\ J_0 e^{(-z-T/2)/\delta}, 0 \geq z \geq -T/2 \end{cases}. \quad (2.2)$$

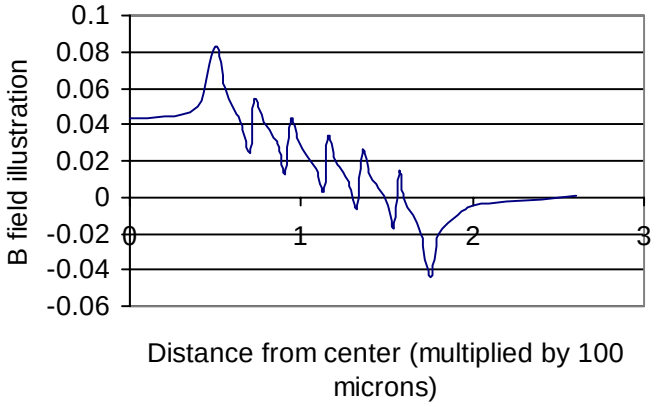

Fig. 2.2: Calculated *B*-field on a square spiral inductor with a totally 1A *dc* current (*N*=6, *W*=18 μm, *P*=21 μm, and *D*=350 μm) (after [2]).

Using Maxwell law, namely $\nabla \times \overline{E} = -j\omega\overline{B}$, and $\overline{J} = \sigma\overline{E}$, we obtain

$$\left|I_{eddy}\right| = 2\int_0^{T/2}\int_0^{W/2} \omega\sigma B(n) x e^{(z-T/2)/\delta} dx dz = 0.162\omega\sigma W^2 I_{ex}\delta(1-e^{-T/2\delta})\frac{\mu_0\left|n-N_0\right|}{P(N-N_0)}, \quad (2.3)$$

where T is the metal thickness, W is the metal width, δ refers to the skin depth ($\sqrt{2/\omega\sigma\mu}$), and σ and μ are the conductivity and permeability of the metallic trace respectively. D is the outer dimension of the inductor. Numerically computed data of the *B*-field is used to describe the initial field domain on the upper surface of the inductor trace (z=T/2). Here, we assume that current is concentrating mainly in the domain near to

the surface of the metallic trace, while the current distribution along the *x* direction is roughly approximated by a linear expression as in equation (2.3) (see in Fig. 2.1).

Assuming that the frequency is high enough, the skin depth δ will be small compared with the thickness *T*, so that the term $(1-e^{-T/2\delta})$ in equation (2.3) can be neglected. As the expression reaches its maximum at the innermost turn (*n* = *N*), it is easy to find the frequency ω' at which the current crowding begins to become significant ($\left|I_{eddy}\right| = I_{ex}$):

$$\omega' = 19.1\frac{P^2\mu}{W^4{\mu_0}^2\sigma} \approx 19.1\frac{P^2}{W^4\mu_0\sigma}. \tag{2.4}$$

For example, for a gold-traced inductor ($\sigma = 4.098\times10^7 S/m$) with metal width and pitch values being $10\mu m$ and $15\mu m$ respectively, equation (2.3) reveals that the current crowding occurs significantly at about 8-9GHz. At lower frequencies, we obtain

$$\left|I_{eddy}\right| \propto \omega\delta(1-e^{-T/2\delta}) \propto \sqrt{\omega}(1-e^{-\sqrt{2\omega\sigma\mu}T^2}). \tag{2.5}$$

This means that the effect of the frequency on the phenomenon of eddy current is monotonic.

2.2 Calculation of the Total Resistance

So long as the eddy current exists, it will cause the electrical transmission loss through the metallic trace to increase the whole device's equivalent resistance. To match the

result of current crowding, we assume the direction of eddy loop on the inner edge of the metallic trace coincides with the initial excitation current, and then consider the phase difference between them in the next step.

The power dissipated in the *n*-th turn due to the eddy current is

$$P_{eddy\cdot n} = 4\sigma l_n \omega^2 B^2(n) \cdot \int_0^{T/2}\int_0^{W/2} x^2 e^{2(z-T/2)/\delta} dxdz = \frac{1}{12}\sigma l_n \omega^2 B^2(n) W^3 \delta(1-e^{-T/\delta}), \quad (2.6)$$

where l_n is the length of the *n*-th turn. Here, the small difference between the lengths of the eddy loop's outer and inner edges near each trace corner is neglected.

To describe approximately the eddy current, reference [2] estimated each closed current loop as a circuit constituted with L_{eddy}, which develops back electromotive force, and R_{eddy}, which represents the net resistance through which this current flows. Taking the ratio of ωL_{eddy} to R_{eddy} gives an estimation for the phase relationship θ between I_{eddy} and I_{ex}. Details of the ideal circuit for this analysis are illustrated in Fig. 2.1 and the section below.

The total power dissipated in the inner half of the *n*-th turn is

$$P_{n\cdot inner} = P_{ex\cdot n}/2 + P_{eddy\cdot n}/2 + 2\sqrt{\cos\theta}\sqrt{P_{ex\cdot n}/2}\sqrt{P_{eddy\cdot n}/2}, \quad (2.7)$$

and in the outer half, it is given as

$$P_{n\cdot outer} = P_{ex\cdot n}/2 + P_{eddy\cdot n}/2 - 2\sqrt{\cos\theta}\sqrt{P_{ex\cdot n}/2}\sqrt{P_{eddy\cdot n}/2}, \quad (2.8)$$

where θ is the phase difference between I_{eddy} and I_{ex}.

Approximately, the turn number n has no significant influence on the phase difference between I_{eddy} and I_{ex}. So, the total power dissipated in the n-th turn is

$$P_n = P_{n\cdot inner} + P_{n\cdot outer} = P_{ex\cdot n} + P_{eddy\cdot n}. \tag{2.9}$$

Combining equations (2.1), (2.6), and

$$P_{ex\cdot n} = I_{ex}^2 R_n = I_{ex\cdot n}^2 \frac{l_n}{\sigma W T}, \tag{2.10}$$

where R_n is the initially considered resistance of the n-th turn at *dc*, we obtain

$$P_n \approx I_{ex}^2 R_n \cdot \left[1 + 0.14 W^4 T (1 - e^{-T/\delta}) \frac{\mu_0^2 (n - N_0)^2}{\mu^2 \delta^3 P^2 (N - N_0)^2} \right]. \tag{2.11}$$

By summing over n for equation (2.9) and comparing with

$$P_{total} = I_{ex}^2 R_{total}, \tag{2.12}$$

the total spiral resistance R_{total} is obtained:

$$R_{total} = R_0 + 0.05 W^4 T \sigma^{3/2} \frac{\mu_0^2}{\mu^{1/2} P^2} \sum_{n=1}^{N} \frac{R_n (n - N_0)^2}{(N - N_0)^2} \omega^{3/2} (1 - e^{-\sqrt{T^2 \mu \sigma \omega / 2}}). \tag{2.13}$$

In order to have a rough review of the ω dependence of R_{total} at high frequencies, we again neglect the term $(1 - e^{-\sqrt{T^2 \mu \sigma \omega / 2}})$ in equation (2.13) and obtain

$$R_{total} = R_0 + a \omega^{3/2}, \tag{2.14}$$

and

$$a = 0.05 W^4 T \sigma^{3/2} \frac{\mu_0^2}{\mu^{1/2} P^2} \sum_{n=1}^{N} R_n \frac{(n - N_0)^2}{(N - N_0)^2}. \tag{2.15}$$

At relatively lower frequencies when the skin depth δ cannot be neglected compared with the metal thickness *T*, by using the Taylor's formula for the term $(1-e^{-\sqrt{T^2\mu\sigma\omega/2}})$, we have

$$R_{total} \approx R_0 + b\omega^2, \tag{2.16}$$

and

$$b = 0.035W^4T^2\sigma^2\frac{\mu_0^2}{P^2}\sum_{n=1}^{N}R_n\frac{(n-N_0)^2}{(N-N_0)^2}. \tag{2.17}$$

Herein, $R_0 = \sum_n l_n \Big/ \sigma WT$ is the theoretical resistance of the whole spiral trace at *dc*, $\sum_n l_n$ is the total length of the metallic trace, and *a* and *b* are constant for fixed inductors.

2.3 Circuit Modeling of Spiral inductors

2.3.1 The Partial Element Equivalent Circuit (PEEC)

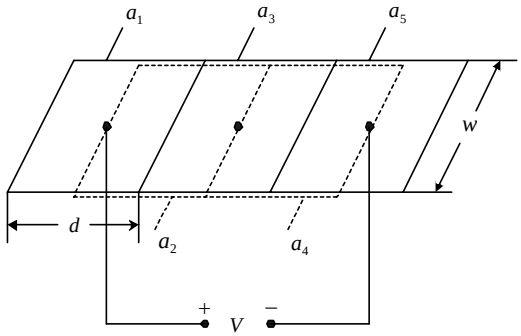

Fig. 2.3: The basic PEEC example. The example shows a part of a flat wire subdivided into three capacitive and two inductive PEEC lumps. The three solid rectangles are the capacitive cells and the two dashed ones are the inductive cells. The black dots are the circuit nodes after [36].

The key to accurate physical modeling is the ability to identify the relevant parasitics and their effects. The PEEC technique is found suitable for the spiral inductor modeling. It is

a circuit based on formulation which is numerically equivalent to a full-wave method of moments solution with the Galerkin matching procedure [59] and [94].

For a simple PEEC example in [36] as shown in Fig. 2.3, it consists only of infinitely thin conductors. Despite its simplicity, it contains all the couplings and therefore easily generalizes. Fig. 2.3 depicts a small fraction of an infinitely thin straight trace (flat wire) which is subdivided into two inductive and three capacitive cells. As usual in a PEEC model, we assume that the three capacitive cells a_1, a_3, and a_5 each has a potential $\Phi_1(t)$, $\Phi_3(t)$, and $\Phi_5(t)$ and a charge $q_1(t)$, $q_3(t)$, and $q_5(t)$, respectively. The two inductive cells a_2 and a_4 on the other hand have uniform currents, $i_2(t)$ and $i_4(t)$. A voltage is impressed on the wire at the ends of the two inductive cells that coincide with the centers of the outer capacitive cells [94]-[97].

The corresponding PEEC model is shown in Fig. 2.4 where the circuit elements are calculated from two independent quasi-static solutions of Maxwell's equation, one involving the capacitive cells and one involving the inductive cells. Conductors are assumed to have zero resistivity, otherwise resistances would be connected in series with the inductances. The proof in [36] showed that the circuit in Fig. 2.4 is equivalent to the unretarded Maxwell's equations except for the approximations introduced by the grid size.

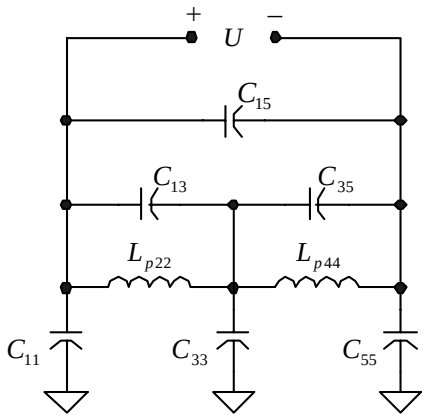

Fig. 2.4: The PEEC model for the basic example as shown in Fig. 2.3. The partial mutual coupling between L_{p22} and L_{p44} is not shown after [36].

With detailed calculations of equations (1) to (19) in [36], Fig. 2.4 provides a good circuit approximation for the example conductor in Fig. 2.3 for all frequencies including very low ones and *dc* current. Furthermore, with those discussions about the PEEC method [36]-[39], it can be widely used and expanded in the circuit modeling with proper simplifications for the spiral inductors in the section below and the following chapters.

2.3.2 Circuit Model Improvement with the Eddy Current Effects

Since an inductor is intended for storing magnetic energy only, the inevitable resistance and capacitance in a real spiral inductor are counter-productive and thus are considered parasitics. The parasitic resistances dissipate energy through ohmic loss while the parasitic capacitances store electric energy. With the PEEC technique above, the simplified physical models of spiral inductors on GaAs or silicon substrate are shown in Fig. 2.5. The inductance and resistance of the spiral inductor and underpass are represented by the series inductance L_s and the series resistance R_s, respectively. C_s

refers to the series capacitance. Other components in the circuits are modeled to represent the effects of substrate [41]. Further details of the circuit components will be explained in Chapter 4.

Our approach is to present the eddy current as electrical component by modifying the conventional circuit model as described in section 2.1. In [2], the method for a two-wire transmission line is used and this technique involves a useful first-order estimation for the relatively complex eddy loop situation within the excitation current as illustrated in Fig. 2.1. The expressions are

$$L_{eddy\cdot n} \approx \frac{\mu_0}{\pi} \ln(\frac{W/4}{W}) l_n, \quad R_{eddy\cdot n} \approx \frac{2}{\sigma TW/4} l_n, \tag{2.18}$$

where the subscript *n* refers to the number of turn.

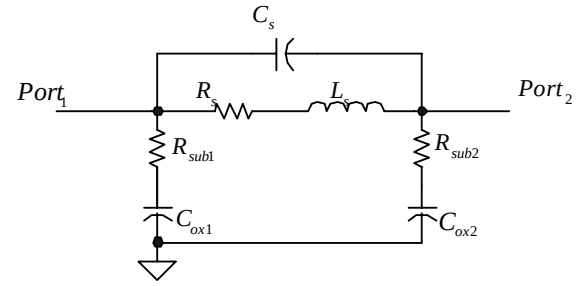

(*a*)

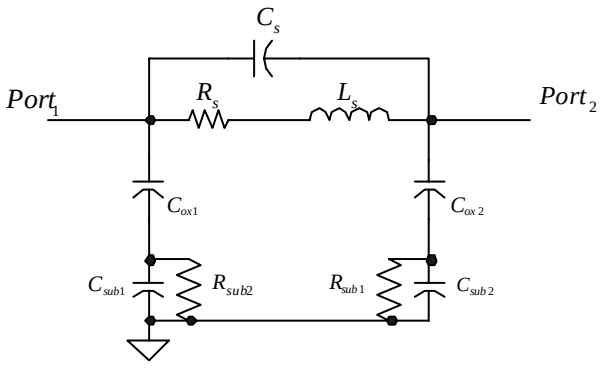

(*b*)

Fig. 2.5: Conventional circuit models for spiral inductors.

The field changing in each turn *n* is certainly more sensitive due to the current in that turn itself than in those adjacent turns or more distant ones. If we assume that the source of the eddy loop is induced by the excitation current, the ratio of R_{eddy} to L_{eddy} represents a constant degree of phase delay from the eddy current to the excitation current. Thus, regardless of the turn number *n*, an overall review of the eddy current effects on the two-port transmission network of inductor can provide us an idea to implement the conventional circuit model, as shown in Fig. 2.6.

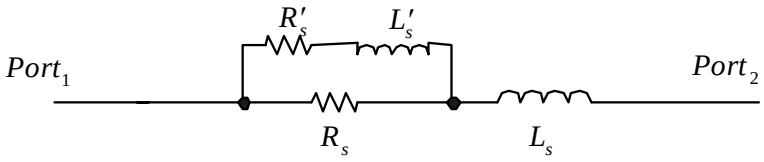

Fig. 2.6: Illustration of modified part after de-embedding.

The branch, constituted by series L'_s and R'_s and in parallel with R_s, is initially assumed as circuit elements contributing to the overall eddy current effects. The voltage over R_s represents the total voltage effect of each eddy current segment induced. Compared with the conventional spiral inductor models as shown in Fig. 2.5, the new model has some significant advantages.

By circuit theory, the input impedance of the network in Fig. 2.6 can be computed as

$$\mathrm{Re}(Z_{in}) = R_s - \frac{R_s^2 \times (R_s + R'_s)}{(R_s + R'_s)^2 + \omega^2 \times L_s'^2}, \tag{2.19}$$

$$\mathrm{Im}(Z_{in})/\omega = L_s + \frac{R_s^{\,2} \times L_s'}{(R_s + R_s')^2 + \omega^2 \times L_s'^{\,2}}, \tag{2.20}$$

where Z_{in} is the input impedance of the spiral inductor.

Equations (2.19) and (2.20) describe the resistance and inductance variations due to the existence of eddy current with an increase of frequency. It overcomes the limit of the conventional circuit models which offer constant input impedances after de-embedding. Detailed steps and further discussions will be shown in the following section.

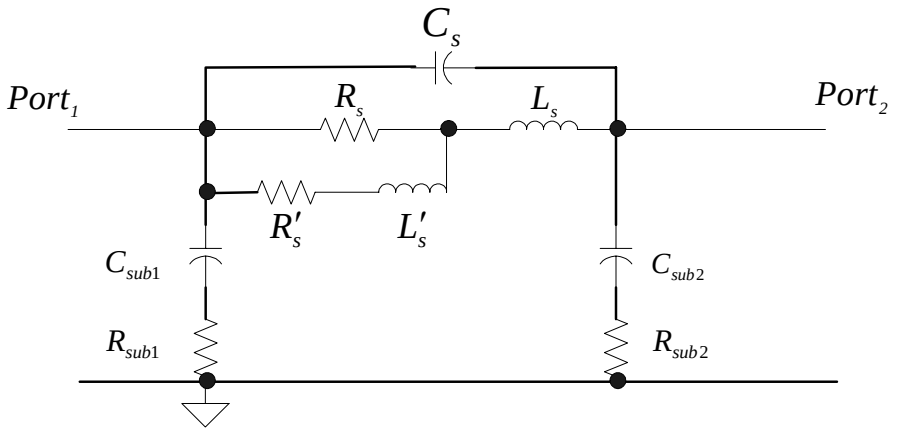

(*a*)

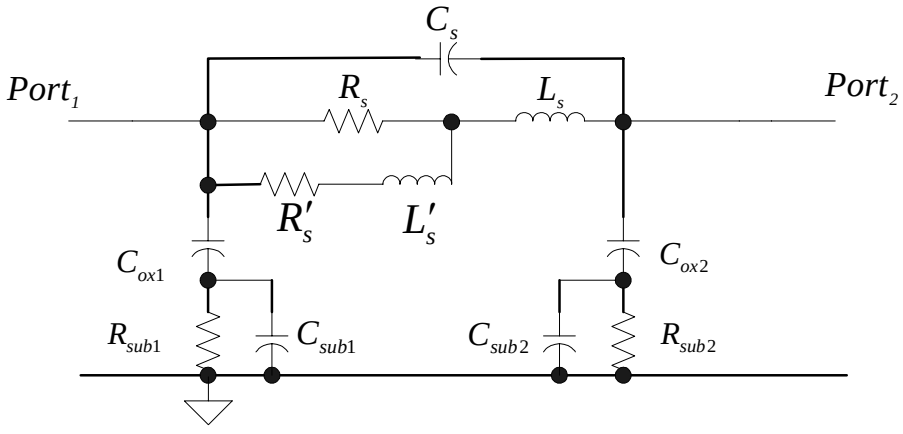

(*b*)

Fig. 2.7: Modified circuit models for spiral inductor.

With the idea of adding an additional branch to model the effects of eddy current in the circuit model as shown in Fig. 2.6, we can thus modify the conventional circuit models (as shown in Fig. 2.5) for spiral inductor on GaAs substrate or silicon substrate. Fig. 2.7 illustrates our modified circuit models for spiral inductors.

2.4 Experimental Results and Discussions

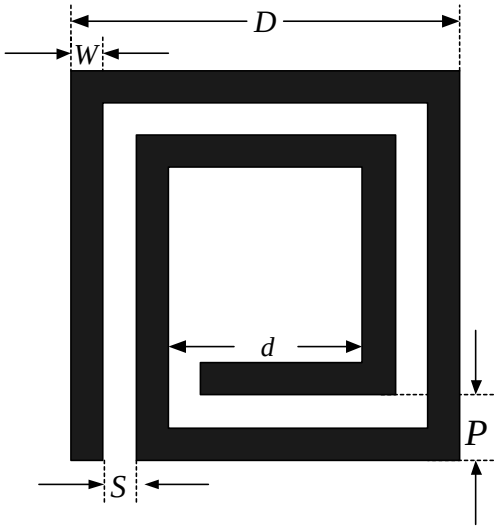

Fig. 2.8: Geometry of spiral inductor.

To confirm that our improved models and resistance expressions can indeed predict the overall inductor's behavior, the two-port *S*-parameters for three sets of square spiral inductors (Inductors 1, 2, and 3) and one set of circular spiral inductor (Inductors 4) are measured. With reference to Fig. 2.8 and Table 2.1, the detailed geometric parameters of the sample inductors are listed. The two-port *S* parameters of the spiral inductors are measured by using the vector network analyzer and coplanar probes. The calibration is up to the probe tip with SLOT and the parasitics are taken out after de-embedding.

	Shape	N	W (μm)	P(μm)	D(μm)	Substrate	Metal/Thickness(μm)	
Inductor 1	square	1.75	10	15	100	GaAs	Gold	1.5
Inductor 2	square	1.5	26	30	105	GaAs	Gold	1.8
Inductor 3	square	3.5	10	11.5	152.5	silicon	Alumni	0.7
Inductor 4	circular	2	6	8	103	silicon	Copper	1.0

Table 2.1: Geometric parameters of spiral inductors.

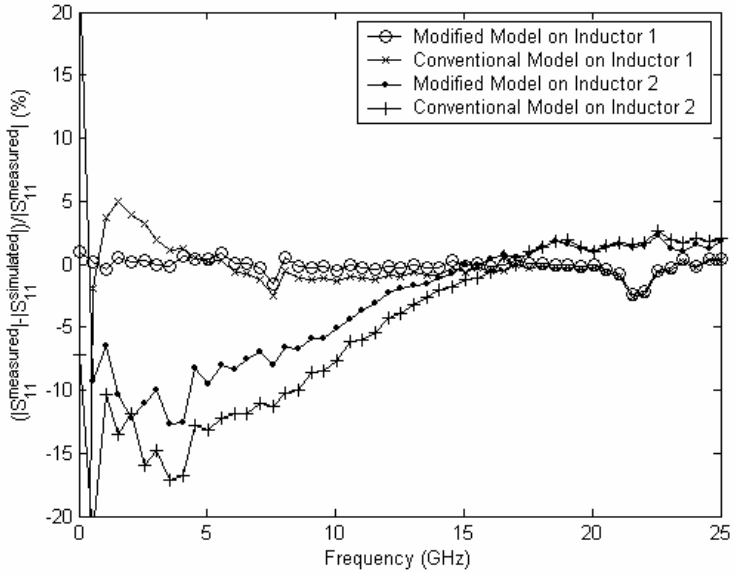

Fig. 2.9: Magnitude difference of *S*-parameter simulation results on the conventional model in Fig. 2.5 (*a*) and the modified model in Fig. 2.7 (*a*).

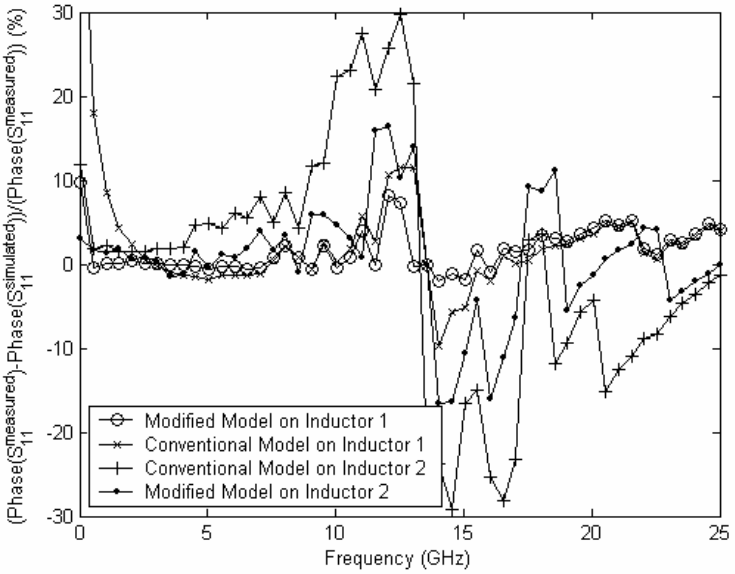

Fig. 2.10: Phase difference of *S*-parameter simulation results on the conventional model in Fig. 2.5 (*a*) and the modified model in Fig. 2.7 (*a*).

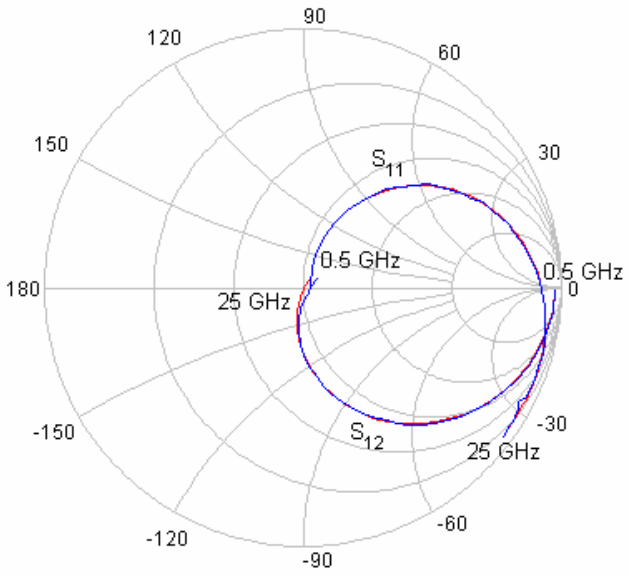

Fig. 2.11: *S*-parameter simulation results on modified circuit model in Fig. 2.7 (*a*) of Inductor 1 (blue line: measured data; red line: simulated data).

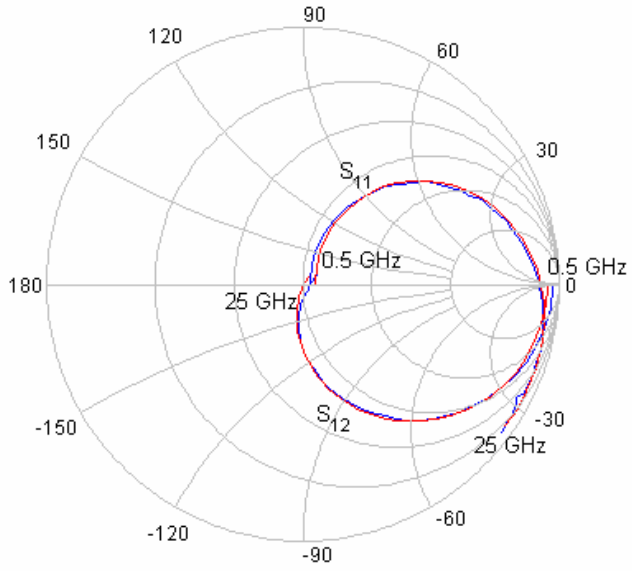

Fig. 2.12: *S*-parameter simulation results on conventional circuit model in Fig. 2.5 (*a*) of Inductor 1 (blue line: measured data; red line: simulated data).

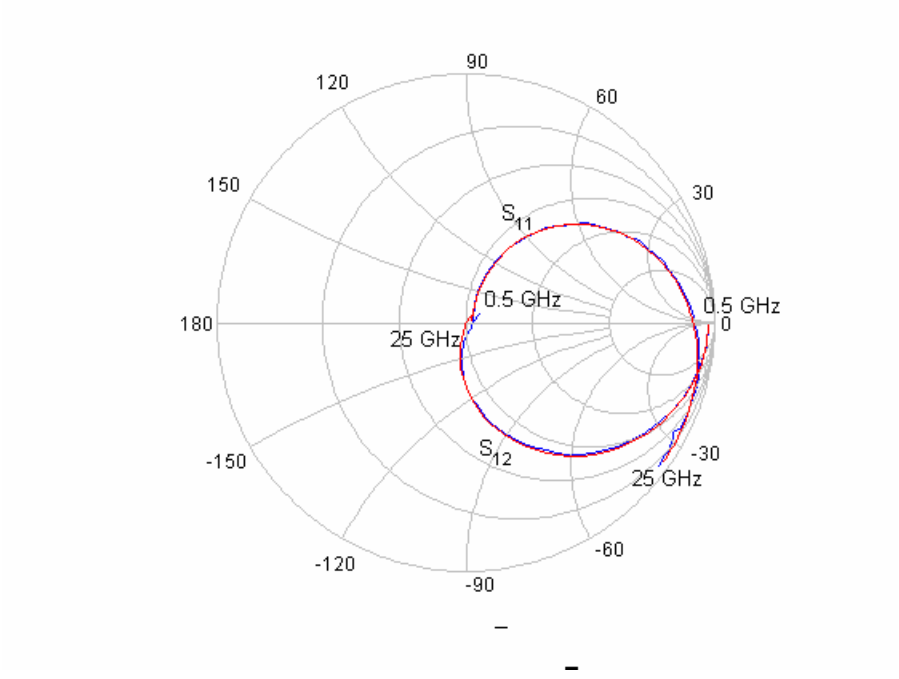

Fig. 2.13: *S*-parameter simulation results on modified circuit model in Fig. 2.7 (*b*) of Inductor 1 (blue line: measured data; red line: simulated data).

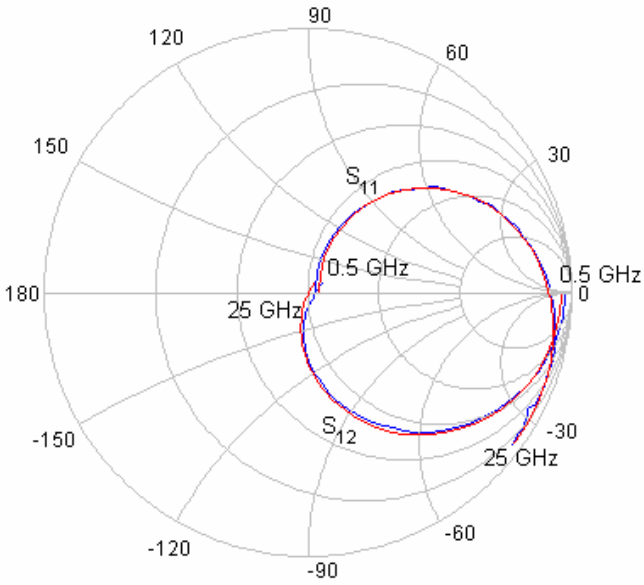

Fig. 2.14: *S*-parameter simulation results on conventional circuit model in Fig. 2.5 (*b*) of Inductor 1 (blue line: measured data; red line: simulated data).

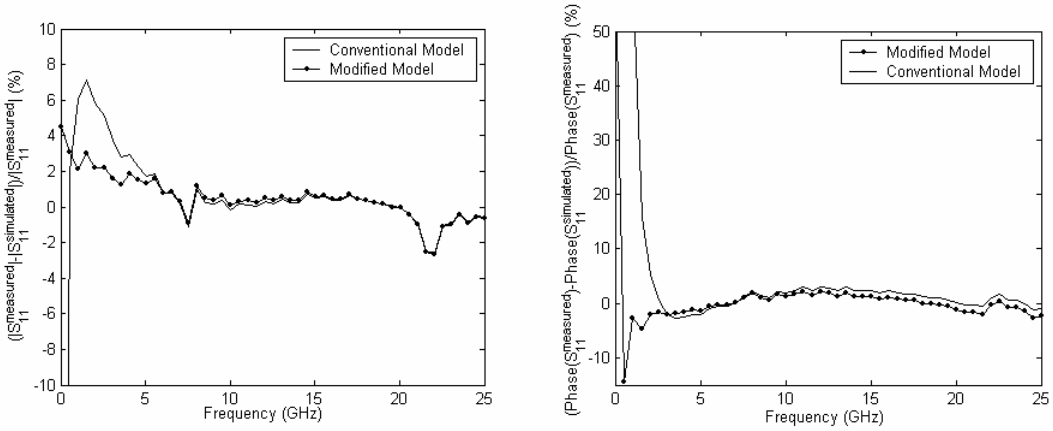

Fig. 2.15: Difference of *S*-parameter simulation results on the conventional model in Fig. 2.5 (*b*) and the modified model in Fig. 2.7 (*b*) for Inductor 1.

Figs. 2.9 and 2.10 provide the circuit simulation results of Inductors 1 and 2 with different circuit models. In these figures, the relative errors of magnitude between the simulated S_{11} with respect to the measured S_{11}, calculated from $\frac{\left|S_{11}^{measured}\right| - \left|S_{11}^{simulated}\right|}{\left|S_{11}^{measured}\right|} \times 100\%$, for both inductors are plotted; and the relative errors of phase are calculated from $\frac{Phase(S_{11}^{measured}) - Phase(S_{11}^{simulated})}{Phase(S_{11}^{measured})} \times 100\%$. As the relative errors of the magnitude from the modified model in Fig. 2.7 (*a*) are always smaller than those from the conventional model in Fig. 2.5 (*a*), the new model provides more accurate fitting with the measured results. For example for Inductor 1, the worst case fitting error of the magnitude of *S*-parameters with modified model is about 2.8% from 0.5GHz to 25GHz, and the worst case fitting error with conventional model is about 5.2%. The worst case fitting error of the phase of *S*-parameters with modified model is about 8.0%, and the worst case fitting error with conventional model is about 12.1%. The improvement of our modified model can also be observed from the Smith-Charts in Figs.

2.11 and 2.12. By comparing Fig. 2.13 with Fig. 2.14, we find that the model in Fig. 2.7 (*b*) is also more satisfactory for the *S*-parameter simulation than the conventional model in Fig. 2.5 (*b*), especially from 0.5GHz to 5GHz. Then, Fig. 2.15 confirms this result. Similar advantages of the new models can also be achieved with other inductors with different *N*, *S*, and *W*, which are fabricated using several external foundries.

Circuit Components	Conventional Model (*a*)	Conventional Model (*b*)	Modified Model (*a*)	Modified Model (*b*)
$R_s(\Omega)$	4.7	4.3	6.6	5.8
$R_s'(\Omega)$			4.6	4.2
$L_s(nH)$	2.4	2.4	2.4	2.4
$L_s'(nH)$			0.6	0.6
$C_s(fF)$	19.7	20.1	20.1	21.0
$R_{sub1}(\Omega)$	11.6	51.7	11.6	52.3
$R_{sub2}(\Omega)$	15.9	54.2	15.9	55.5
$C_{ox1}(fF)$		43.8		42.6
$C_{ox2}(fF)$		31.7		30.5
$C_{sub1}(fF)$	37.8	277.3	37.7	277.1
$C_{sub2}(fF)$	28.1	250.8	28.1	267.6

Table 2.2: Extracted values of circuit components from circuit optimization for Inductor 1.

Table 2.2 tabulates the circuit components' values in Figs. 2.5 and 2.7 for Inductor 1 after circuit optimization with IC-CAP. The objective error function is given as

$$\varepsilon_k = \sum_{f=1}^{F}\sum_{m=1}^{2}\sum_{n=1}^{2}\left|\frac{Mag(S_{mn}^{measured}(f))}{Mag(S_{mn}^{simulated}(f))}-1\right| + \sum_{f=1}^{F}\sum_{m=1}^{2}\sum_{n=1}^{2}\left|\frac{Phase(S_{mn}^{measured}(f))}{Phase(S_{mn}^{simulated}(f))}-1\right|. \quad (2.21)$$

Here, *F* refers to the total number of frequency points.

As noted from Table 2.2, the values of R_s and R_s' change significantly from the conventional models to the modified models. However, the changes of the respective

extracted inductances L_s and L_s', capacitance C_s, and other circuit components which contribute to the substrate effects, are relatively much smaller. Furthermore, the aim of our circuit optimization is usually to achieve the best fitting results for the whole measured frequency range, and in our measurement, the starting frequency is 0.5GHz, at which the eddy current will begin to affect the series resistance significantly. Thus, the circuit-extracted values of R_s will be a bit larger than the theoretical values of *dc* resistance R_0.

Figs. 2.16 and 2.17 give a general review of Y_2 and Y_3 parts in the π-mode circuit model of Inductor 1 as shown in Fig. 2.18, which can generally indicate the characters of the inductor substrate. From Figs. 2.16 and 2.17, it is noted that the resistance losses of the substrate are decreasing functions of frequencies. The series capacitances also change greatly in low frequency range (below 5GHz) and tend to be constant in higher frequency range. As the aim of circuit optimization is usually to achieve the best fitting results for the whole measured frequency range, the values of R_{sub1}, C_{sub1}, R_{sub2}, and C_{sub2} in Fig. 2.7 (*a*) are thus extracted from high frequencies automatically. However, using the circuit model in Fig. 2.7 (*b*), the resistances R_{sub1} and R_{sub2}, and the series capacitances C_{ox1} and C_{ox2}, can be extracted from relatively lower frequencies. Thus, from Figs. 2.16 and 2.17, if the simulation results for the substrate are considered for individually, the substrate structure in the modified model in Fig. 2.7 (*b*) is better and more reasonable than that in Fig. 2.7 (*a*).

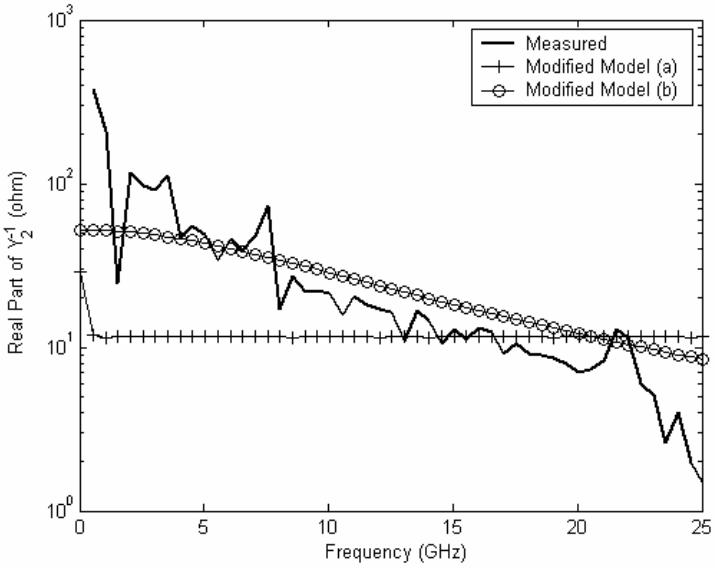

(*a*)

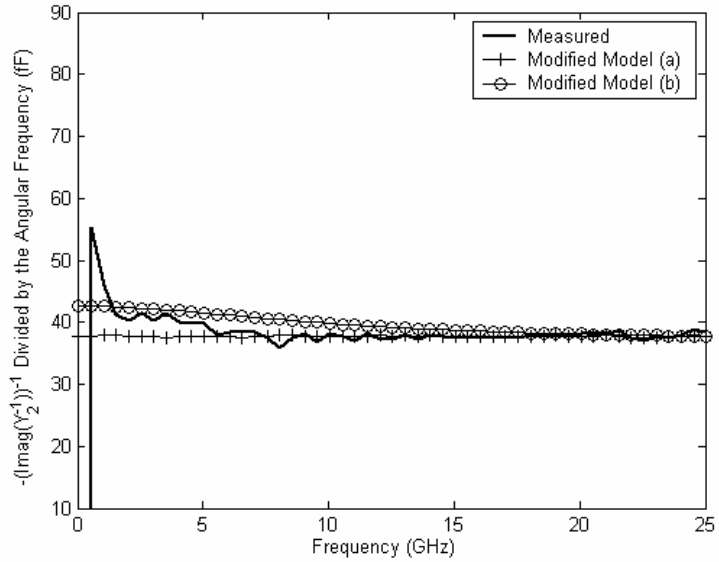

(*b*)

Fig. 2.16: Measured and simulated results of the real part of Y_2^{-1} (*a*) and $-\frac{1}{imag(Y_2^{-1})\omega}$ (*b*) on Inductor 1 with improved models.

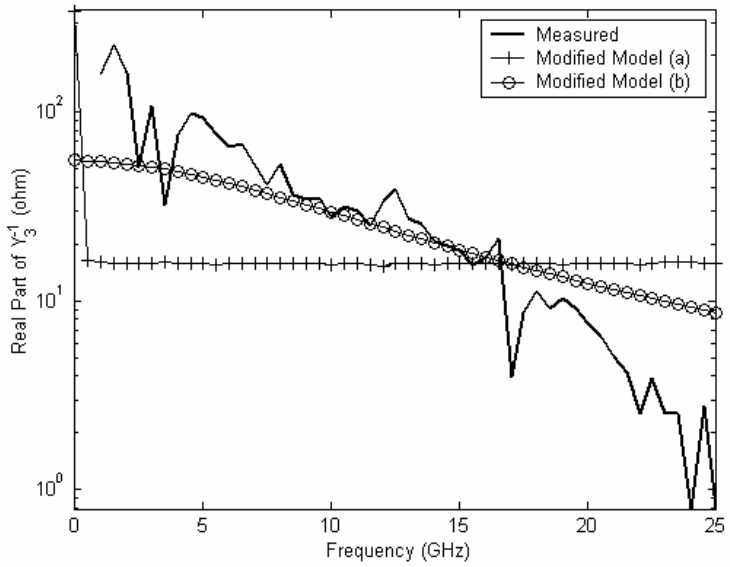

(*a*)

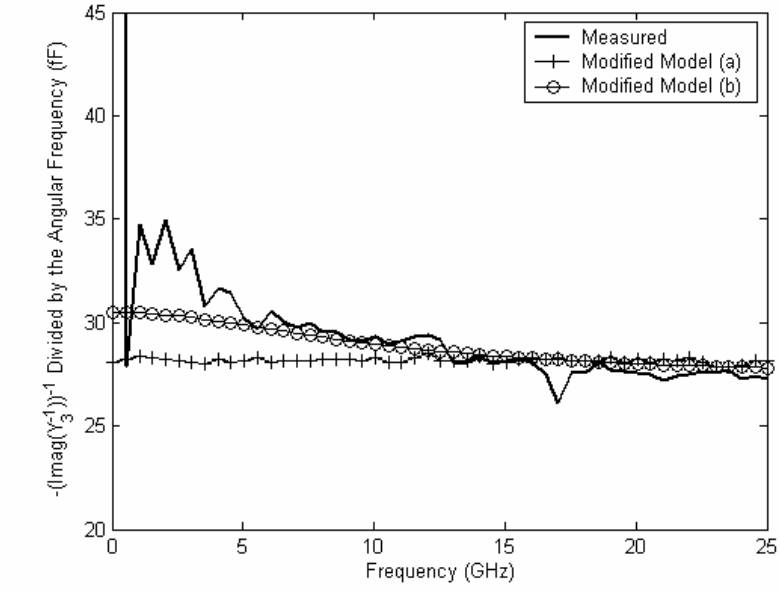

(*b*)

Fig. 2.17: Measured and simulated results of the real part of Y_3^{-1} (*a*) and $-\frac{1}{imag(Y_3^{-1})\omega}$ (*b*) on Inductor 1 with improved models.

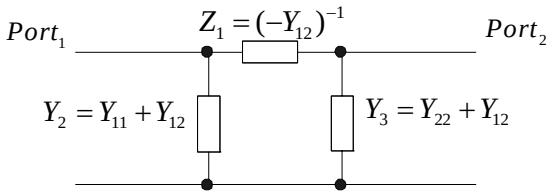

Fig. 2.18: General π -mode reciprocal network form of inductor.

Fig. 2.18 shows a general π-model of the equivalent circuit for the spiral inductor. IC-CAP is used for components extraction and optimization. With Fig. 2.7 (*a*), the de-embedded *Y*-parameters in terms of the measured *Y*-parameters data are expressed as

$$Y'_{11} = Y_{11} - j\omega C_s - (R_{sub1} + (j\omega C_{sub1})^{-1})^{-1}, \tag{2.22}$$

$$Y'_{12} = Y_{12} + j\omega C_s, \tag{2.23}$$

$$Y'_{21} = Y_{21} + j\omega C_s, \tag{2.24}$$

$$Y'_{22} = Y_{22} - j\omega C_s - (R_{sub2} + (j\omega C_{sub2})^{-1})^{-1}, \tag{2.25}$$

where Y'_{mn}s denote the modified *Y*-parameters after de-embedding. If the model in Fig. 2.7 (*b*) is utilized, equations (2.23) and (2.24) remain the same, and equations (2.22) and (2.25) are modified as

$$Y'_{11} = Y_{11} - j\omega C_s - ((j\omega C_{ox1})^{-1} + (1/R_{sub1} + j\omega C_{sub1})^{-1})^{-1}, \tag{2.26}$$

$$Y'_{22} = Y_{22} - j\omega C_s - ((j\omega C_{ox2})^{-1} + (1/R_{sub2} + j\omega C_{sub2})^{-1})^{-1}, \tag{2.27}$$

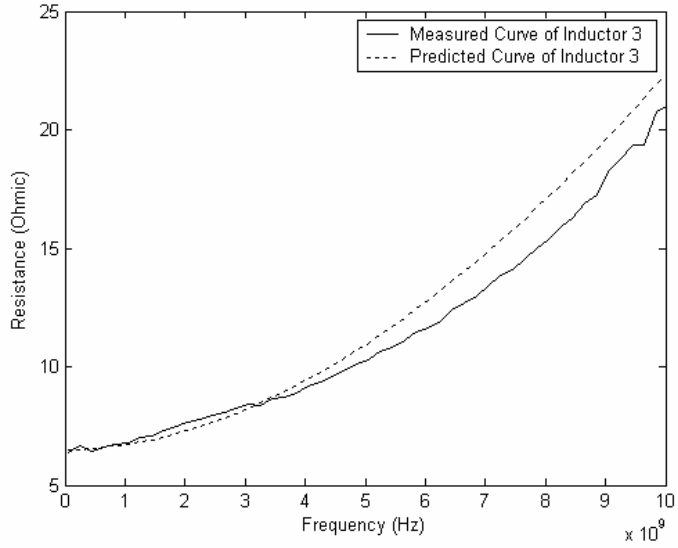

(*a*)

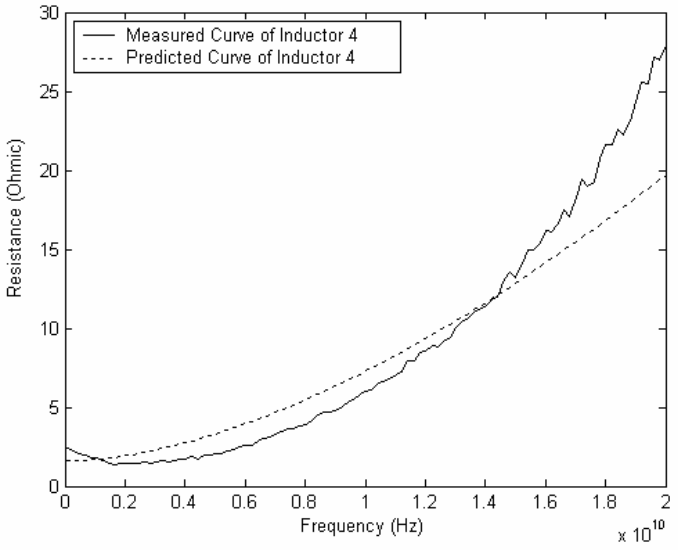

(*b*)

Fig. 2.19: Real part of input impedance of Inductor 3 and Inductor 4 after de-embedding.

By plotting the real and imaginary parts of $-(Y'_{12})^{-1}$, we can observe the characteristics of the input impedance of the physical spiral inductor respectively. As shown in Fig. 2.19, the measured resistances with increasing frequencies agree with our predictions in Section 2.2. In Fig. 2.19, the predicted curve refers to the equation (2.13). The deviations between the simulated and measured curves are mainly due to the

neglected substrate effects as their magnetic field induces an opposing current which will affect the existing current on the strips and the total resistance loss as well. In equation (2.13), the theoretically calculated values of the *dc* resistance R_0 of the whole spiral metallic trace are 6.5Ω and 1.6Ω for Inductor 3 and Inductor 4, respectively. The values of N_0 in equation (2.13) are both equivalent to 1 for Inductors 3 and 4.

In our further investigation, we also found that equation (2.13) is more accurate for the resistance simulation in the whole frequency range than equations (2.14) and (2.16). Equations (2.14) and (2.16) are valid when the frequency *f* is very low and the skin depth δ is much larger than the metal thickness *T*, respectively. By comparing the prediction of equation (2.14) of Inductor 4 with that of Inductor 3, we can also conclude that equations (2.14) are valid only when *f* is high enough so that δ is much smaller than *T*.

	Shape	*N*	$W(\mu m)$	$P(\mu m)$	$D(\mu m)$	Substrate
Inductor 5	symmetrical, octagon	3	8	12	187	silicon
Inductor 6	symmetrical, octagon	5	8	12	142	silicon
Inductor 7	symmetrical, octagon	3	8	12	280	silicon
Inductor 8	non-symmetrical, square	4.25	16	20	235	GaAs
Inductor 9	non-symmetrical, square	3.75	26	30	290	GaAs
Inductor 10	non-symmetrical, square	3.75	16	20	220	GaAs
Inductor 11	non-symmetrical, square	2.75	16	20	175	GaAs
Inductor 12	non-symmetrical, square	3	16	20	175	GaAs
Inductor 13	non-symmetrical, square	3.25	16	20	193	GaAs
Inductor 14	non-symmetrical, square	3.5	16	20	193	GaAs
Inductor 15	non-symmetrical, square	3.75	22	26	280	GaAs
Inductor 16	non-symmetrical, square	4	22	26	280	GaAs

Table 2.3: Detailed parameters of other sample inductors.

Table 2.3 lists the detailed parameters for more sample spiral inductors, Inductor 5 to Inductor 16. Figs. 2.20 to 2.22 show the simulation results with our modified circuit

model (as shown in Fig. 2.7 (*b*)) and the conventional model for Inductor 5 to Inductor 7. All the other results display the same trend as Figs. 2.20 to 2.22 and for brevity, Figs. 2.23 to 2.31 plot only the simulation results with the modified model in Fig. 2.7 (*a*) for Inductor 8 to Inductor 16. The fitting results are all quite satisfactory with minor fitting errors, which are mostly less than 10%.

The drawback of our circuit modification is that: due to skin effect, the increase of frequency will have other dramatic influences on a spiral inductor's resistance and inductance [98]-[99]. But these effects cannot simply be included in the circuit modeling by modifying circuit components or structure only. All our modifications with the circuit model mainly contribute to the existence of eddy current in the metallic trace of the inductor, but they do not contain much consideration of the skin effect.

2.5 Conclusion

The non-uniform *B*-field around a spiral inductor will cause eddy current in the metallic trace, resulting in the phenomenon of "current crowding". Appearance of current redistribution will dramatically increase the transmission loss at high frequencies, i.e., the series resistance of the metallic trace of the inductor, if we regard each spiral inductor as a two-port network. Expressions (2.4), (2.5), and (2.13) to (2.17), derived in this chapter, provide an approximate analysis model for the current crowding effects.

Here, an improved expression incorporating the skin effect for the prediction of series resistance in the spiral inductor model is also derived. Two novel modified equivalent circuit models for spiral inductors based on the analysis of eddy current are thus proposed. A good agreement between the simulated and the measured *S*-parameters is obtained.

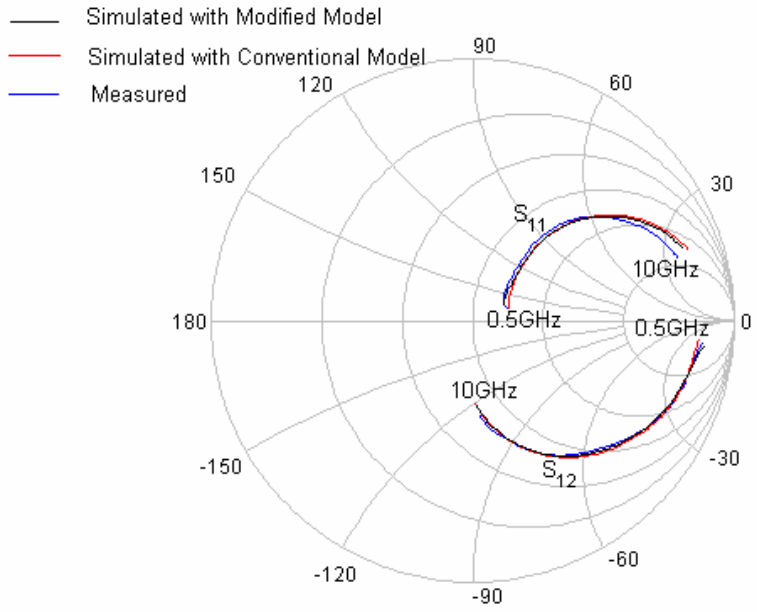

Fig. 2.20: *S*-parameter simulation results on modified (Fig. 2.7 (*b*)) and conventional (Fig. 2.5 (*b*)) circuit models of Inductor 5.

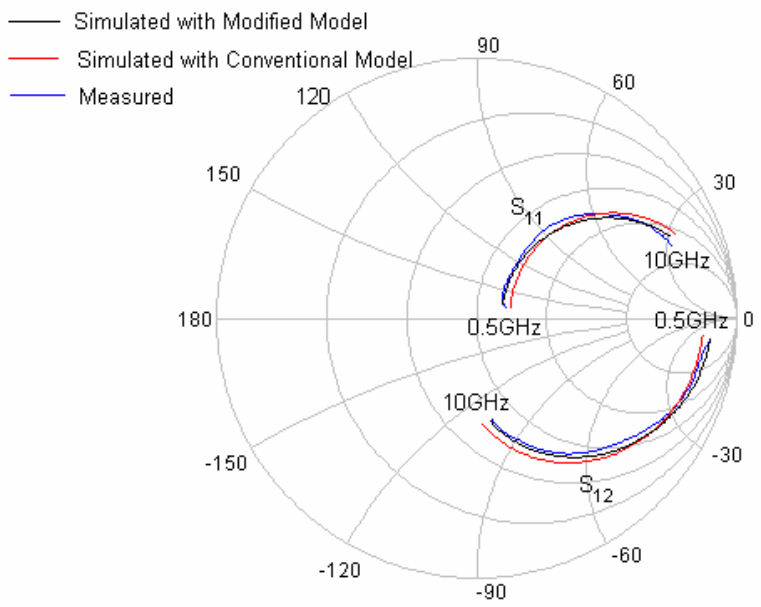

Fig. 2.21: *S*-parameter simulation results on modified (Fig. 2.7 (*b*)) and conventional (Fig. 2.5 (*b*)) circuit models of Inductor 6.

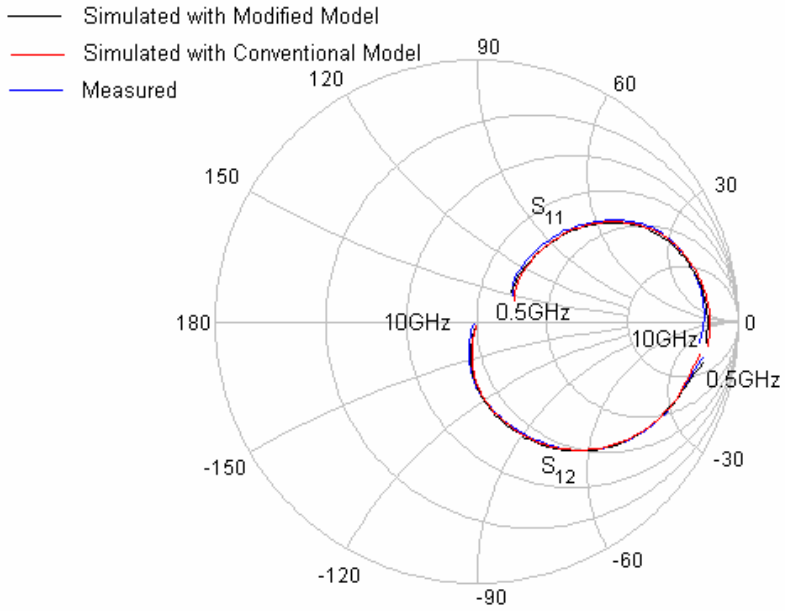

Fig. 2.22: *S*-parameter simulation results on modified (Fig. 2.7 (*b*)) and conventional (Fig. 2.5 (*b*)) circuit models of Inductor 7.

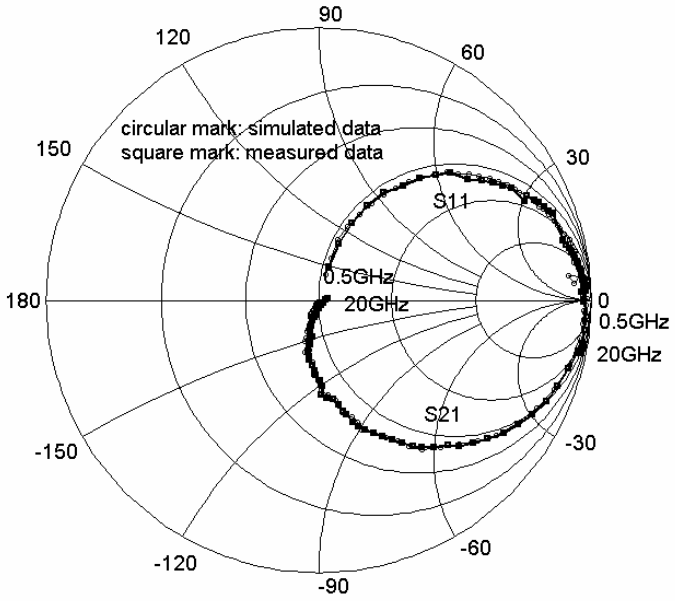

Fig. 2.23: *S*-parameter simulation results on modified circuit model (Fig. 2.7 (*a*)) of Inductor 8.

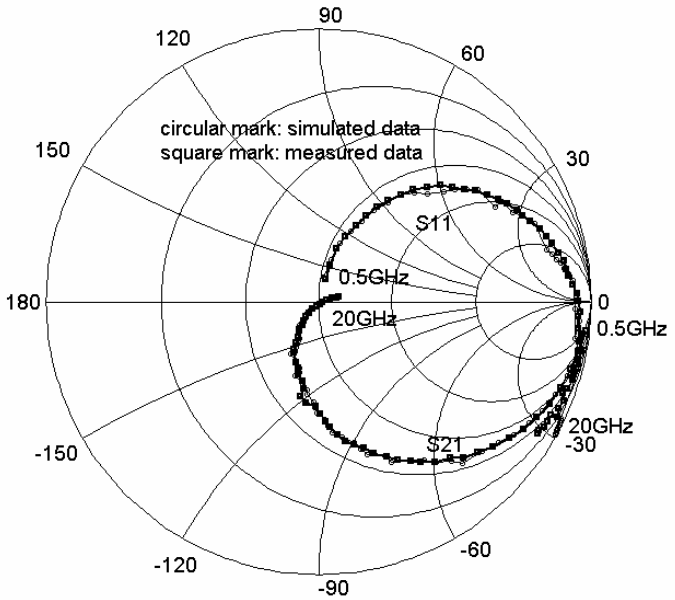

Fig. 2.24: *S*-parameter simulation results on modified circuit model (Fig. 2.7 (*a*)) of Inductor 9.

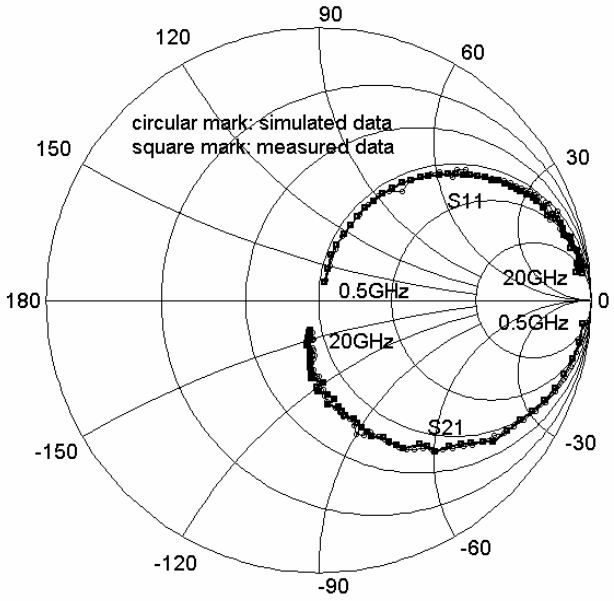

Fig. 2.25: *S*-parameter simulation results on modified circuit model (Fig. 2.7 (*a*)) of Inductor 10.

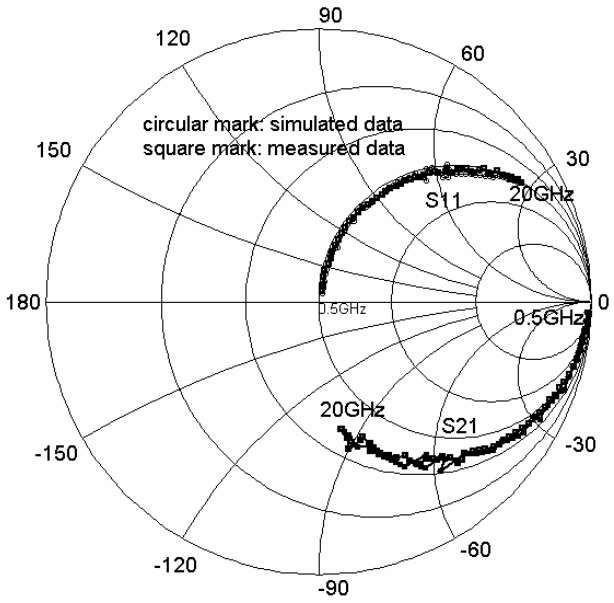

Fig. 2.26: *S*-parameter simulation results on modified circuit model (Fig. 2.7 (*a*)) of Inductor 11.

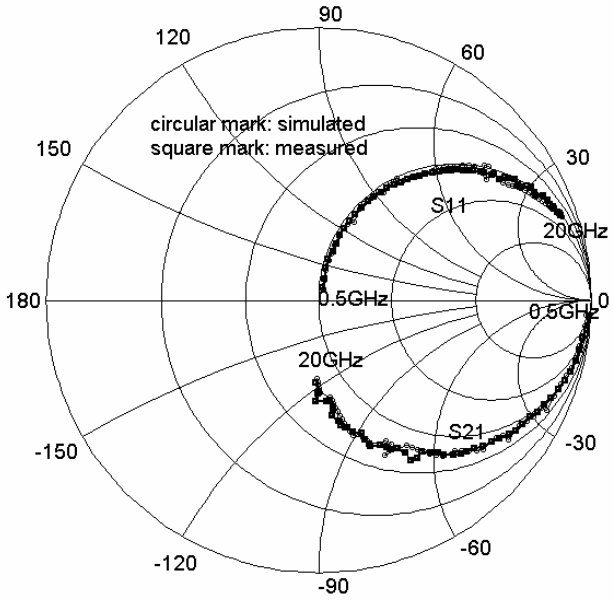

Fig. 2.27: *S*-parameter simulation results on modified circuit model (Fig. 2.7 (*a*)) of Inductor 12.

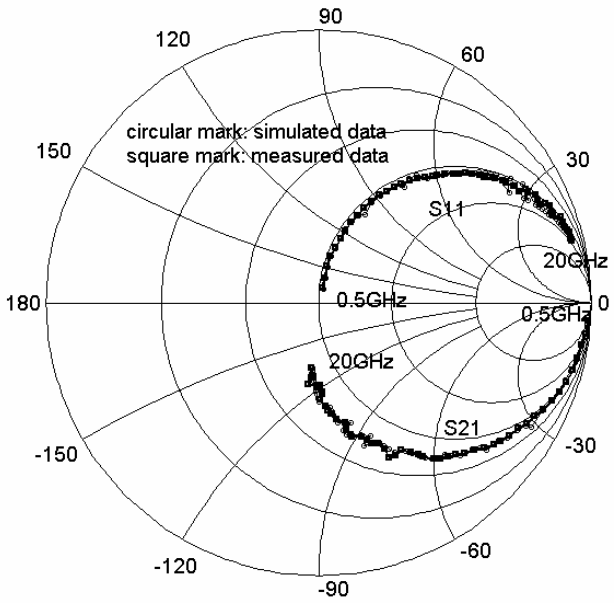

Fig. 2.28: *S*-parameter simulation results on modified circuit model (Fig. 2.7 (*a*)) of Inductor 13.

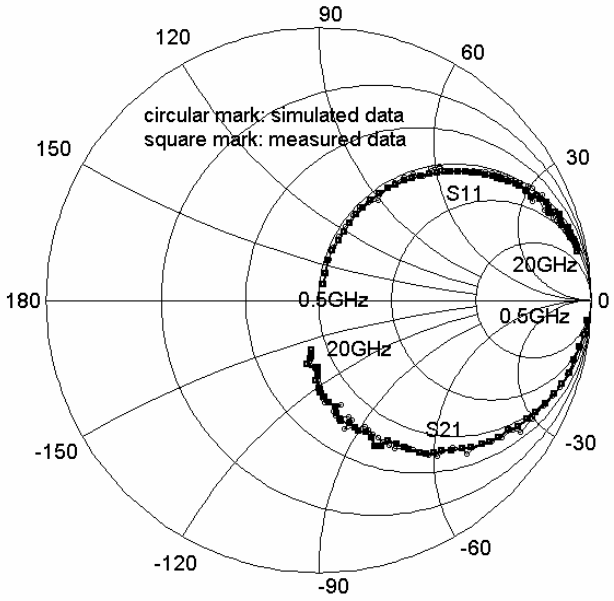

Fig. 2.29: *S*-parameter simulation results on modified circuit model (Fig. 2.7 (*a*)) of Inductor 14.

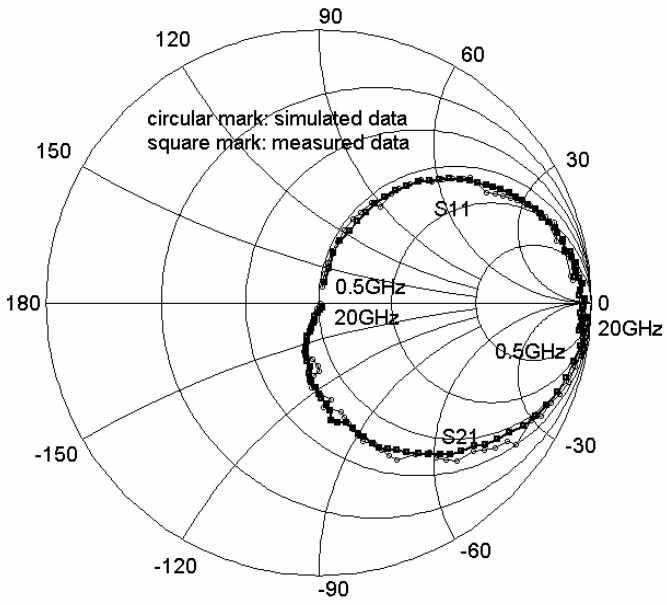

Fig. 2.30: *S*-parameter simulation results on modified circuit model (Fig. 2.7 (*a*)) of Inductor 15.

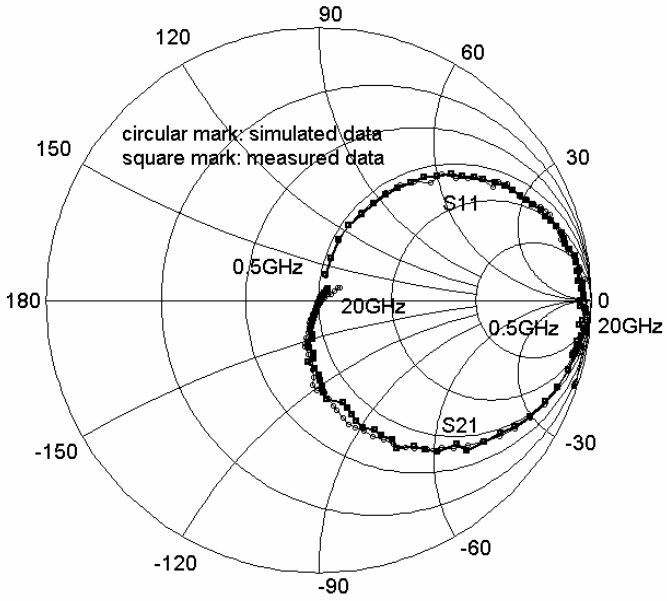

Fig. 2.31: *S*-parameter simulation results on modified circuit model (Fig. 2.7 (*a*)) of Inductor 16.

CHAPTER 3

INVESTIGATION OF INDUCTANCE OF SPIRAL INDUCTOR WITH NON-UNIFORM CURRENT DISTRIBUTION

3.1 Fundamental Concepts

Various approaches for modeling inductors on semiconductor have been reported in the past years [29]-[30], [32]-[33], and [41]. Since an inductor is intended for storing magnetic energy only, an ideal expression of its inductance in terms of metal width, gap spacing, and metal length is essential for the equivalent circuit modeling. An accurate numerical solution can be obtained by using a three-dimensional (3-D) finite-element simulator such as MagNet [54], but 3-D simulators are computationally intensive and time-consuming. Other techniques for analysis include the Greenhouse method [41] and [55], Wheeler formula [56], and "Data Fitted Monomial Expression" [57]. Data fitted expressions usually lack the precise theoretical interpretation, while the physical foundation for computing inductance is built on the concepts of the self-inductance of a wire and the mutual inductance between a pair of wires. A comprehensive collection of

formulae for inductance calculation was summarized by Grover in [58]. A commonly adopted assumption in the previously reported works on calculating inductance is that they usually neglected the frequency dependence of the spiral inductor's inductance.

The concept of inductance L can be interpreted as

$$L = -\frac{d\phi}{di} = -\frac{d(\oint B \cdot ds)}{di}, \tag{3.1}$$

where ϕ refers to the magnetic flux surrounded by one closed loop and i refers to the current. When the current in the materials is uniform, as the change of magnetic flux $d\phi$ is usually proportional to the change of the current di, the inductance depends only on the geometry of the system. But when the current distribution is non-uniform, things are no longer the same. Both the self- and the mutual inductance should be derived from more fundamental electromotive definition, i.e.,

$$e = -\frac{d\phi}{dt} = -L\frac{di}{dt}, \tag{3.2}$$

where e is the electromotive force induced by the change of magnetic flux $d\phi$ in one closed loop. This requires us to integrate each individual current element's contribution to the magnetic flux $d\phi$ together, due to the non-uniform current.

To state, both eddy current and skin effect will result in non-uniform current distribution in the metallic trace of a spiral inductor as discussed in the previous Chapter 2. Fortunately, we can approximate the relationship between the current redistribution and frequency by proper expressions such as in [2]. Then in this chapter, the development of inductance calculation will be improved further with the current redistribution.

3.2. Fundamental Analysis

3.2.1 Partial Inductance Calculations with Magnetic Flux Method

In this section, we use the concept of “partial inductance” [100]-[101] as the fundamental method to derive the inductance calculation. Partial inductances involve the magnetic flux between a conductor and infinity. To simplify the electromagnetic mechanism in a spiral inductor, we consider firstly two conductors with rectangular cross sections as in Fig. 3.1. Both the width and the thickness of the two cross sections are divided into several infinitely thin segments, so that each current in one filament can now be assumed to be uniformly distributed.

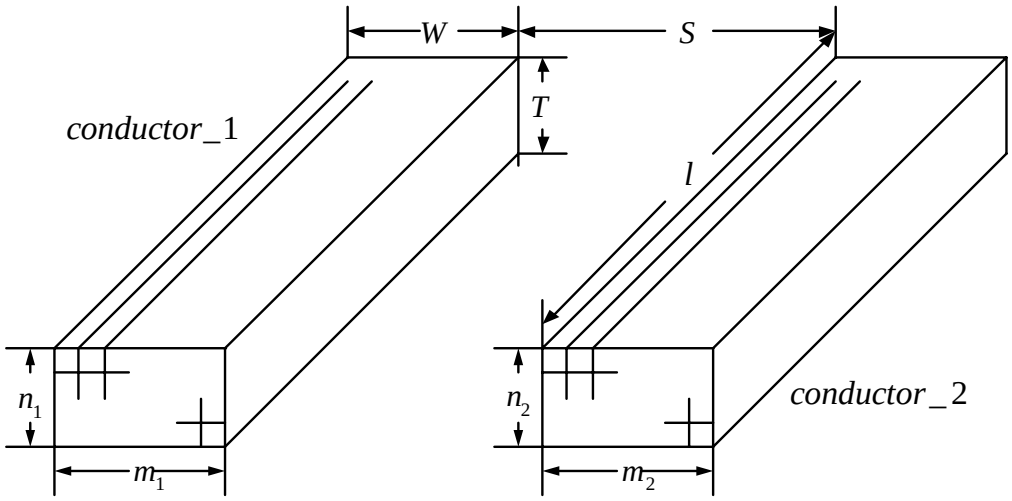

Fig. 3.1: Illustration of two straight conductors.

Conventionally, the mutual inductance between two parallel conductors is usually approximated by resolving the conductor cross sections into smaller filaments [102] and using the magnetic flux method. Then, the overall partial mutual inductance can be obtained through

$$M \approx \frac{1}{m_1 n_1} \frac{1}{m_2 n_2} \sum_{i=1}^{m_1 n_1} \sum_{j=1}^{m_2 n_2} M_{ij}, \tag{3.3}$$

where M_{ij} is the mutual partial inductance between two filaments in different conductors in Fig. 3.1. This expression is valid with uniform current distributions. The term $1/m_1 n_1$ represents the uniformly distributed current in each *source filament*, and the term $1/m_2 n_2$ describes the approximate uniformly distributed magnetic flux on each *field filament*.

For the case of non-uniformly current distribution, the usage of equation (3.3) is generally limited. By extending the magnetic flux method to include the non-uniform current distribution, equation (3.3) should be modified to

$$M \approx \begin{cases} \dfrac{1}{m_2 n_2} \displaystyle\sum_{i=1}^{m_1 n_1} \left(k_i' \sum_{j=1}^{m_2 n_2} M_{ij} \right) \Big/ \sum_{i=1}^{m_1 n_1} k_i' \\ or \\ \dfrac{1}{m_1 n_1} \displaystyle\sum_{j=1}^{m_2 n_2} \left(k_j'' \sum_{i=1}^{m_1 n_1} M_{ij} \right) \Big/ \sum_{j=1}^{m_2 n_2} k_j'' \end{cases}, \tag{3.4}$$

where k_i' represents the current weighting function in each filament I_i' in conductor_1 as

$$I_i' = k_i' I_{total}' \Big/ \sum_{i=1}^{m_1 n_1} k_i', \tag{3.5}$$

and k_j'' represents the current weighting function in each filament I_j'' in conductor_2 as

$$I_j'' = k_j'' I_{total}'' \Big/ \sum_{j=1}^{m_2 n_2} k_j''. \tag{3.6}$$

Here, the current in each filament is approximated to be constant because the dimension of the filament is small enough compared with the interested wavelength. Both

I'_{total} and I''_{total} are respectively the root mean squared (rms) total current in conductor_1 and conductor_2. From equation (3.4), it can be found that the use of magnetic flux method will give rise to some ambiguities in the value of mutual inductance. For example, when $I'_{total} \neq I''_{total}$, the formula (3.4) will usually yield two different values of mutual inductance. In addition, two different values of mutual inductance may also be obtained, even if $I'_{total} = I''_{total}$. That is because the current density in some filament in one of those two conductors can still be different from that of the corresponding filament in the other conductor, or the two conductors are with different numbers of filaments. However, for the latter case, if the numbers of filaments are sufficiently large, the two different values of mutual inductance will in the limit be the same.

3.2.2 Energy Method in Calculating the Effective Inductance

In [58], Grover proposed the general and fundamental principles for the inductance calculations with the magnetic energy method.

When a current I' is established in a circuit or element of a circuit, the rise of current induces an electromotive force that will oppose the rise of current. Thus, energy has to be expended by the source, in order to keep the current flowing against the induced electromotive force *e*. If we denote by *I* the current at any moment, the power expended in forcing the current against the induced electromotive force in equation (3.2) can be expressed as

$$p = LI\frac{dI}{dt}. \tag{3.7}$$

Here, L is the total inductance of the circuit.

Thus, the total energy supplied in raising the current to the final value I' is

$$W_1 = \int_0^{T_0} LI\frac{dI}{dt}dt = \int_0^{I'} LIdI = \frac{1}{2}LI'^2, \tag{3.8}$$

in which T_0 is the time interval for the establishment of the current. This energy is stored in the magnetic field and becomes available in the circuit when the current is broken [58]. It may also be shown that energy is stored in each volume element dV of the field to the amount of $\frac{H^2}{8\pi}dV$, where H is the magnetic field intensity at the point in question.

If the current I' is being established in circuit 1, a current I'' is maintained in circuit 2 that has a mutual inductance M with circuit 1, then during the rise of I, an electromotive force $-M\frac{dI}{dt}$ is induced in circuit 2. To force the current I'' against this force, some extra energy is required. This energy can be expressed as

$$W_2 = \int_0^{T_0} M\frac{dI}{dt}I''dt = MI'I''. \tag{3.9}$$

If the induced electromotive force is in such a direction that it aids the flow of the current I'', then the energy is returned to the source of I'' and M is to be considered as negative; otherwise, M is to be considered as positive.

The energy of a system consisting of two circuits 1 and 2, in which currents I' and I'' respectively are established, can be calculated by supposing that the current I' in one circuit to be made first. Then the other current is supposed to rise from zero to I'', while I' is held constant. First, with circuit 2 open, the rise of the current in circuit 1 from zero to I' involves the storing of energy $\frac{1}{2}L_1 I'^2$ in the magnetic field as calculated in equation (3.8). As the current in circuit 2 then rises from zero to I'', energy $\frac{1}{2}L_2 I''^2$ is supplied by the source 2 and, at the same time, source 1 has to supply $MI'I''$ to maintain current I' unchanged. The total magnetic energy stored in the system of two circuits is, therefore,

$$W = \frac{1}{2}L_1 I'^2 + \frac{1}{2}L_2 I''^2 + \frac{1}{2}MI'I'' + \frac{1}{2}MI''I', \tag{3.10}$$

where L_1 and L_2 represent the total inductance of the two circuits respectively, and the last two terms in this equation describe the stored magnetic energy due to the mutual inductance *M* between these two circuits.

If there are *n* circuits carrying currents $I_1, I_2, \cdots I_n$, having mutual inductances M_{12}, M_{13}, etc., the energy of the whole system is the sum of terms of the form $\frac{1}{2}L_i I_i^2$ for each circuit, and a term $M_{ij}I_i I_j$ for each pair of coupled circuits. The magnetic field intensity at each point is, of course, the resultant of the components due to the individual circuits.

When the current is non-uniformly distributed in the conductors in Fig. 3.1, we can express the overall mutual inductance between them as

$$M = \frac{W_{total}}{I'_{total} I''_{total}}. \tag{3.11}$$

By defining the concept of *effective mutual inductance* M_{eff}, we achieve

$$M_{eff} = \sum_{i=1}^{m_1 n_1} \left(k'_i \sum_{j=1}^{m_2 n_2} \left(k''_j M_{ij} \right) \right) \Bigg/ \left(\sum_{i=1}^{m_1 n_1} k'_i \sum_{j=1}^{m_2 n_2} k''_j \right). \tag{3.12}$$

Equation (3.12) is more convenient to be used than equation (3.4) especially for the different current distribution cases of the two conductors, as the above-stated ambiguity is thus resolved. When the currents are uniform and their distributions are the same over the cross sections of the two parallel conductors, these two methods, namely through equation (3.4) and through equation (3.12), are identical.

3.3 Derived Inductance Formulae for Spiral Inductor with Non-uniform Current Distribution

3.3.1 Self- and Mutual Inductances with Magnetic Flux Method

When the current in a wire is uniform, the self-inductance is primarily determined by the magnetic flux external to the wire, while the mutual inductance is determined by the mutual effects between two wires. In our case, the current in each filament in Fig. 3.1 can be assumed to be uniform. Thus, the overall self-inductance of the metallic trace of an

inductor can be considered to be the total effect of the self- and mutual inductances of all the filaments in its cross section. The overall mutual inductance between two metallic traces should be recalculated due to the non-uniform current distribution.

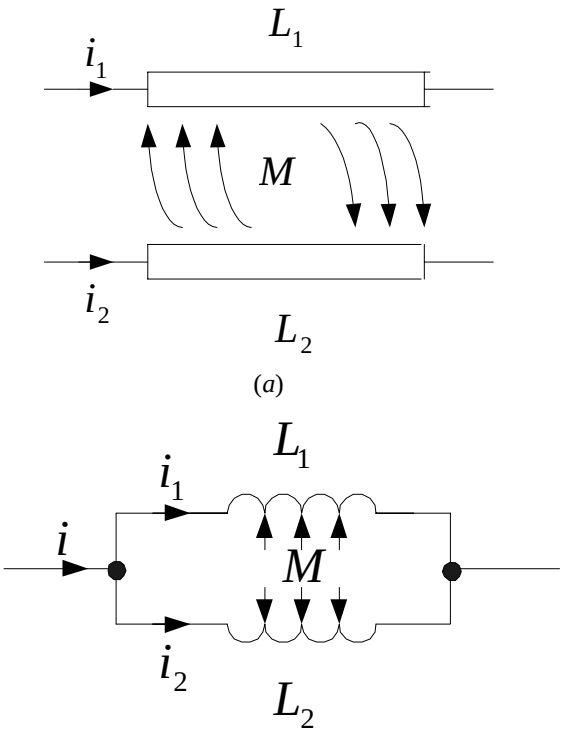

Fig. 3.2: Mutual inductance *M* in relation to the self-inductance L_1 and L_2.

Fig. 3.2 (*a*) shows how the overall inductance with two parallel filaments is computed. In each equipotential metallic body of the structure, both filaments are excited approximately by the same voltage as shown in Fig. 3.2 (*b*). The overall inductance of two-filament system can thus be approximated by

$$L = \frac{d\phi}{di_{total}} \approx \frac{d(\phi_1 + \phi_2)}{di_{total}} = \frac{d[(\phi_{11} + \phi_{12}) + (\phi_{21} + \phi_{22})]}{di_{total}}, \tag{3.13}$$

where ϕ_{ij} refers to the magnetic flux effect in the j^{th} filament induced by the i^{th} current filament. By assuming $i_1/i_2 = k_1/k_2$, $\left(\frac{k_1+k_2}{k_1}\right)\frac{2d\phi_{11}}{di_{total}} = L_1 = L_2 = \left(\frac{k_1+k_2}{k_2}\right)\frac{2d\phi_{22}}{di_{total}}$, and the magnetic flux is uniformly distributed within the filament, the overall inductance of Fig. 3.2 (*b*) is given by

$$\begin{aligned} L &\approx \frac{\left(\frac{k_1 di_{total}}{k_1+k_2}\right)\frac{1}{2}\left(L_1 \pm M\right)+\left(\frac{k_2 di_{total}}{k_1+k_2}\right)\frac{1}{2}\left(L_2 \pm M\right)}{di_{total}} \\ &= \frac{1}{2}\left(\left(\frac{k_1}{k_1+k_2}\right)L_1 + \left(\frac{k_2}{k_1+k_2}\right)L_2 \pm M\right) = \frac{L_1 \pm M}{2}, \end{aligned} \tag{3.14}$$

where L_j (j=1 or 2), and M are the frequency-independent self-inductance of filament and mutual inductance between filaments respectively, and k_j (j=1 or2), is the current weighting function. Using the same analogy as the two-filament case above, the overall inductance for the N-filament system can be computed by

$$L_{self} \approx \frac{1}{N}\left[L_1 + \sum_{n=1}^{N}\left(\left[\frac{k_n}{\sum_{j=1}^{N} k_j}\right]\sum_{\substack{m=1 \\ m\neq n}}^{N} M_{mn}\right)\right] \approx \frac{\sum_{n=1}^{N}\left(k_n \sum_{m=1}^{N} M_{mn}\right)}{N\sum_{j=1}^{N} k_j}, \tag{3.15}$$

where $N = m_1 n_1 = m_2 n_2 = \cdots$ is the total number of filaments in each metallic trace, and M_{mn} is the mutual inductance value between the m^{th} and the n^{th} current filaments, and

$$i_n = \left(\frac{k_n}{\sum_{j=1}^{N} k_j}\right) i_{total}. \tag{3.16}$$

Here, we assume $L_1 = L_2 = \cdots = L_N$ in equation (3.15). Thus, quite similar to equation (3.15), the mutual inductance between any pair of traces with *N* filaments each (as shown in Fig. 3.1) is expressed as

$$L_{mutual} = \frac{1}{m_1 n_1} \sum_{n=1}^{m_2 n_2} \sum_{m=1}^{m_1 n_1} \left(\frac{k_n}{\sum_{j=1}^{N} k_j} M'_{mn} \right), \tag{3.17}$$

where M'_{mn} refers to the mutual inductance between the m^{th} and the n^{th} current filaments in different metallic traces (as shown in Fig. 3.1). The sum of each M' due to all of the other metallic traces will provide an overall inter-trace mutual inductance of a spiral inductor.

3.3.2 Geometric Mean Distance

The simplified formula for the mutual inductance (expressed in μH) between two parallel filaments with length *l* and distance *g* (both expressed in centimeters) is

$$M = 0.002l[\ln(\frac{l}{g} + \sqrt{1 + \frac{l^2}{g^2}}) - \sqrt{1 + \frac{g^2}{l^2}} + \frac{g}{l}] \approx 0.002l(\ln\frac{2l}{g} - 1 + \frac{g}{l} - \frac{g^2}{4l^2} + \cdots), \tag{3.18}$$

when $\frac{g}{l}$ is not very big [58].

In the case of two equal straight conductors of rectangular cross sections, we can use the *geometric mean distance R* to replace *g* in equation (3.18). Then, the conductor can be considered as infinitely thin filament on the cross section, and the geometric mean

distance represents the total effect of the distance between each pair of points R_{mn} (as shown in Fig. 3.3). Similar to [58], we have to find $\frac{1}{N}$ of the sum of the N values of the logarithm of the distance between the N pairs of points $(N \to \infty)$.

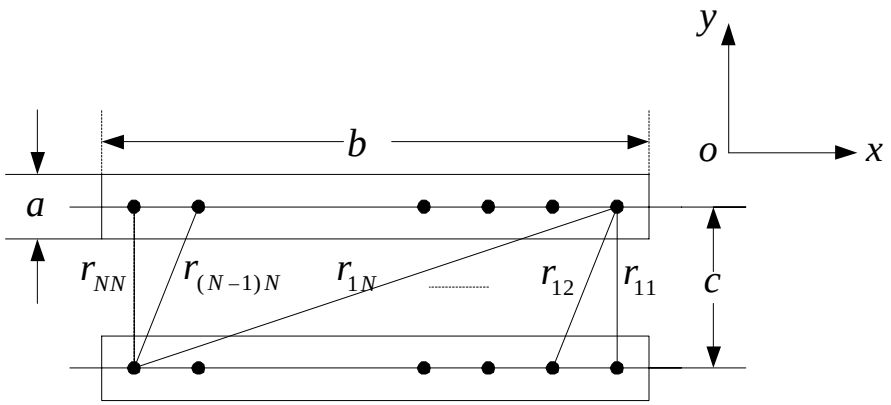

Fig. 3.3: Illustration of the rectangular cross section of two equal conductors.

If $a << b$, the difference between R and c is mainly caused by the geometric size of the conductor cross section on the x direction, and it is not on the y direction. Thus, we obtain

$$R' = \lim_{N\to\infty}(\prod_{m=1}^{N}(\prod_{n=1}^{N} r'_{mn})^{1/n})^{1/m}, \tag{3.19}$$

where $r'_{mn} = \sqrt{c^2 + [(m-n)\frac{b}{N}]^2}$.

In the same case, with the idea of *geometric mean distance of an area from itself* R' in [58], we can also introduce equation (3.18) to calculate the term L_1 in equation (3.15) with

$$R = \lim_{N\to\infty}(\prod_{m=1}^{N}(\prod_{\substack{n=1\\ n\neq m}}^{N} r_{mn})^{1/n})^{1/m}, \tag{3.20}$$

where $r_{mn} = |m-n|\frac{b}{N}$.

3.3.3 Modified Inductance Calculation under Skin Effect

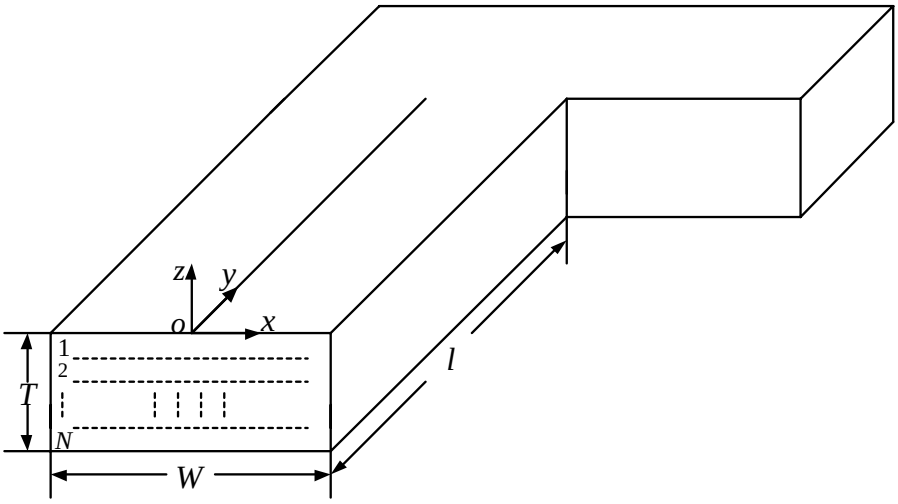

Fig. 3.4: Dividing method on the cross section of metallic trace under skin effect.

The current is uniformly distributed in the rectangular cross section of a spiral inductor at *dc*. As the frequency is increased, the current will crowd to the surface and is eventually concentrated in an annulus of thickness from the surface [41], and [103]-[105]. This phenomenon is called *skin effect*. The most critical parameter pertaining to skin effect is the *skin depth*, which is defined as

$$\delta = \sqrt{\frac{1}{\pi\sigma\mu f}}, \tag{3.21}$$

where σ, μ and f respectively represent the conductivity, the permeability, and frequency. The attenuation of the current density, J_s, as a function of distance z away from the surface can be represented by the function

$$J_s(z) = \begin{cases} J_0 e^{z/\delta}, & 0 \geq z \geq -T/2 \\ J_0 e^{-(z+T)/\delta}, & -t/2 \geq z \geq -T \end{cases}, \tag{3.22}$$

where J_0 and T refer to the current density at the surface ($z = 0$ and -T) and the thickness of the metallic trace respectively (see in Fig. 3.4). The current, I, can be obtained by integrating J_s over the whole cross-sectional area, yielding

$$I = W\left(\int_{-T/2}^{0} J_0 e^{z/\delta} dz + \int_{-T}^{-T/2} J_0 e^{-(z+T)/\delta} dz \right) = 2WJ_0\delta\left(1 - e^{-T/2\delta}\right), \tag{3.23}$$

where W is the width of the metallic trace. As the variations of the current density mainly occur along the z direction under skin effect, we can divide the cross section into infinitely thin filaments on the z direction. Such will also satisfy the conditions for equations (3.18) to (3.20). By combining equations (3.15) to (3.17), and setting the current weighting function as $k_n = J_s\left(z = -\frac{nT}{N} \right)\frac{TW}{N}$, the proposed inductance calculation due to the current redistribution under skin depth effect becomes

$$\frac{L_{self}^{\beta}}{L_{self}^{\alpha}} = K_1 = \lim_{N\to\infty} \frac{T\sum_{n=1}^{N/2} e^{-Tn/(N\delta)} \sum_{m=1}^{N} \overline{M_{mn}}}{\delta\left(1 - e^{-T/2\delta}\right)\sum_{n=1}^{N}\sum_{m=1}^{N} \overline{M_{mn}}}, \tag{3.24}$$

$$\frac{L_{self}^{\beta'}}{L_{self}^{\alpha}} = K_1' = \lim_{N\to\infty} \frac{T^2 \sum_{i=1}^{N/2} \left(e^{-iT/(N\delta)} \left(\sum_{j=1}^{N/2} \left(e^{-jT/(N\delta)} \overline{M_{ij}} \right) + \sum_{j=1+N/2}^{N} \left(e^{(jT-NT)/(N\delta)} \overline{M_{ij}} \right) \right) \right)}{2\delta^2 \left(1 - e^{-T/2\delta}\right)^2 \sum_{i=1}^{N}\sum_{j=1}^{N} \overline{M_{ij}}}, \tag{3.25}$$

$$\frac{L_{mutual}^{\beta}}{L_{mutual}^{\alpha}} = \lim_{N\to\infty} \frac{T\sum_{n=1}^{N/2} e^{-Tn/(N\delta)} \sum_{m=1}^{N} \overline{M'_{mn}}}{\delta\left(1 - e^{-T/2\delta}\right)\sum_{n=1}^{N}\sum_{m=1}^{N} \overline{M'_{mn}}}, \tag{3.26}$$

and

$$\frac{L_{mutual}^{\beta'}}{L_{mutual}^{\alpha}} = \lim_{N\to\infty} \frac{T^2 \sum_{i=1}^{N/2} \left(e^{-iT/(N\delta)} \left(\sum_{j=1}^{N/2} \left(e^{-jT/(N\delta)} \overline{M'_{ij}} \right) + \sum_{j=1+N/2}^{N} \left(e^{(jT-NT)/(N\delta)} \overline{M'_{ij}} \right) \right) \right)}{2\delta^2 \left(1 - e^{-T/2\delta}\right)^2 \sum_{i=1}^{N} \sum_{j=1}^{N} \overline{M'_{ij}}}, \quad (3.27)$$

where the superscripts α , β, and β' represent, respectively, the conditions when the current is uniformly distributed, when it is under skin depth effect with the magnetic flux method calculation, and when it is under skin depth effect with the energy method calculation. $\overline{M_{mn}}$ refers to the mutual inductance between the m^{th} and the n^{th} filaments in the same straight metallic trace and $\overline{M'_{mn}}$ refers to the mutual inductance between the m^{th} and the n^{th} filaments in different straight metallic traces. They can all be calculated from equations (3.18) to (3.20).

As the distance between two filaments in different straight metallic traces of the spiral inductor is much larger than the filaments' thickness, we can approximate that

$$\sum_m \overline{M'_{m1}} = \sum_m \overline{M'_{mn}} = \cdots \sum_m \overline{M'_{mn}}. \quad (3.28)$$

Therefore, when the skin effect is considered alone, we have

$$L_{mutual}^{\alpha} \approx L_{mutual}^{\beta} \approx L_{mutual}^{\beta'}. \quad (3.29)$$

3.3.4 Modified Inductance Calculation with Eddy Current

The phenomenon of *current crowding* due to the appearance of *eddy current* was studied in [2]. An approximate expression to describe the eddy current is given as

$$J_{eddy}(x) = 2\pi f I_0 \sigma B(\tau) x. \tag{3.30}$$

Here, τ is the number of turn of the spiral inductor, $B(\tau)$ is a function which changes with τ only for each fixed inductor, and I_0 is the excitation current (shown in Fig. 3.5). If we divide the cross section into infinitely thin filaments along the *x* direction, we can achieve

$$L_{self}^{\gamma} \propto \lim_{N,N'\to\infty} \sum_{n=1}^{N} \Big(\sum_{\substack{m=1 \\ m\neq n}}^{N} \overline{M_{mn}} + \sum_{m'=1}^{N'} \overline{M_{m'n}} \Big) - \lim_{N,N'\to\infty} \sum_{n'=1}^{N'} \Big(\sum_{m=1}^{N} \overline{M_{mn'}} + \sum_{\substack{m'=1 \\ m'\neq n}}^{N'} \overline{M_{m'n'}} \Big) = 0, \tag{3.31}$$

and quite similarly,

$$L_{self}^{\gamma'} \approx 0, \tag{3.32}$$

where the superscript γ and γ' represent the conditions with eddy current effect, for the magnetic flux method and for the energy method, respectively. The effect of eddy current on the overall self-inductance is neutralized as the eddy current on both sides of a metallic trace is in opposite direction. This phenomenon also exists under the presence of skin depth effect and thus equations (3.31) and (3.32) are still valid under the incorporation of skin depth and eddy current effects.

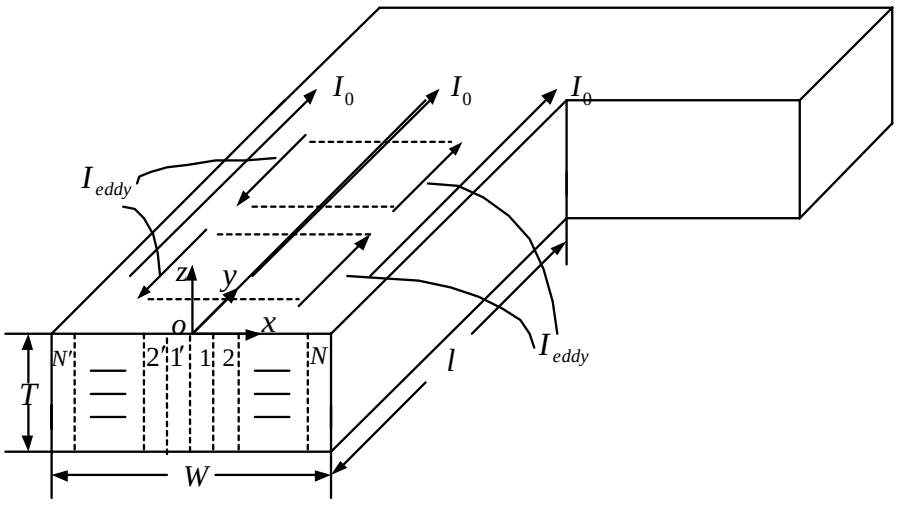

Fig. 3.5: Dividing method on the cross section of metallic trace with eddy current.

While considering for the mutual inductance between two different metallic traces, the total excitation current should also be assumed to be I_0 because the eddy current is inducted by it. By using equations (3.17) and (3.30), and setting $k_n = J_{eddy}\left(x = \frac{nW}{2N}\right)\frac{TW}{2N}$, we obtain

$$\frac{L^{\gamma}_{mutual}}{L^{\alpha}_{mutual}} = K_2 B(\tau) T \pi \sigma W^2 f, \tag{3.33}$$

with

$$K_2 = \frac{\lim\limits_{N,N'\to\infty}\sum\limits_{n=1}^{N}\frac{n}{N}\left(\sum\limits_{m=1}^{N}\overline{M'_{mn}} + \sum\limits_{m'=1}^{N'}\overline{M'_{m'n}}\right) - \lim\limits_{N,N'\to\infty}\sum\limits_{n'=1}^{N'}\frac{n'}{N'}\left(\sum\limits_{m=1}^{N}\overline{M'_{mn'}} + \sum\limits_{m'=1}^{N'}\overline{M'_{m'n'}}\right)}{\lim\limits_{N,N'\to\infty}\sum\limits_{n=1}^{N}\left(\sum\limits_{m=1}^{N}\overline{M'_{mn}} + \sum\limits_{m'=1}^{N'}\overline{M'_{m'n}}\right) + \lim\limits_{N,N'\to\infty}\sum\limits_{n'=1}^{N'}\left(\sum\limits_{m=1}^{N}\overline{M'_{mn'}} + \sum\limits_{m'=1}^{N'}\overline{M'_{m'n'}}\right)}; \tag{3.34}$$

and

$$\frac{L^{\gamma'}_{mutual}}{L^{\alpha}_{mutual}} = K'_2\left(B(\tau) T \pi \sigma W^2 f\right)^2, \tag{3.35}$$

with

$$K'_2 = \frac{\lim\limits_{N,N'\to\infty}\sum\limits_{j=1}^{N}\frac{j}{N}\left(\sum\limits_{i=1}^{N}\frac{i}{N}\overline{M'_{ij}} + \sum\limits_{i'=1}^{N'}\frac{i'}{N}\overline{M'_{i'j}}\right) - \lim\limits_{N,N'\to\infty}\sum\limits_{j'=1}^{N'}\frac{j'}{N'}\left(\sum\limits_{i=1}^{N}\frac{i}{N}\overline{M'_{ij'}} + \sum\limits_{i'=1}^{N'}\frac{i'}{N}\overline{M'_{i'j'}}\right)}{\lim\limits_{N,N'\to\infty}\sum\limits_{j=1}^{N}\left(\sum\limits_{i=1}^{N}\overline{M'_{ij}} + \sum\limits_{i'=1}^{N'}\overline{M'_{i'j}}\right) + \lim\limits_{N,N'\to\infty}\sum\limits_{j'=1}^{N'}\left(\sum\limits_{i=1}^{N}\overline{M'_{ij'}} + \sum\limits_{i'=1}^{N'}\overline{M'_{i'j'}}\right)}. \tag{3.36}$$

Here, the superscript γ and γ' represent the condition of eddy current with the two different methods, respectively.

3.4 Results for Typical Geometries

In the previous section, we divide the inductance calculation of a spiral inductor into three aspects

$$L_{total} = L_{mutual}^{\alpha} + L_{self}^{\beta} + L_{mutual}^{\gamma} = L_{mutual}^{\alpha} + L_{self}^{\beta'} + L_{mutual}^{\gamma'}. \quad (3.37)$$

The term $L_{mutual}{}^{\alpha}$ is constant for fixed inductors and it contributes to at least 20-30% of the total inductance of the metallic trace in normal conditions.

3.4.1 Skin Effect

As L_{self}^{β} and $L_{self}^{\beta'}$ are caused by the skin effect, they may indicate the different importance that each filament (divided as the method in Fig. 3.4) plays within the total self-inductance calculation. Fig. 3.6 plots the filament weight factors (in percents) in the calculation of K_1 and K_1' versus k for one typical inductor ($J_0 = 1A/m^2$, $\sigma = 4.098 \times 10^7 S/m$, $\delta = 1.11\mu m$, f=5GHz, $T = 1.2\mu m$, $W = 8\mu m$, and $l_{total} = 2000\mu m$), where k=1,2..N is the filament number as shown in Fig. 3.4. This figure illustrates the self-inductance weights of the current in each filament with two different methods, and the status of current distribution under skin effect as well. Here, the values of K_1 and K_1' in equations (3.24) and (3.25) respectively indicate the relationship between the self-inductance and frequency. The term L_{self}^{α} in equations (3.24) and (3.25) should be calculated with the definition of *geometric mean distance from itself* in [58] as

$$L_{self}^{\alpha} = 0.002 l_{total} [\ln(\frac{2l_{total}}{W+T}) + 0.5 - 0.00239], \quad (3.38)$$

where l_{total} is the total length of the spiral inductor and $l_{total} >> T$.

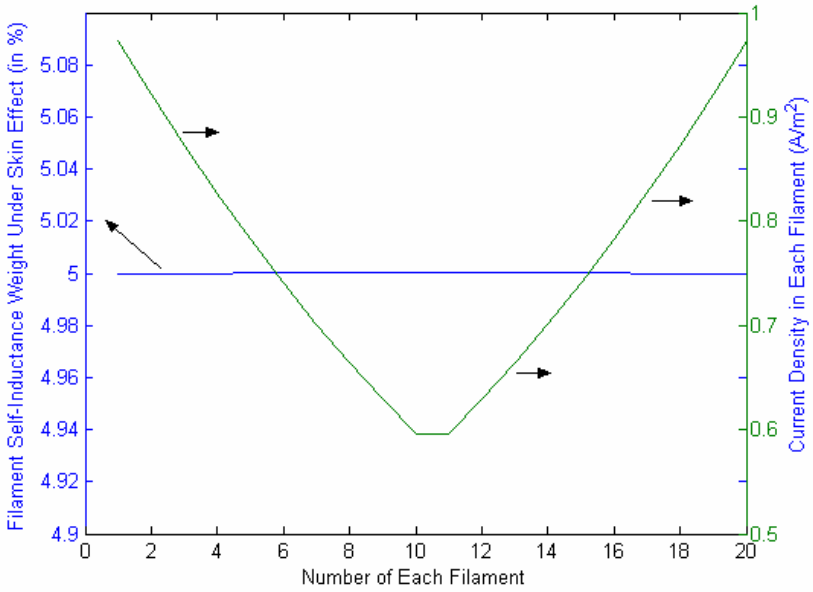

Fig. 3.6: Illustration of the filament self-inductance weights and the current density under skin effect.

In Fig. 3.6, although the theoretical results seem to show that the outer filaments may contribute to relatively less effects on the self-inductance than the inner ones, the weight differences between the filaments are quite insignificant. The alternating percentage between the maximum and the minimum values of the weights is less than 0.1%. One of the reasons for this fact is that the total length l_{total} of the spiral inductor far outweighs the metal thickness T and g in equation (3.18) consequently. Therefore, even if the current is non-uniformly distributed under skin effect, the partial inductance of each single filament, divided as shown in Fig. 3.4, will still remain constant when frequency changes. Thus, the different horizontal filaments are contributing to the same importance for the total inductance of spiral inductor.

3.4.2 Eddy Current

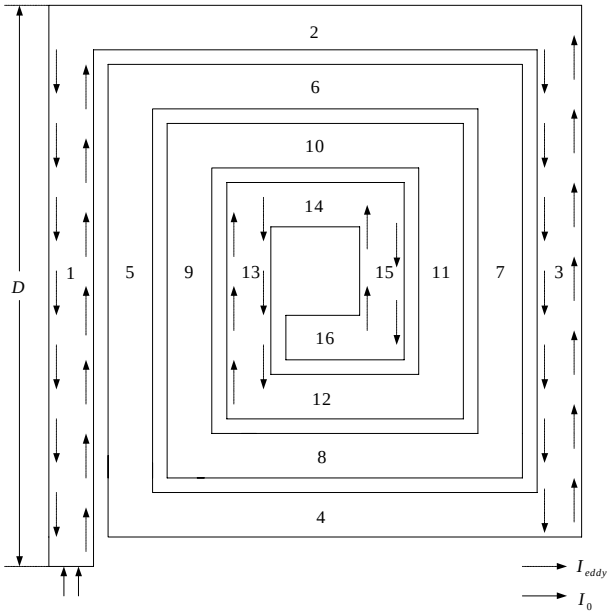

Fig. 3.7: Description of eddy current in inductor.

The variation of mutual inductance caused by eddy current is represented by K_2 or K_2' in equations (3.33) to (3.36). With the same inductor's parameters as above, each theoretically calculated value of K_2 between two parallel straight traces of the inductor is listed in Table 3.1, and the traces are numbered as shown in Fig. 3.7. In calculating the mutual inductance between two unequal parallel filaments (see in Fig. 3.8), we use the formula [58]

$$M_{a,b} = (M_{(b+c),(b+c)} + M_{(b+d),(b+d)} - M_{c,c} - M_{d,d})/2, \tag{3.39}$$

where the terms on the right refer to the mutual inductances between pairs of filaments with equivalent lengths.

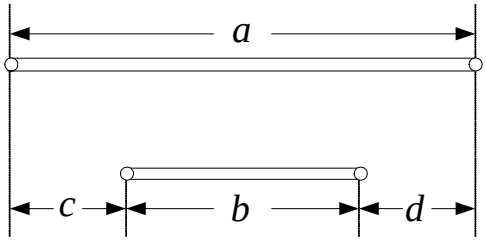

Fig. 3.8: Two unequal parallel filaments.

$K_2^{m,n}$	n=1	n=5	n=9	n=13	n=3	n=7	n=11	n=15
m=1	-	0.0475	0.0301	0.0245	0.0057	0.0061	0.0066	0.0073
m=5	0.0475	-	0.0501	0.0323	0.0061	0.0066	0.0072	0.0079
m=9	0.0301	0.0501	-	0.0536	0.0066	0.0072	0.0078	0.0086
m=13	0.0245	0.0323	0.0536	-	0.0073	0.0079	0.0086	0.0095

$$K_2^{m,n} \approx K_2^{m+k,n+k} \quad (m = 1,5,9,13 \text{ and } k = 1,2,3)$$

$$K_2^{m,n} = K_2^{n,m}$$

Table 3.1: Values of K_2 between straight traces of the inductor.

Table 3.1 indicates that except for the outermost and the innermost turns of a spiral inductor, the eddy current in the other turns causes approximately equal effects in its two adjacent parts that will counteract with each other. While for the traces on different sides of the inductor's center, K_2 is much smaller than for those on the same side. Thus, in our case, as $N \times (W + S)/D \approx 0.25$, over 95% of L_{mutual}^{γ} is caused by the eddy current on the same side. When the inductor has more than 4 turns, the *B*-field and the resulting eddy current in the inner and outer turns of the spiral inductor will probably have different directions [2] (see in Fig. 3.7).

But one more aspect, which one must pay attention to, is that the *B*-fields, which induce the eddy current, can be assumed to be generated by the initial current from the metallic trace mostly. Then, with the Maxwell's equations

$$\nabla \times \vec{H} = \vec{J} + \frac{\partial \vec{D}}{\partial t}, \tag{3.40}$$

and

$$\nabla \times \vec{E} = -\frac{\partial \vec{B}}{\partial t} = -j\omega\vec{B}, \tag{3.41}$$

the *E*-field and the resulting eddy current are actually in quadrature with the excitation current $\vec{J}$ [2].

The basic concept of the overall inductance of a microwave component should represent the phase difference between the excitation voltage and the excitation current directly. Thus, if the eddy current in the metallic trace always has $\frac{\pi}{2}$ phase difference from the excitation current, there will be no significant contributions to the overall inductance of the metallic trace of the spiral inductor from the eddy current in a long time domain as the positive effects will be counteracted by the negative ones in the continuous half periods. Thus, for our first-order estimation, one can neglect the effect of eddy current on the overall inductance calculation (self- and mutual inductance calculations) as the absolute values of either K_2 or K_2' in our two methods for the inductance calculation cannot change effectively the real inductance of the spiral inductor.

3.5 Analysis of Internal Inductance

3.5.1 Internal Inductance of Ground Plane

If the internal inductance of the ground plane, L_{ground}, below the spiral inductor is considered, the total inductance L_{total} associated with the spiral inductor can be expressed as

$$L_{total} = L_{ext} + L_{\text{int}} + L_{ground}, \tag{3.42}$$

where L_{int} refers to the internal inductance of the metallic trace only.

The internal inductance of the ground plane is also governed by the skin effect (i.e., the skin depth associated with the ground plane). In [106], the authors proposed a series of closed-form expressions for the internal inductance of the ground plane as

$$L_{ground} = \frac{2l_{total}}{\pi W \omega \sigma_{ground} \delta_{ground}} \left(\tan^{-1}\left(\frac{W}{2H}\right) - \frac{H}{W} \ln\left(1+\left(\frac{W}{2H}\right)^2\right)\right). \qquad (3.43)$$

Here, σ_{ground} and δ_{ground} are the conductivity and the skin depth of the ground plane, respectively. H is the substrate height between the metallic trace and the ground and W is the width of metallic trace.

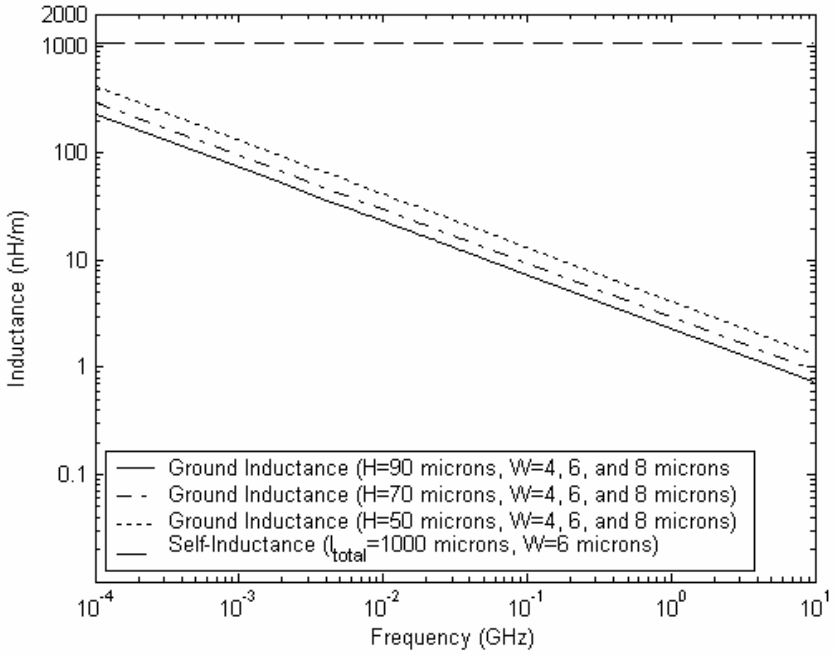

Fig. 3.9: Self- and internal ground inductances for the spiral inductors.

As shown in equations (3.42) and (3.43), the relative importance of L_{ground} as compared to L_{total} is a function of frequency and geometry. Thus, in this section, a series of different geometries are analyzed: the spiral inductors are all on silicon substrate with

$l_{total} = 1000\mu m$, $\sigma_{ground} = 5.8 \times 10^7 S/m$, $T = 1\mu m$, and $\varepsilon_r = 4.5$. The W are $4\mu m$, $6\mu m$, and $8\mu m$; and the H are $50\mu m$, $70\mu m$, and $90\mu m$, respectively.

Fig. 3.9 shows the calculated self-inductance from equation (3.38), and the internal ground plane inductance L_{ground} from equation (3.43). From the simulation results, we can also find that the internal inductance of the ground is much more sensitive to *H* than to *W*. With the increasing of *H*, the internal inductance of the ground will then contribute less effect to the overall inductance of the spiral inductor at any frequency.

With equation (3.38), the theoretical self-inductance for the spiral inductors (T=$1\mu m$ and $l_{total} = 1000\mu m$) with $8\mu m$, $6\mu m$, and $4\mu m$ metal width will be 1024nH/m, 1074nH/m, and 1141nH/m, respectively. Thus, although the internal ground inductance at low frequencies is comparable to the self-inductance of the whole metallic trace [106], it will be a bit small compared to the self-inductance at high frequencies. When the frequency is above 0.1GHz, L_{ground} is about 1% of the self-inductance only. Furthermore, if the overall mutual inductance of the spiral inductor is considered, L_{ground} will be less than 0.7-0.8% of the exact L_{total} at frequencies above 0.1GHz.

3.5.2 Internal Inductance of Metallic Trace of Spiral Inductors

The external inductance of conductor coincides with the asymptotic value of inductance at high frequencies, and corresponds to the limit where all current flows on the wire

surface only and no fields exist inside the conductor [107]. The internal inductance of conductor is the difference between the low- and high-frequency limits and is due to the field penetration inside the conductor. Typically, the internal inductance accounts for less than 10% of the total low-frequency (partial) inductance of a single wire, or open loop. For closely spaced loop, due to the cancellation of self- and mutual inductances, the internal inductance can be a significant portion of the loop inductance [107].

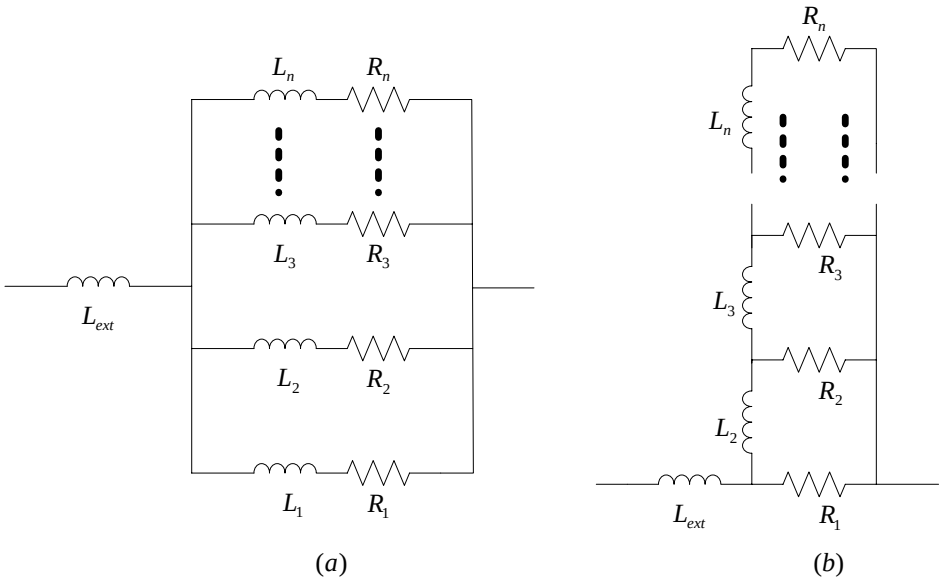

Fig. 3.10: Equivalent circuit models for skin effect.

In the previous sections, we find that the partial external inductance of each single filament in Fig. 3.4 can be assumed to be constant with the change of frequency, even when the current is non-uniformly distributed in the conductor. Thus, the total external inductance of the whole inductor is nearly a constant (see pp. 69, Fig. 3.6) and affected marginally by skin effect. However, for the overall internal inductance, things are quite different. For example, in the circuit model of Fig. 3.10 (*a*) for skin effect [107]-[109], L_{ext} refers to the external inductance, and the internal inductance L_{int} can be calculated from the right hand side in the model. Thus, we can find that due to the series resistance

R_n of each filament under skin effect, the theoretical internal inductance of the conductor will usually be frequency-dependent even if the partial internal inductance L_n of each filament is constant and equivalent at different frequencies. But the generation of the model in Fig. 3.10 (*a*) requires extensive calculations, and no compact expressions are given [107].

Fig. 3.10 (*b*) shows another ladder equivalent circuit for skin effect utilized in [107], and [110]-[112]. The ladder topology of Fig. 3.10 (*b*) was introduced firstly by Wheeler [111] and developed by Yen *et al*. [112] and Kim and Neikirk [110]. Kim and Neikirk provided a technique based on the ad-hoc assumption of a geometric progression of the resistance and inductance values [110] as

$$R_{n+1} = R_n / RR, \tag{3.44}$$

and

$$L_{n+1} = L_n / LL. \tag{3.45}$$

Here, the values of L_n may not be equivalent because they represent the inductances which isolate progressively the resistors R_n and the filaments are not required to be divided uniformly. Once R_1 and L_2 are empirically set, the ratios RR and LL are calculated to satisfy constrains on the low frequency resistance R_{dc} and internal inductance L_{int}. The free parameters in the model are

$$\alpha_R = R_1 / R_{dc}, \tag{3.46}$$

and

$$\alpha_L = L_{\text{int}} / L_2, \tag{3.47}$$

which are empirically fitted to exact analytical results or measurements.

Although the original model as above was fitted on nonrectangular cross sections, the authors of [107] recalibrated it from numerical simulations and re-determined the parameters α_R and α_L for a wide range of rectangular cross sections with different W/T ratios. The simulation results of the total inductance shown in [107] with Fig. 3.10 are quite satisfactory and in accordance with the data obtained from FastHenry results [113].

The formula for the total internal inductance L_{int} of a conductor with width *W*, thickness *T*, and length l_{total} at low frequencies is given by the expression [107]

$$L_{\text{int}} = 10^{-9} l_{total} (0.3 + 0.28 e^{-0.14 W/T}), \tag{3.48}$$

where the wire length l_{total} is in centimeters and *W*>*T* (the ratio *T*/*W* should be substituted for *W*/*T* in the opposite case). This equation is used to separate the internal inductance from the external inductance at low frequencies.

Then, by choosing *n*=4, $\alpha_R = 10$, $\alpha_L = 3.2$, and combining the circuit model in Fig. 3.10 (*b*) with equations (3.44) to (3.48), Fig. 3.13 shows the behavior of the computational internal inductance of a series of rectangular cross-section, copper-traced spiral inductors with $6\mu m$ width and $1\mu m$ metal thickness below 10GHz. The l_{total} s of them are $914\mu m$, $1320\mu m$, $1775\mu m$, $2281\mu m$, $2837\mu m$, and $3443\mu m$, respectively.

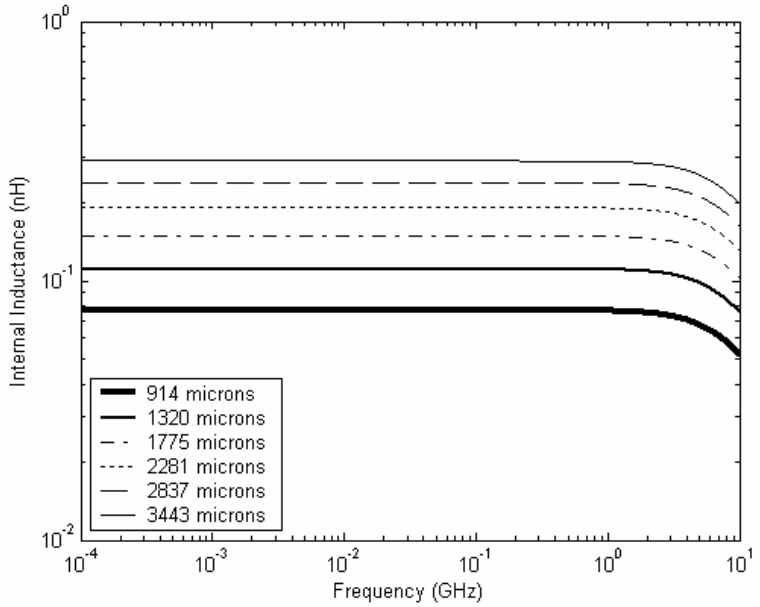

Fig. 3.11: Computational skin-effect internal inductance of solid rectangular conductors of pure copper.

Fig. 3.11 shows that the internal inductance of longer wires will decrease more at any frequency than shorter ones. For fixed metal width and thickness as our examples, the internal inductance values of the wires will usually be 20%-30% smaller at 10GHz than the values around *dc*. Furthermore, by comparing the results from equation (3.48) with those of equation (3.38), it is easy to find that the internal inductance accounts for 3%-4% in the total self-inductance and 2%-3% in the total inductance of the spiral inductor at low frequencies. Thus, the effect of internal inductance on the reduction of the total inductance from 0.1GHz to 10 GHz will be from 0.4% to 0.9%.

3.6 Experimental Results and Discussions

In this section, we compare the predicted inductance behavior from all the proposed approximate expressions with measured data from some sample inductors. We fabricated a series of circular copper-traced spiral inductors on silicon substrate. The layout

parameters of the inductors include $6\,\mu m$ width, $2\,\mu m$ spacing, $1\,\mu m$ metal thickness, and $75\,\mu m$ inner dimension. The heights between the metallic traces and the underpass of the spiral inductors and the ground plane are $0.46\mu m$ and $70\mu m$, respectively. The numbers of turns of Inductor 23 to Inductor 28 are 3, 4, 5, 6, 7, and 8, respectively. Thus, the total lengths of the inductors are $914\mu m$, $1320\mu m$, $1775\mu m$, $2281\mu m$, $2837\mu m$, and $3443\mu m$, respectively. The measured data are taken with the HP8510C vector network analyzer and the HP nonlinear network measurement system.

The measured data for the inductance is extracted from the following expression $L_s(f) = \frac{imag((-Y_{12} - 2j\pi f C_s)^{-1})}{2\pi f}$. Here, C_s refers to the total parasitic capacitance value of the inductor as shown in the circuit model in Fig. 3.12 and can be calculated through $n \cdot W^2 \cdot \frac{\varepsilon_{ox}}{t_{ox}}$ [41]. The simulated inductance, which is derived from the previous Sections 3.2 to 3.5, is given as

$$L_{total}(f) = L_{ext} + L_{\text{int}}(f) = L_{mutual}^{ext} + L_{self}^{ext} + L_{\text{int}}(f) + L_{ground}(f). \qquad (3.49)$$

Here, the theoretical self-inductance L_{self}^{ext} of a conductor with rectangular cross section can be calculated from equation (3.38), and equations (3.43) and (3.48) are utilized to separate the internal inductances of the metallic trace and the ground plane from the external inductance at low frequencies. The internal inductances of the metallic traces of spiral inductors are predicted with the method of ladder circuit model as illustrated in Fig. 3.10 (*b*) in Section 3.5.2.

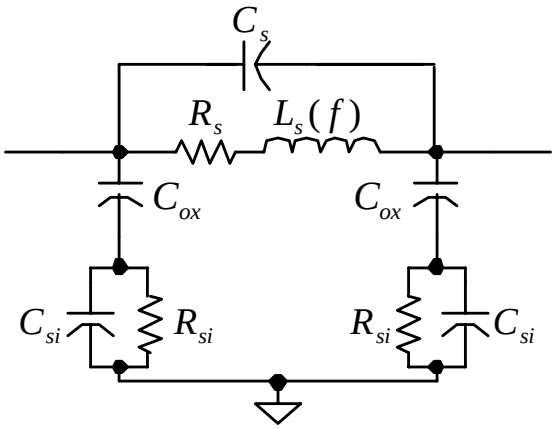

Fig. 3.12: Equivalent circuit of an inductor.

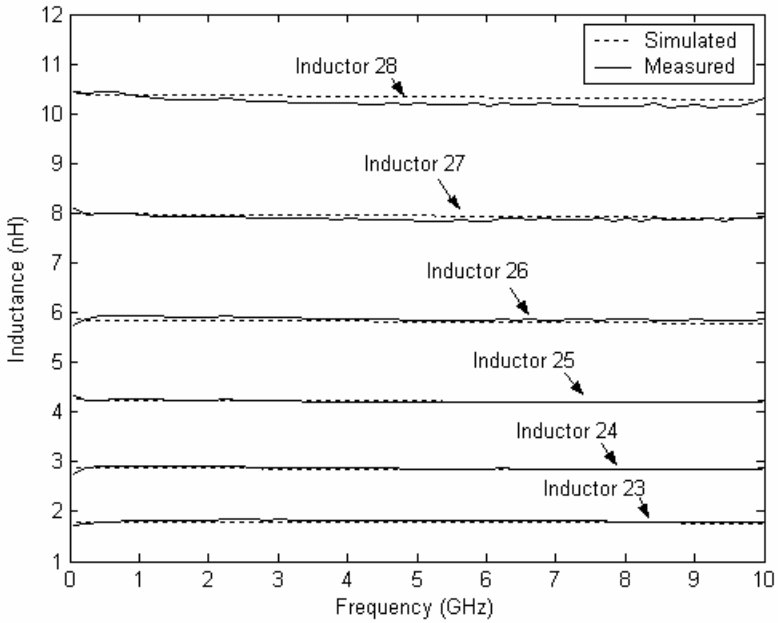

Fig. 3.13: Comparison between the measured and simulated inductance of spiral inductors.

As illustrated in Fig. 3.13, both the measured and the simulated inductances of spiral inductors can be found to decrease slightly with the increasing of frequency. Fig. 3.13 also provides a good agreement for the prediction of inductances of Inductors 23-28. The plots show that the typical simulation errors of inductances are within the range of 0.5%-1% for Inductors 23-25 and are within the range of 1%-2% for Inductors 26-28.

Once we neglect the parasitic capacitance effect in the inductance extraction, both the measured and the circuit-simulated inductances will be increasing functions of frequency for all these spiral inductors. But in reality, the total physical inductance should decrease as a function of frequency due to the skin effect, as illustrated in Fig. 3.13.

But all of the previous analysis can only be part of the comprehensive investigation as they cannot explain the phenomenon why the inductance value of some spiral inductors may decrease 5%, or even 10% (as reported in [114]), from 0.1GHz to 10GHz. As for a highly conductive substrate, the eddy current generated in the bulk substrate will lead to a significant decrease in inductance as a function of frequency, as the current partially cancels the magnetic field generated by the device. The inductance reduction with frequency may also be induced by the substrate skin effect which increases negative mutual inductance [34], and [114]-[115]. When frequency increases, under skin effect mode, the longitudinal current near silicon-silicon oxide interface will usually reduce the inductor inductance [114].

3.7 Conclusion

The total inductance of a spiral inductor can be separated into two aspects, self- and mutual inductances; and generally, it consists of both external and internal inductances. The non-uniform current distribution in the metallic trace of the inductor is caused by skin effect and eddy current mainly.

The skin effect will always cause current to concentrate to the surface of the metallic trace. In this chapter, two different methods are derived and utilized to predict both the self- and the mutual inductances of spiral inductor under skin effect. By combining with some former predictions with equivalent circuit diagrams for the skin effect, the internal inductance of spiral inductor is also investigated and analyzed.

According to the law of Faraday-Lenz, eddy current is generated in the metallic trace, due to the non-uniform *B*-field around the spiral inductor. An electrical field is then magnetically induced that will generate the eddy current in the metallic traces of the spiral inductor. The direction of eddy current is such that they oppose the original change in magnetic field. But they are always in quadrature with the excitation current. Therefore for our first-order estimation, the eddy current will have no effective contributions to both the self- and mutual inductances between the traces of the inductor.

Compared with the external inductance, the more essential parts for the frequency-dependent inductance of spiral inductor are found to be caused by the internal inductances of the metallic trace and the ground plane. Their effects are analyzed in this chapter.

A further analysis of how the inductance of the spiral inductor changes due to skin effect and eddy current in the dielectric substrate below is more involved and shall be referred to the future work.

CHAPTER 4

DETAILED EXPLANATION OF THE HIGH QUALITY CHARACTERISTICS OF SYMMETRICAL OCTAGONAL SPIRAL INDUCTORS

4.1 Introduction

At radio frequencies (RF), the usage of on-chip silicon spiral inductors in *LC* tank circuits is limited by the achievable quality factor (*Q*). The quality factor of a spiral inductor is seriously affected by three capacitance components. They are the series feed-forward capacitance, the capacitance between the spiral metallic trace and substrate, and lastly, the substrate capacitance. In the physical modeling of an inductor [32], [41], [55], and [58], the series feed-forward capacitance accounts for the capacitance due to the overlaps between the spiral metallic trace and the underpass [6] and [67].

In Chapters 2 and 3, we show our improved calculations for the resistance and inductance of planar, non-symmetrical spiral inductors. To increase the overall *Q*-factor

of silicon spiral inductor, one usually has to resort to the use of symmetrical spiral inductor, instead of the conventional non-symmetrical spiral inductor, which can decrease the feed-forward capacitance of the inductor. In this chapter, an attempt to provide a new and comprehensive explanation on how the symmetrical, arbitrarily-shaped spiral inductor helps to improve the *Q*-factor characteristics over that of the corresponding conventional non-symmetrical spiral inductor is made. It is hope with this new understanding, alternate forms of symmetrical spiral inductor can be derived.

4.2 Theoretical Analysis

In this section, the differences on the feed-forward capacitance value, series resistance and inductance values, and the *electric and magnetic center* (EMC) between symmetrical and non-symmetrical spiral inductors are discussed. The effects of these differences on the *Q*-factor are analyzed and presented.

4.2.1 Change of C_s

Fig. 4.1 shows the difference between a symmetrical and a non-symmetrical spiral inductor on silicon substrate. For the ease of explanation, the circuit dimensions corresponding to both types of inductors are assumed to be equal. A simplified equivalent circuit model for the spiral inductor is presented in Fig. 4.2. In this model, the series branch consists of the spiral inductor's inductance L_s, the metal resistance R_s, and the

series feed-forward capacitance C_s. For most practical inductors, it is sufficient to model C_s as the sum of all overlap capacitances, which is equal to [41]

$$C_s = n \cdot W^2 \cdot \frac{\varepsilon_{ox}}{t_{ox}}, \tag{4.1}$$

where n is the number of overlaps, W is line-width of the metallic trace, ε_{ox} and t_{ox} denote the dielectric constant and thickness of the oxide layer between the metallic trace and underpass, respectively.

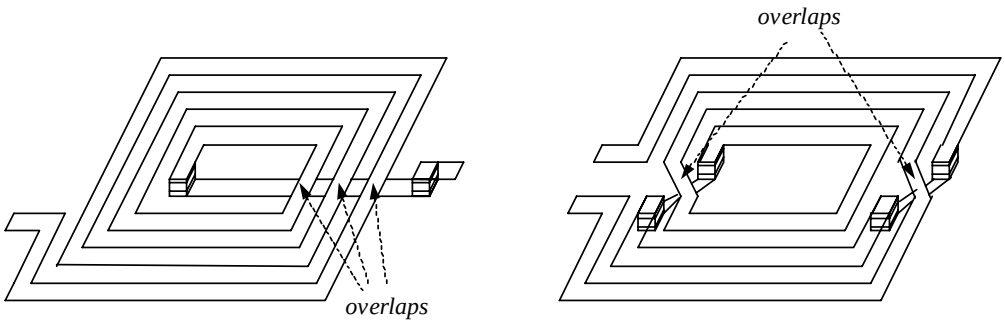

(*a*) (*b*)

Fig. 4.1: (*a*) A non-symmetrical spiral inductor. (*b*) A symmetrical spiral inductor.

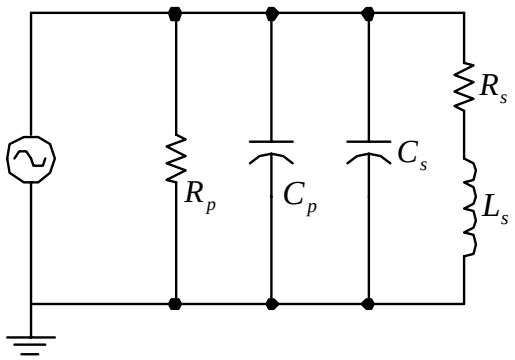

Fig. 4.2: A typical circuit model for a spiral inductor.

Fig. 4.1 illustrates that for the same inner dimension, width, spacing, and number of turns of a spiral inductor, the symmetrical spiral inductor needs one less overlap than the

conventional, non-symmetrical spiral inductor. As such, intuitively, the capacitance C_s, caused by the overlaps of the symmetrical spiral inductor, will be 1/*n* times smaller than that of the non-symmetrical spiral inductor. Furthermore, in the symmetrical case, each overlapping area between the metallic traces and the underpass is no longer W^2 as in the non-symmetrical case, and it usually becomes a bit smaller. Thus, from equation (4.1), we find that the C_s will decrease more.

In [6], Yue expressed the *Q*-factor of a typical spiral inductor as

$$Q = \frac{\omega L_s}{R_s} \cdot \frac{R_p}{R_p + [(\omega L_s / R_s)^2 + 1] R_s} \cdot \left[1 - \frac{R_s^2 (C_s + C_p)}{L_s} - \omega^2 L_s (C_s + C_p) \right]. \tag{4.2}$$

In this equation, the values of R_p and C_p are irrelevant with respect to C_s as

$$R_p = \frac{1}{\omega^2 C_{ox}^2 R_{si}} + \frac{R_{si} (C_{ox} + C_{si})^2}{C_{ox}^2}, \tag{4.3}$$

and

$$C_p = C_{ox} \frac{1 + \omega^2 (C_{ox} + C_{si}) C_{si} R_{si}^2}{1 + \omega^2 (C_{ox} + C_{si}) R_{si}^2}. \tag{4.4}$$

Here, R_{si}, C_{si}, and C_{ox} describe the substrate parasitics as shown in Fig. 3.12. In general, a MOS microstrip structure can be modeled by a three-element network comprised of R_{si}, C_{si}, and C_{ox}. C_{ox} represents the oxide capacitance whereas R_{si} and C_{si} represent the silicon substrate resistance and capacitance, respectively. The physical origin of R_{si} is the silicon conductivity which is predominately determined by the majority carrier concentration. C_{si} models the high-frequency capacitive effects occurring in the semiconductor. For spiral inductors on silicon, the lateral dimensions are typically a few

hundred microns which are much larger than the oxide thickness and are comparable to the silicon thickness. As a result, the substrate capacitance and resistance are approximately proportional to the area occupied by the inductor and can be expressed by

$$C_{ox} = \frac{1}{2} lW \frac{\varepsilon_{ox}}{t_{ox}}, \tag{4.5}$$

$$C_{si} = \frac{1}{2} lWC_{sub}, \tag{4.6}$$

$$R_{si} = \frac{2}{lWG_{sub}}, \tag{4.7}$$

where C_{sub} and G_{sub} are the capacitance and conductance per unit area for the silicon substrate. ε_{ox} and t_{ox} denote the dielectric constant and thickness of the oxide layer between the inductor and the substrate. The area of the spiral inductor is equal to the product of the total inductor length (l) and width (W). The factor of two in equations (4.5) to (4.7) accounts for the fact that the substrate parasitics are assumed to be distributed equally at the two ends of the inductor. C_{sub} and G_{sub} are functions of the substrate doping and are extracted from the measured results. For inductors fabricated with the same technology, C_{sub} and G_{sub} do not vary significantly. As a result, R_{si} and C_{si} scale with l and W only.

So, it is obvious that if C_s decreases, the last term $\left[1 - \frac{R_s^2 (C_s + C_p)}{L_s} - \omega^2 L_s (C_s + C_p)\right]$ in equation (4.2) will increase. This will eventually result in an enhancement on the overall quality factor of the spiral inductor. Such

conclusion is also valid for an arbitrarily-shaped, symmetrical spiral inductor and as an example, the octagonal symmetrical spiral inductor is referred in the next section.

4.2.2 Changes of R_s and L_s

The results in [116] showed that the series resistance R_s of an octagonal or circular shaped inductors is smaller by 10% than that of a square-shaped spiral inductor with the same inductance value. In comparison with the square-shaped spiral inductor, from equation (4.2), one can conclude that the quality factor of both the circular and octagonal spiral inductors will become larger with a decrease of R_s.

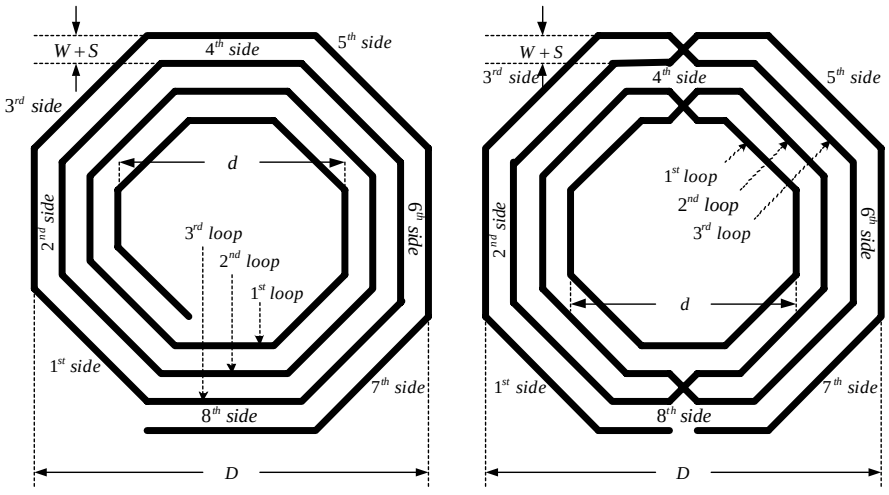

(*a*) (*b*)

Fig. 4.3: (*a*) A non-symmetrical, octagonal spiral inductor. (*b*) A symmetrical, octagonal spiral inductor.

But another thing which should be mentioned here is that once the number of inductor turns is more than 2, the symmetrical structure of an inductor will usually require more vias than the non-symmetrical one. This will sometimes influences the *Q*-

factor of the inductor since each new turn involves level interchanges, which accrue the resistance [117].

As shown in Fig. 4.3, *W*, *S*, *d*, and *D* refer respectively to the width, spacing of the metallic traces, inner dimension, and outer dimension of the spiral inductor. For the same *W*, *S*, *d*, and number of turns *N*, the difference in the total length of the spiral inductor between the non-symmetrical and symmetrical spiral inductor is about $0.2(N-1)(W+S)$. This factor usually amounts to less than 1% of the total length of the spiral inductor. As a result, with equations (3), (8), and (9) in [118], the self-inductances for both the octagonal, non-symmetrical spiral inductor and the octagonal, symmetrical spiral inductor are found to be approximately the same. Thus, the difference between the measured inductance values of the two types of spiral inductor is solely due to the magnetic coupling effect between different arms.

4.2.3 Change of the Electric and Magnetic Centers

Fig. 4.4 shows the simplified lumped element model of a typical spiral inductor. Here, we let $l_{i,n}$ and $r_{i,n}$ represent respectively the individual inductance and series resistance observed from the i^{th} side in the n^{th} loop of the spiral inductor. $l_{i,n}$ is the sum of the n^{th} loop's self-inductance at the i^{th} side and the mutual inductance observed from the i^{th} side of the spiral inductor. In the case of an octagonal, symmetrical spiral inductor, the EMC is also the geometric center of the inductor. Then, as all the sides of the spiral inductor are equidistant from the EMC, the inter-magnetic coupling observed can be taken to be the

same throughout. In this connection, it is natural to assume that all the $l_{i,n}$ s observed from the sides of the spiral inductor will have the same inductance value.

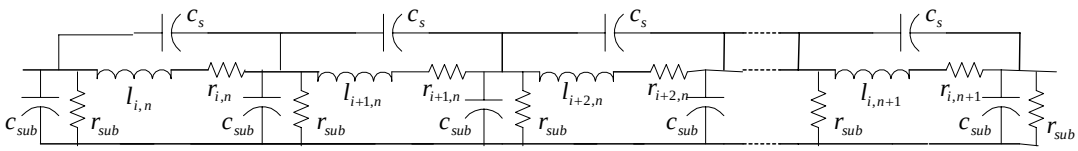

Fig.4.4: A simplified lumped element model of a spiral inductor.

Comparing to the symmetrical, octagonal spiral inductor, we observe that the non-symmetrical spiral inductor does not have an ideal geometric center. The respective EMC of the non-symmetrical spiral inductor is off-set to one side. As such, the magnetic coupling will not be distributed equally throughout the whole spiral inductor. The half loop that is closer to the EMC will result in larger magnetic coupling and hence, larger values of $l_{i,n}$ s in this respective half-loop of the spiral inductor. When the inductor structure is octagonal, one would obtain

$$\begin{cases} l'_{2n-1} = (1-\alpha_n) l_n / 2, \\ l'_{2n} = (1+\alpha_n) l_n / 2, \end{cases} \tag{4.8}$$

where n=1,2,…,N, l_n refers to the total inductance value of the n^{th} loop of the symmetrical octagonal spiral inductor, N is the total number of inductor turns, and α_n is a positive proportionality factor which relates the effect of the off-set EMC to the n^{th} loop symmetrical octagonal spiral inductor. l'_{2n} refers to the mutual inductance value observed from the half n^{th} loop that is closer to the EMC in the non-symmetrical octagonal spiral inductor whereas l'_{2n-1} refers to the mutual inductance value observed from another half n^{th} loop that is further away from the EMC.

By representing the spiral inductor as a cascade of series networks (see Fig. 4.4) and neglecting initially the fringing capacitance between opposite sides, the whole input impedance of the n^{th} loop of the non-symmetrical spiral inductor in terms of the theoretical *ABCD*-parameters is then described as

$$\begin{aligned} Z'_{in} &= A'_{12} = (r_n + j\omega l'_{2n-1}) + (r_n + j\omega l'_{2n}) + (j\omega c_{sub} + 1/r_{sub})(r_n + j\omega l'_{2n-1})(r_n + j\omega l'_{2n}) \\ &= \left[2r_n + (r_n^2 - \omega^2 l_n^2)/r_{sub} - 2\omega^2 l_n r_n c_{sub} + \omega^2 l_n^2 \alpha_n^2 / r_{sub}\right] \\ &\quad + j\left[2\omega l_n + \omega c_{sub}(r_n^2 - \omega^2 l_n^2) + 2\omega l_n r_n / r_{sub} + \omega^3 c_n l_n^2 \alpha_n^2\right], \end{aligned} \tag{4.9}$$

whereas for the symmetrical spiral inductor, we obtain

$$Z_{in} = \left[2r_n + \frac{r_n^2 - \omega^2 l_n^2}{r_{sub}} - 2\omega^2 l_n r_n c_{sub}\right] + j\left[2\omega l_n + \omega c_{sub}(r_n^2 - \omega^2 l_n^2) + \frac{2\omega l_n r_n}{r_{sub}}\right]. \tag{4.10}$$

The effective quality factor, Q_{eff} of a spiral inductor can be calculated from [119]-[120] as

$$Q_{eff} = \frac{\mathrm{Im}[Z_{in}]}{\mathrm{Re}[Z_{in}]}, \tag{4.11}$$

where $\mathrm{Re}[Z_{in}]$ and $\mathrm{Im}[Z_{in}]$ are respectively the real and imaginary parts of the input impedance of a spiral inductor. Then, with equations (4.9) and (4.10), we have

$$Q'_{eff} = \frac{\mathrm{Im}[Z'_{in}]}{\mathrm{Re}[Z'_{in}]} < Q_{eff} = \frac{\mathrm{Im}[Z_{in}]}{\mathrm{Re}[Z_{in}]}, \tag{4.12}$$

when

$$r_n c_{sub} < l_n r_n /(r_{sub})^2 + \omega^2 l_n r_n c_{sub}^2 + l_n / r_{sub}. \tag{4.13}$$

In equations (4.11) to (4.12), Q_{eff} and Q'_{eff} denote respectively the effective *Q*-factors of a symmetrical and a non-symmetrical spiral inductor. In practice, c_{sub} is always

smaller than $l_n/(r_{sub}r_n)$ or $l_n/(r_{sub})^2$. Therefore, it is easy to make equation (4.13) satisfied. In this connection, the symmetrical spiral inductor will provide a larger quality factor as compared to the non-symmetrical spiral inductor.

4.3 Experimental Results

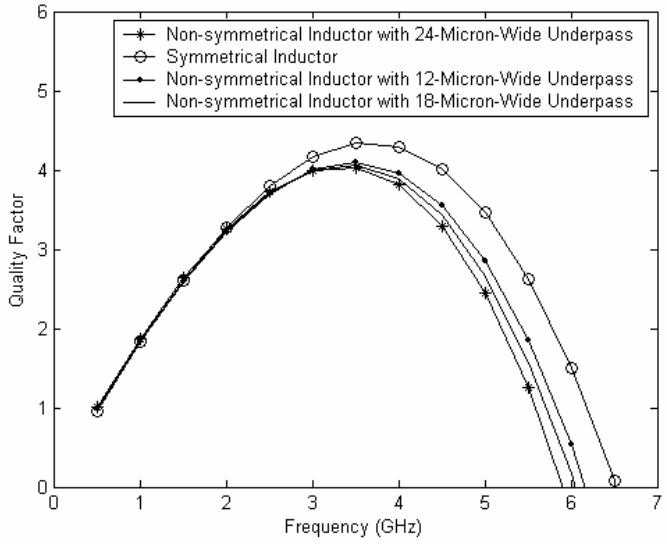

(*a*)

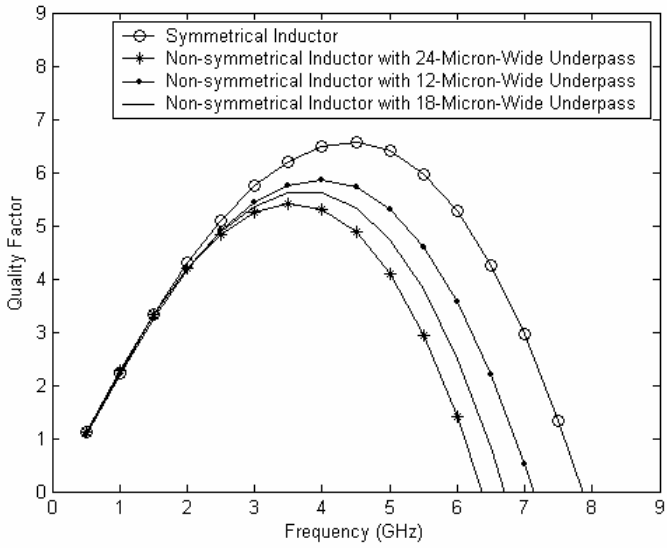

(*b*)

Fig. 4.5: Comparisons of the simulated quality factors between symmetrical and non-symmetrical spiral inductors.

Fig. 4.5 (*a*) describes the simulation results of the *Q*-factor of four square inductors, one symmetrical and three non-symmetrical, with all 4 turns, 366 μm outer dimension, 24 μm line-width, and 6 μm spacing on a upper SiO_2 layer (0.5 μm) and a lower silicon layer (20 μm) substrate. The only difference between these three non-symmetrical inductors is that the widths of the underpass are 12 μm, 18 μm, and 24 μm, respectively. Fig. 4.5 (*b*) describes the simulation results of the *Q*-factor of four square inductors, one symmetrical and three non-symmetrical, with all 5 turns, 366 μm outer dimension, 24 μm line-width, and 6 μm spacing on a upper SiO_2 layer (20 μm) and a lower silicon layer (50 μm) substrate. The only difference between these three non-symmetrical inductors is that the widths of the underpass are 12 μm, 18 μm, and 24 μm, respectively. The heights between the metallic traces and the underpass for all of these inductors are 0.5 μm. From Fig. 4.5, we can find that the symmetrical spiral inductor provides a higher *Q*-factor and a higher resonance frequency than the non-symmetrical ones. While within the non-symmetrical inductor cases, the inductor with narrower underpass can provide relatively higher *Q*-factor than the one with wider underpass. These simulation results agree with our predictions of the effect of the feed-forward capacitance C_s on *Q*-factor in Section 4.2.1, as C_s in equations (4.1) and (4.2) is smaller of the symmetrical structure than of the non-symmetrical structure, and then C_s is also smaller with narrower underpass than with wider underpass in the non-symmetrical inductors. With the increasing of the peak value of *Q*-factor, Q_{MAX}, the inductor will usually provide higher resonance frequency f_{res}, and higher frequency when the Q_{MAX} appears.

As it is relatively difficult to test out separately the effects of EMC's shift from the symmetrical inductor to the non-symmetrical one, we may modify the 4-turn symmetrical, square inductor above to be with irregular spacing between turns to verify our analysis. Compared with the general symmetrical inductor with all $6\,\mu m$-spacing, our modified 'symmetrical' inductor with irregular spacing has $3\,\mu m$-spacing between each pair of adjacent traces around one corner and $9\,\mu m$-spacing between each pair of adjacent traces around the opposite corner. This makes the inner turns of the inductor 'crowd' to one corner together. The advantage of such attempt is that this will not change the total spiral length *l*, the metal area Wl, and the overlapping areas between the metallic traces and the underpass of the symmetrical inductor, except the inductor's EMC. Thus, the theoretical values of the circuit components in Fig. 4.2 can still be approximated to be constant.

From Fig. 4.6, we can conclude that the shift of the inductor EMC from the geometric center of the spiral inductors to anywhere else will usually cause the Q_{MAX} to become a bit lower. However, the f_{res}, and the frequency where the Q_{MAX} appears, do not exhibit any significant changes. Similar results can also be achieved from one pair of 3-turn octagonal symmetrical inductors with respectively regular spacing ($6\,\mu m$) and irregular spacing (again $3\,\mu m$ and $9\,\mu m$, respectively), as shown in Fig 4.6. Thus in general, the effect of the EMC shift on the *Q*-factor is not as significant as that of the overlaps and C_s.

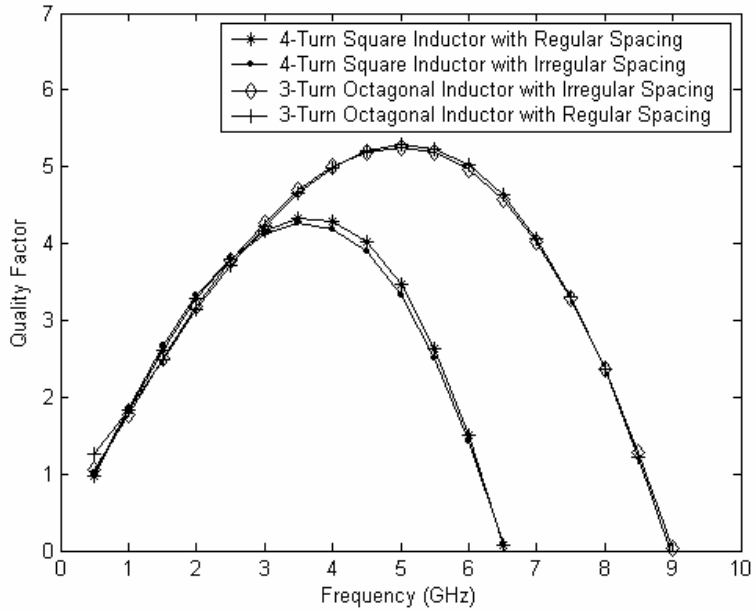

Fig. 4.6: Comparisons of the simulated quality factors between the symmetrical spiral inductors with regular spacing and irregular spacing (24 μm metal width, and 366 μm outer dimension).

We designed several symmetrical, aluminum-traced, octagonal spiral inductors having different numbers of turns or outer dimensions. Except for Inductor 29 to Inductor 31 which have totally 3 turns, all of the other inductors have 5 turns. The outer dimensions of these inductors, numbered from Inductor 29 to Inductor 35, are 187 μm, 233 μm, 280 μm, 142 μm, 187 μm, 233 μm, and 280 μm, respectively. All these inductors have 8 μm line-width and 4 μm spacing between the metallic turns. These inductors are fabricated with a 5 μm oxide dielectric separation between the inductor and the silicon substrate with the thickness of 200 μm. The two-port *S*-parameters for all of the inductors are measured up to 15GHz with IC-CAP and de-embedding technique.

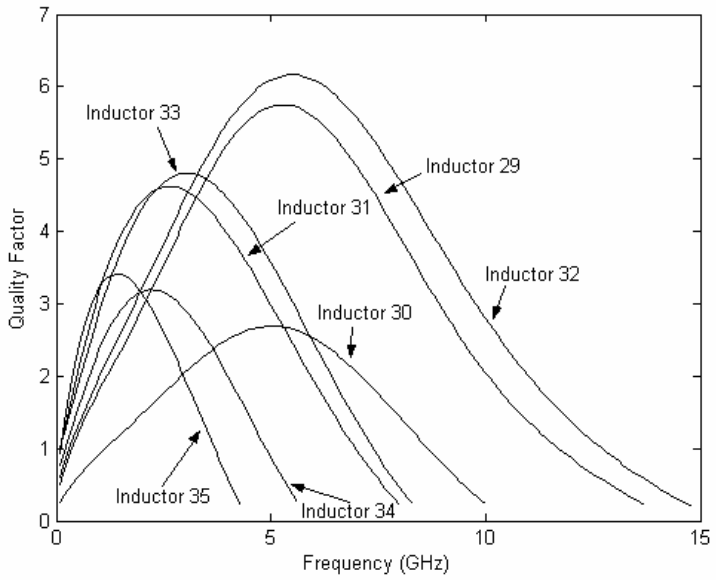

Fig. 4.7: Measured quality factors for various spiral inductors.

Fig. 4.7 shows the measured *Q*-factors of our inductors. Within each group of inductors with the same number of turns, the maximum *Q*-factor observed belongs to the smallest inductor, which has the shortest length of metallic trace. With C_s remaining relatively unchanged within each group, this high quality factor is mainly due to the lower R_s value observed from the smallest spiral inductor.

At low frequencies (particularly lower than 1GHz), the *Q*-factor can be well described by $\omega L_s / R_s$ as the last two terms in equation (4.2) have values close to unity [6]. From Fig. 4.7, it is noted that with the increase of the number of turns within each group of inductors with equal outer dimension, the inductance value increases more than the series resistance value. Thus, the inductor with more turns can provide higher *Q*-factor values than the inductor with less turns at low frequencies. However, with the increase of frequency, eddy current [2] will become more significant and hence, the

resistance value R_s will then increase dramatically, especially for the inductors with more turns. In this connection, the overall *Q*-factor of the inductor with more turns becomes progressively lower than the inductor with less turns, at relatively higher frequencies.

From Fig. 4.7, we note that in the case of the same number of turns, the measured resonant frequencies decrease with an increase of the outer dimension of inductors (from Inductor 29 to Inductor 31, and from Inductor 32 to Inductor 35). While with the increase of the number of spiral turns, more overlaps are resulted and thus, the effect due to the capacitance C_s becomes predominant. The theoretical resonant frequency f_{res}, derived from the last term of expression (4.2), is

$$f_{res} = \frac{1}{2\pi}\sqrt{\frac{L_s - R_s^2(C_s + C_p)}{L_s^2(C_s + C_p)}}. \tag{4.14}$$

This expression shows that with an increase of C_s, the resonant frequency will decrease. Within each group of inductors with the same outer dimension, the capacitance, C_s, will become larger when the number of turns increases. As a result, this usually constitutes a decrease in both the maximum quality factor and the resonance frequency (see in Fig. 4.7).

Due to the unavailability of the corresponding non-symmetrical octagonal inductors, which have the same parameters with our designed symmetrical ones, we are unable to provide the physical comparison results of the measured *Q*-factors. These comparisons will be referred to the future work.

4.4 Conclusion

Compared with the non-symmetrical structure, the symmetrical octagonal spiral inductor can reduce the coupling capacitance of the overlaps of the metallic traces. Furthermore, as the EMC of the symmetrical case is the accurate geometric center of the spiral inductor, it can balance effectively the effect of inductance coupling between different sides of the inductor. All these aspects will provide higher quality factor and resonance frequency for the symmetrical inductor.

The number of overlaps between the underpass and the metallic trace of the inductor can reduce the *Q*-factor significantly in high frequency range. However, in lower frequency range, when the total number of inductor turns is fixed, one predominant factor which influences the *Q*-factor is the outer dimension of the inductor.

CHAPTER 5

AN IMPROVED MODEL OF TWO-LAYER SPIRAL INDUCTOR WITH EDDY CURRENT EFFECTS IN SUBSTRATE

5.1 Introduction

In addition to the various single-layer spiral inductors as discussed in the previous chapters, multi-layer inductors have also gained great importance in the design of integrated silicon RF transmitters and receivers. For this reason, the analysis and optimization of such structures are of great importance [32] and [81].

The substrate effects on the performance of metal-insulator-metal (MIM) spiral inductors are critical to silicon RF IC's design [81]. The effects of substrate RF losses from eddy current on the characteristics of silicon-based integrated inductors and transformers have, up to now only, been experimentally studied in [80] and [83]. It is thus our intention in this chapter to incorporate the eddy current effects in equivalent circuit method for the case of multi-layer spiral inductors.

Due to the more significant inductance coupling compared with the single-layer inductors, multi-layer structure can provide relatively larger inductance values and higher quality factors [64] and [69]. For a two-layer case, the total inductance of the whole inductor is $L_1 + L_2 + 2M$, where L_1 and L_2 are the self-inductances of the two spiral metallic traces and M is the mutual inductance between the two layers. In a two-layer inductor, the two spiral metallic traces are identical ($L_1 = L_2 = L$) and the mutual coupling between the two layers is usually quite strong ($M \approx \sqrt{L_1 L_2} = L$). The total inductance is therefore increased by nearly a factor of 4. Similarly, for an *n*-layer inductor, the total inductance is nominally equal to n^2 times that of one metallic trace. With the availability of more than five metallic layers in modern CMOS technologies, stacked inductors can provide larger inductance values in smaller areas [69] and [81].

The most commonly used compact model of spiral inductor is the standard "9-element" model [32] and [121], as shown in Fig. 3.12. In this chapter, we present a more accurate equivalent circuit for two-layer spiral inductors, particularly suited to be used in the design of RFIC's. The contributions of the metallic traces and eddy current in the substrate to the total performance of the two-layer spiral inductor are modeled respectively by different parts in the circuit model. The proposed equivalent circuit is validated considering experimental data of a series of two-layer spiral inductors on silicon substrate, and the results are reported in Section 5.4.

5.2 Analysis of Eddy Current in the Substrate

Eddy current in the substrate arises from the magnetic *B*-field generated by the impressed current in the metallic trace of inductor that penetrates the silicon substrate. The schematic representation of the eddy current is shown in Fig. 5.1. The authors of [83] derived the 2-D equations of the eddy current at both low and high frequencies for the cases of single- and two-layer substrate. The directions of the eddy current depend on the *B*-field throughout the whole domain [2].

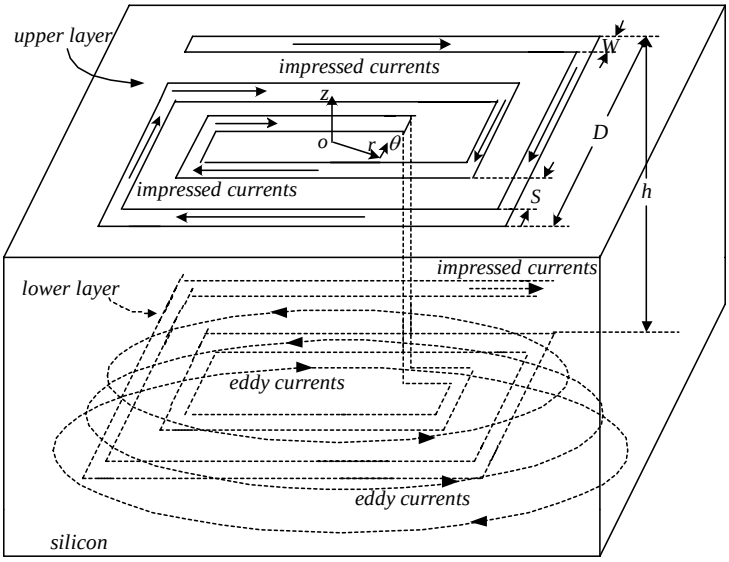

Fig. 5.1: Illustration of eddy current in the substrate of two-layer spiral inductors.

By considering the eddy current as the sum of all displacement current in the substrate, we can regard the substrate resistance loss and inductance as the results of the eddy current. In [42] and [49], some innovative circuit models of spiral inductor which incorporate the substrate losses were provided. The authors of [42] introduced a substrate resistor and a transformer in the model to describe the effect of eddy current, but the turn ratio of the transformer in their circuit is fixed to be $1:1$. Similarly, a new wide-band compact model for single-layer spiral (SLS) inductors on lossy silicon substrate was

presented in [66] and the innovation of their research was also based on the eddy current effects in the circuit modeling of spiral inductors.

For the case of a one-layer substrate, the self- and mutual impedance terms were derived in [83] as

$$Z_{ij} = -200\pi j\omega\left(\int_0^{\infty} e^{-cz_1}\sqrt{c^2-1}xc + \int_0^{\infty} e^{-cz_2}\sqrt{c^2-1}xc + \frac{1}{z_1^2} + \frac{1}{z_2^2}\right), \tag{5.1}$$

where

$$z_{1,2} = (2b \pm (x_i + x_j)\, j)(j-1)\frac{\sqrt{800\pi\sigma\omega}}{2}. \tag{5.2}$$

Here, x represents the distance between the two sets of N parallel current filaments and b represents the height of the oxide insulation above the conductive substrate.

In the calculations of the eddy current in the substrate, the induction-heat effects are temporarily neglected. When an EM field is incident upon the metallic trace of the inductor, it will induce eddy current (see in Fig. 5.1). A common way of treating the problem is to use the current vector potential ($\vec{\psi}$) in the finite-element (FE) formulation of quasisteady Maxwell's equations in [122] as

$$\vec{J} = \nabla \times \vec{\psi}. \tag{5.3}$$

Here, the eddy current density $\vec{J}$, induced in the metallic trace with a conductivity σ by the electrical field $\vec{E}$, is represented as $\vec{J} = \sigma\vec{E}$. The $\vec{E}$, caused by the change of magnetic field $\vec{B}$ with time, is given by equation (3.41).

By combining equations (5.3) and (3.41) and considering the effect of the induced current, we can obtain the governing equation for the metallic trace with permeability μ as

$$\nabla \times \frac{1}{\sigma} \nabla \times \vec{\psi} = -\frac{\partial}{\partial t}(\vec{B} + \mu \vec{\psi}). \tag{5.4}$$

Since the metallic trace is very thin, it is reasonable to assume that the eddy current is induced by the *z* component of the magnetic field and the current vector potential, respectively. Thus, equation (5.4) becomes

$$\frac{\partial^2 \vec{\psi}}{\partial x^2} + \frac{\partial^2 \vec{\psi}}{\partial y^2} = \sigma \frac{\partial}{\partial t}(\vec{B} + \mu \vec{\psi}). \tag{5.5}$$

This indicates that there are two terms to contribute to $\frac{\partial \vec{B}}{\partial t}$ as

$$\frac{\partial \vec{B}}{\partial t} = \frac{\partial \vec{B}}{\partial x} U + \frac{\partial \vec{B}_i}{\partial t}. \tag{5.6}$$

The first term is zero for static field (*U*=0), while the second term is zero for a direct current case.

Then, the magnetic field in the substrate generated by the one turn of current has B_r and B_z components that are given by [123] as

$$B_r = \frac{\mu I z \left[\frac{R_0^2 + r^2 + z^2}{(R_0 - r)^2 + z^2} \int_0^{\pi/2} \sqrt{1 - \frac{4 R_0 r \sin^2 \theta}{(R_0 + r)^2 + z^2}} d\theta - \int_0^{\pi/2} \frac{d\theta}{\sqrt{1 - \frac{4 R_0 r \sin^2 \theta}{(R_0 + r)^2 + z^2}}} \right]}{2\pi r \sqrt{(R_0 + r)^2 + z^2}}, \tag{5.7}$$

and

$$B_z = \frac{\mu I[\frac{R_0^2 - r^2 - z^2}{(R_0 - r)^2 + z^2}\int_0^{\pi/2}\sqrt{1 - \frac{4R_0 r\sin^2\theta}{(R_0 + r)^2 + z^2}}d\theta + \int_0^{\pi/2}\frac{d\theta}{\sqrt{1 - \frac{4R_0 r\sin^2\theta}{(R_0 + r)^2 + z^2}}}]}{2\pi r\sqrt{(R_0 + r)^2 + z^2}}, \quad (5.8)$$

where I is the current that flows in the spiral inductor and R_0 is the radius of the inductor.

The induced E-field responsible for the eddy current production, which follows Faraday's law, can be expressed as

$$\frac{1}{r}\frac{\partial(rE_\theta)}{\partial r} \approx -j\omega B_z. \quad (5.9)$$

So, the eddy current in the substrate below the inductor can be computed through

$$\left|J_{eddy}\right| = \omega\varepsilon_0\varepsilon_r E_\theta = \frac{1}{2}\varepsilon_0\varepsilon_r\omega^2\left(\sum_{n=1}^{N_1}(rB_z) + \sum_{n=1}^{N_2}(rB_z)\right), \quad (5.10)$$

where n is the number of turn. N_1 and N_2 represent the total numbers of turns of the inductors on the upper and the lower layers, respectively.

Furthermore, in the case of two-layer spiral inductors, B_z and E_θ will become much larger as the lower metallic trace is usually fabricated in the semi-conductor substrate entirely. So, it is reasonable that the eddy current within the silicon substrate of two-layer spiral inductor, induced by the current from the metallic traces, is more significant than that of the single layer case. Thus, one of the main purposes of our study is to improve the circuit model for two-layer spiral inductor and incorporate the effects of eddy current into our circuit modeling simultaneously.

Based on equations (5.7) to (5.10), we can conclude that both the magnetic field intensity and the induced eddy current in the substrate are usually proportional to the exciting current of the spiral inductor in both layers. As such, there exists a mutual coupling factor, which is denoted as *M* in Fig. 5.3, between the current flowing in the two-sandwiched metallic layers and the eddy current in the semi-conductor substrate.

5.3 The Equivalent Circuits for Two-layer Spiral Inductors

The layout of a typical two-layer spiral inductor is also shown in Fig. 5.1. This section describes the modifications in the circuit modeling of two-layer inductor and the circuit element representation in the equivalent circuit.

5.3.1 Conventional Modeling for Multi-layer Spiral Inductors

Based on the conventional hybrid π-mode circuit for normal single-layer spiral (SLS) inductors, one theoretical method to model the effects of the metallic traces on different layers in the circuit is shown in Fig. 5.2. C_s and C_s' represent respectively the total fringing-field capacitance between the two metallic traces in different layers, and between the sides of the trace in the lower layer only. Another fringing-field capacitance C_s'' in the upper layer is temporarily neglected in the circuit model for simplification. Each of the R_s and L_s represents the corresponding series resistance and inductance of one single metallic trace, respectively. *M* represents the coupling factor of mutual inductance between the two metallic traces in different layers. C_{ox} contributes to the

capacitance of the substrate of silicon oxide, and R_{si} and C_{si} model the effects of the silicon substrate below.

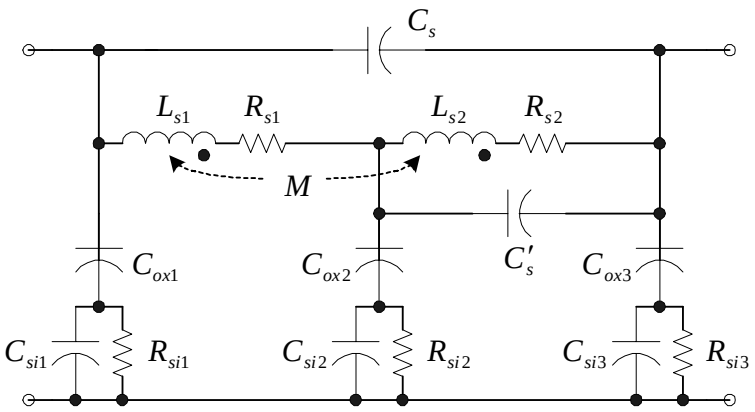

Fig. 5.2: One kind of conventional equivalent circuit for two-layer spiral inductors.

5.3.2 Modified Modeling with Eddy Current Effects

In the case of SLS, the equivalent circuit in Fig. 5.2 can usually be simplified as a *T*–mode model by concentrating the substrate effects into a single part at the center. While in the case of multi-layer spiral (MLS) inductor, each of those three parts for the substrate can no longer be easily neglected in the network, due to the model limitations. Such will enlarge the complexity in the evaluations of circuit components and characterizations.

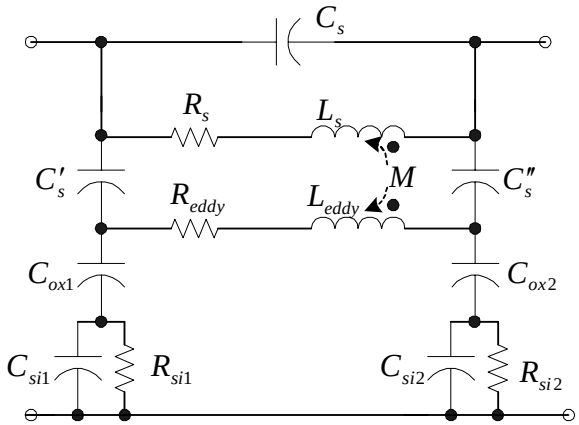

Fig. 5.3: Modified equivalent circuit for two-layer spiral inductors.

Then, by incorporating the effects of eddy current in the substrate, we can improve the model of two-layer spiral inductors as shown in Fig. 5.3. Here, R_{eddy} and L_{eddy} contribute to the substrate loss and the inductance effect caused by the eddy current, respectively. *M* represents the coupling factor of the eddy current from the impressed current. In contrast to the conventional model in Fig. 5.2, both of the metallic traces in the two layers are respectively modeled as a simple *R-L* series network in our proposed model.

5.3.3 Quality Factor Evaluation

Since our proposed model is a hybrid π network (similar as Fig. 2.18), the input impedance of the network can easily be derived from

$$Z_{in} = -\frac{1}{Y_{12}(\omega)} \approx R(\omega) + j\omega L(\omega), \tag{5.11}$$

in which *R* and *L* are the components for the series branch of the whole inductor. The validation and advantage of the modified model will be reported in Section 5.4.

The quality factor *Q* of a spiral inductor is given by the ratio of the inductive reactance to the total dissipation of a inductor. So, it can be directly achieved from [42] and [66] as

$$Q(\omega) = \frac{\mathrm{Im}(Z_{in})}{\mathrm{Re}(Z_{in})} = \mathrm{Im}(\frac{1}{Y_{11}(\omega)}) / \mathrm{Re}(\frac{1}{Y_{11}(\omega)}). \tag{5.12}$$

5.4 Experimental Results

In this section, we compare the simulated results generated from the two equivalent circuit models as mentioned previously with the measured data on several samples of two-layer spiral inductors. All the sample inductors are measured by the HP8510C vector network analyzer and the HP nonlinear network measurement system.

We designed several circular two-layer spiral inductors with different number of turns and different outer dimensions on silicon. For the silicon substrate, the thickness of the upper SiO_2 layer is $20\,\mu m$ and that of the lower silicon layer is $45\,\mu m$. Detailed geometric parameters of these inductors are listed in Table 5.1.

	$W(\mu m)$	$S(\mu m)$	N	$h(\mu m)$	Metal Thickness(μm)	Inner Radius(μm)
Inductor 36	10	1.5	2.25	10	1.57	30
Inductor 37	10	1.5	3.25	10	1.57	30
Inductor 38	10	1.5	4.25	10	1.57	30
Inductor 39	10	1.5	5.25	10	1.57	30
Inductor 40	10	1.5	6.25	10	1.57	30

Table 5.1: Geometric parameters for two-layer spiral inductors.

5.4.1 Comparisons of the Simulation Results on Two Different Models

Fig. 5.4 illustrates the simulation results of S_{11} and S_{12} with the conventional model in Fig. 5.2 and the improved model in Fig. 5.3, for Inductor 36. A good agreement can be achieved between the simulated and the measured data. However, by plotting the difference between the simulated results and the measured data of S_{11} and S_{12} directly, the advantages of the improved model can be displayed more obvious (see in Fig. 5.5). And the two sets of simulated results are compared with the same set of measured data.

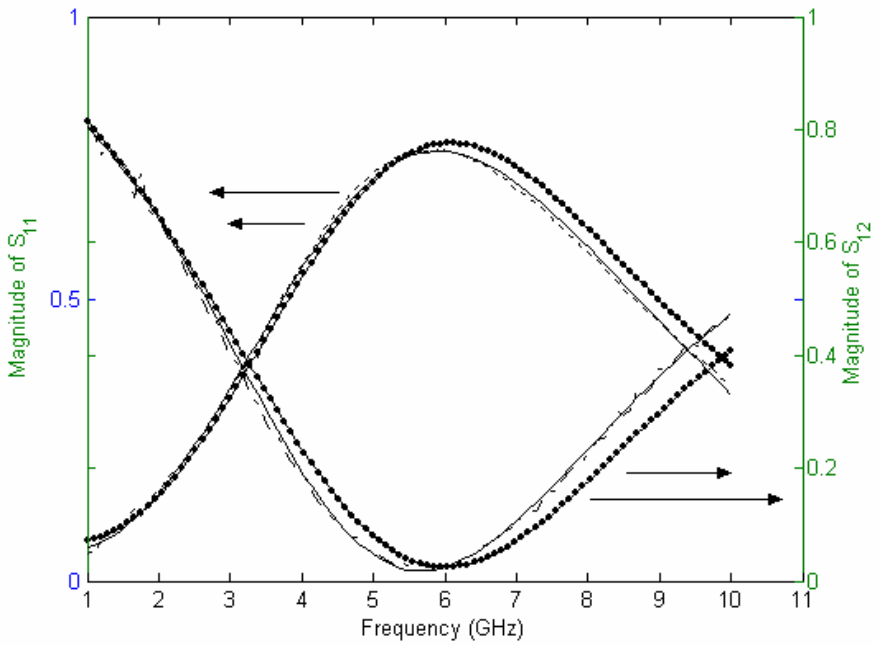

Fig. 5.4: Illustrations of comparisons of the *S*-parameters between the measured data (solid line) and the simulated data on the conventional model (point line) and the modified model (dashed line).

	R_s (Ω)	R_{eddy} (Ω)	L_s (nH)	L_{eddy} (nH)	C_s (fF)	C_s' (fF)	C_s'' (fF)	C_{ox1} (fF)	C_{ox2} (fF)	C_{si1} (fF)	C_{si2} (fF)	R_{si1} (Ω)	R_{si2} (Ω)	M
Inductor 36	10	13	3.6	0.6	0.04	399.4	820.2	17157	822.8	51.5	2.83	407.3	178.1	0.6
Inductor 38	9	7	6	1	28	734.5	2167	3993	87.63	7.5	20.3	176.4	0.3	0.8
Inductor 39	17.9	8.4	11	0.9	0.6	702.7	1367	93.9	34380	0.7	112.2	139.3	169.4	0.8

Table 5.2: Extracted lumped-elements in the improved circuit model.

By comparing with the same set of experimental conditions and with measurement errors of about 2%, it is apparent from Fig. 5.5 that our modified equivalent circuit can provide better *S*-parameter fitting results, especially in the high frequency range, i.e., higher than the inductor self-resonance frequency. In Fig. 5.5, the magnitude differences of S_{11} and S_{12} simulations are calculation from $\left|S_{11}^{measured}\right| - \left|S_{11}^{simulated}\right|$ and $\left|S_{12}^{measured}\right| - \left|S_{12}^{simulated}\right|$, respectively. Similar advantages of the improved circuit can also be achieved by comparing the simulation results of phases for the *S*-parameters.

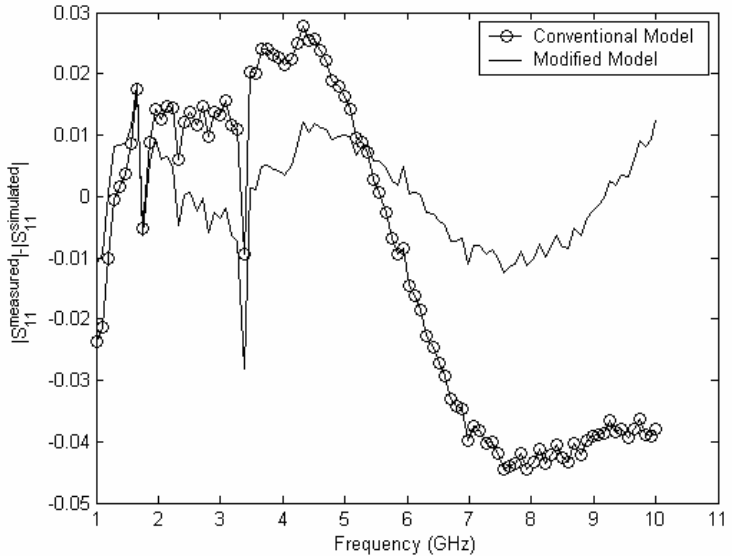

(*a*)

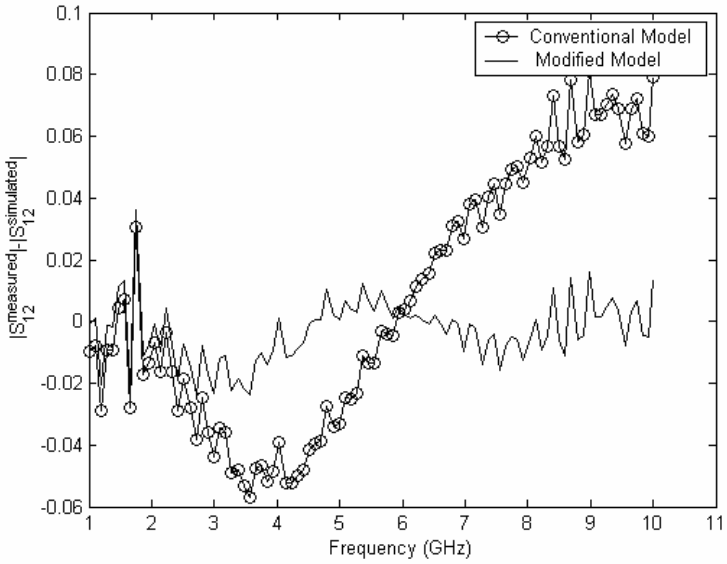

(*b*)

Fig. 5.5: Comparisons of the simulations results for the *S*-parameters with different models.

5.4.2 Further Discussion on the Validation of the Improved Circuit Model

A de-embedding procedure is performed firstly to extract all the lumped-elements of the proposed equivalent circuit model for the sample two-layer inductors through circuit optimization. The results of circuit components are reported in Table 5.2.

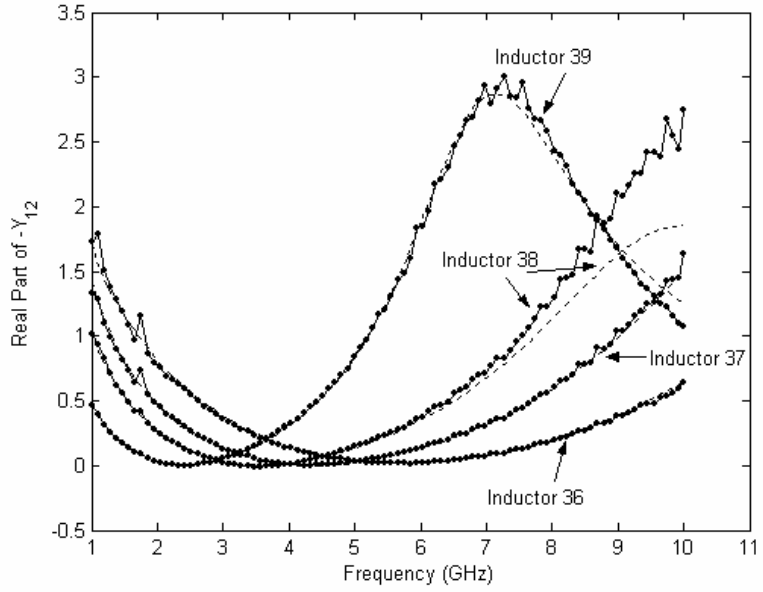

(*a*)

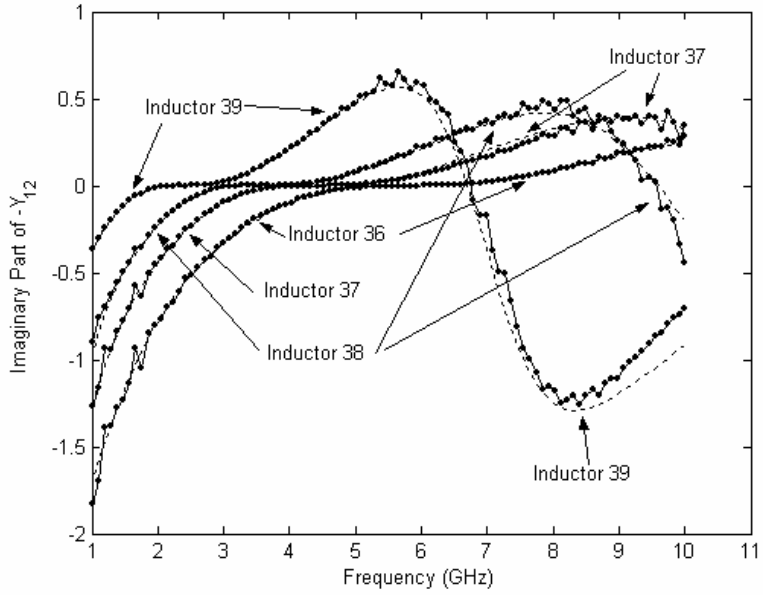

(*b*)

Fig. 5.6: Comparisons of the real and imaginary parts of $-Y_{12}$ between the measured data (point line) and simulated data (dashed line) with the improved model on different inductors.

Fig. 5.6 describes the real and imaginary parts of $-Y_{12}$ of some two-layer spiral inductors in equation (5.11). An excellent agreement between the simulated and the measured results is obtained.

Improved Model														
R_s	R_{eddy}	L_s	L_{eddy}	C_s	C_s'	C_s''	C_{ox1}	C_{ox2}	C_{si1}	C_{si2}	R_{si1}	R_{si2}	M
(Ω)	(Ω)	(nH)	(nH)	(fF)	(fF)	(fF)	(fF)	(fF)	(fF)	(fF)	(Ω)	(Ω)	
10	13	3.6	0.6	0.04	399.4	820.2	17157	822.8	51.5	2.8	407.3	178.1	0.6

Conventional Model															
R_{s1}	R_{s2}	L_{s1}	L_{s2}	C_s	C_s'	C_{ox1}	C_{ox2}	C_{ox3}	C_{si1}	C_{si2}	C_{si3}	R_{si1}	R_{si2}	R_{si3}	M
(Ω)	(Ω)	(nH)	(nH)	(fF)	(fF)	(fF)	(fF)	(fF)	(fF)	(fF)	(fF)	(Ω)	(Ω)	(Ω)	
1	9	1.0	1.3	52.6	509.0	10	755.0	199.8	3.1	21.3	403.0	98.8	240.9	813	0.7

Table 5.3: Illustrations of the comparison results of the extracted lumped-elements in both the conventional and improved models for Inductor 36.

Table 5.2 presents the extracted value of circuit components in the improved lumped-element circuit model (as shown in Fig. 5.3) for the samples inductors. Table 5.3 illustrates the comparison results of the circuit components' values of both the conventional and the improved circuit models for Inductor 36.

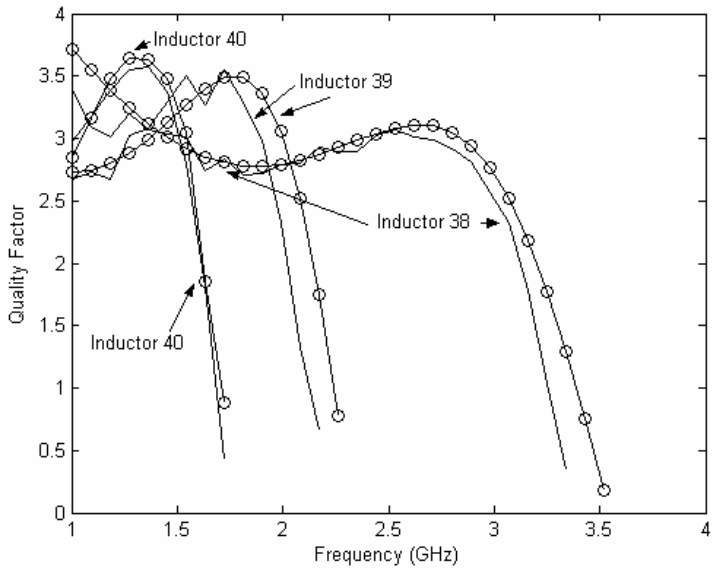

Fig. 5.7: Illustration of the measured (solid line) and simulated (circular mark) quality factors of different two-layer spiral inductors.

A good agreement between the extracted and the simulated values of quality factor with our improved circuit model is achieved on different sample inductors, as shown in

Fig. 5.7. These plots show that the improved model, which takes into account the physical phenomenon underlying the eddy current in the silicon substrate, is very satisfactory especially in the range below resonance frequency.

5.5 Conclusion

The effects of eddy current in the substrate of multi-layer spiral inductor are assumed to be more significant than those of single-layer case. Both the magnetic fields and the induced eddy current in the substrate are proportional to the excitation current in the metallic traces of a multi-layer spiral inductor.

An improved equivalent circuit model for two-layer spiral inductor on silicon substrate is presented. This model, which is characterized by detailed analysis of the effects of eddy current in the CMOS substrate, can describe accurately the scattering parameters, series resistance, inductance, and quality factor of two-layer spiral inductor. Compared with the conventional model, our proposed model provides a better agreement between the simulated and the measured responses of two-layer spiral inductor.

CHAPTER 6

DESIGNS AND APPLICATIONS

6.1 Introduction

In this chapter, we present some designs and applications, including a type of triple-band slot antenna with spiral EBG feedline, a modified CPW Wilkinson power divider fabricated with EBG-fed, and another power divider based on the transformer design.

6.2 Triple-Band Slot Antenna with Spiral EBG

The use of photonics materials has been driving the relative theory to the propagation of optical waves [124]. The theory of photonic band-gap (PBG) or electromagnetic band-gap (EBG) was developed initially for optical frequencies and can easily be applied to millimeters waves, microwaves, and antennas [124]. Generally, EBG can diminish the propagation constant causing the wave to move slowly [125]. Then in this section, we utilize the spiral EBG into the antenna design and attempt to achieve better antenna performances.

To implement our analysis, a triple-band rectangular-ring slot antenna with spiral EBG feed was designed, fabricated and tested. For comparison purpose, a reference antenna was also fabricated and tested [126]. The slot antenna consists of three concentric rectangular-ring slots and is printed on a substrate of thickness H=1.6mm and relative permittivity $\varepsilon_r = 4.4$.

The geometric parameters of the EBG feedline are given in Fig. 6.1 and Table 6.1 gives the geometric parameters of two antennas. For the convenience of comparison, all the geometric parameters, except feedline, are the same for EBG-fed antenna and reference antenna. The fabricated reference antenna and EBG antenna are shown in Fig. 6.2 and Fig. 6.3, respectively.

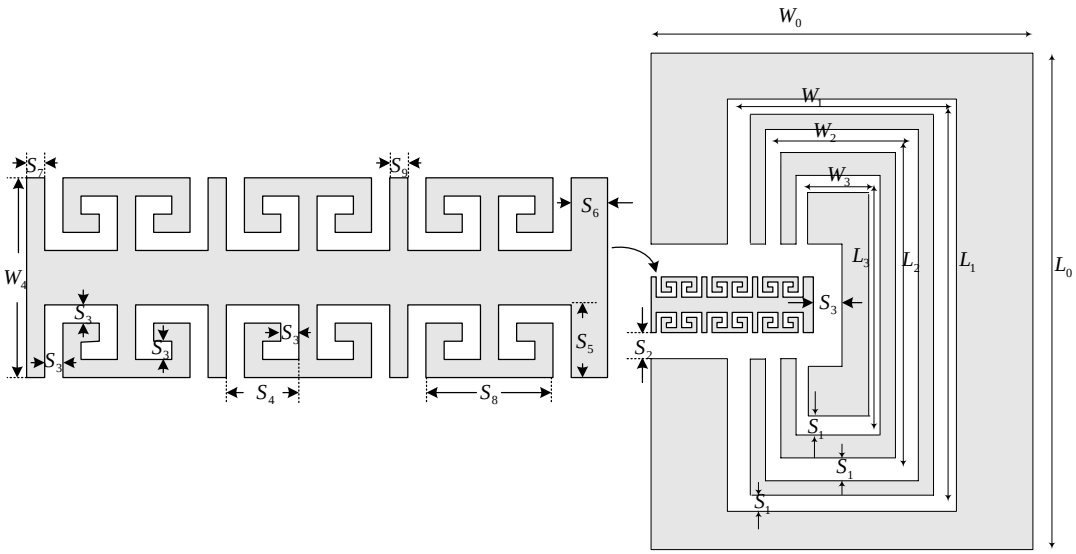

Fig. 6.1: Geometric dimensions of multi-band slot antenna with EBG feed.

L_0	L_1	L_2	L_3	W_0	W_1	W_2	W_3	W_4	S_1	S_2	S_3	S_4	S_5	S_6	S_7	S_8	S_9
65	35	30	24.5	53	20	15	10	6.4	2	0.3	0.5	1.2	1.5	1.4	0.6	5.6	2.5

Table 6.1: Geometric parameters (in mm) for reference antenna and EBG-fed antenna.

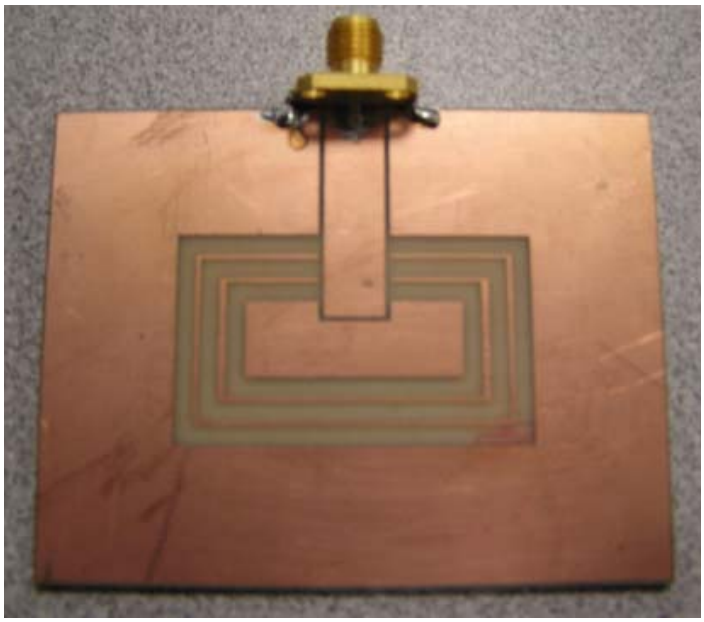

Fig. 6.2: Fabricated slot line antenna with conventional CPW feed.

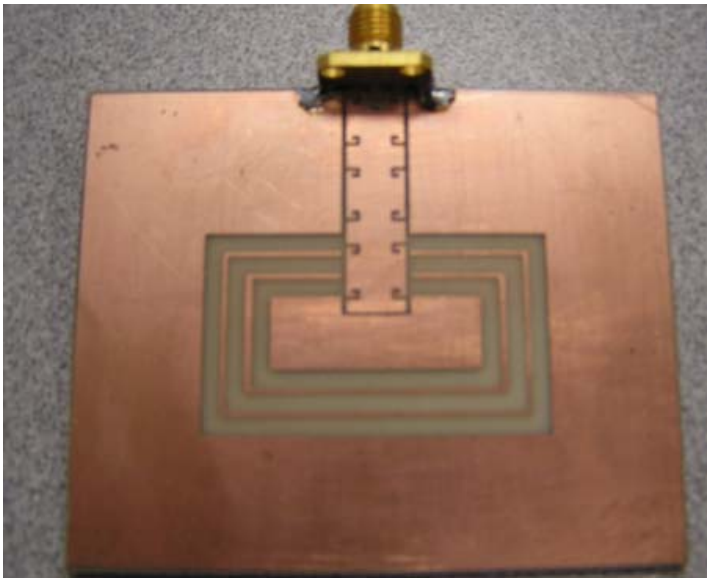

Fig. 6.3: Fabricated slot line antenna with spiral EBG feed.

	f_1(GHz)	BW_1	$Gain_1$(dBi)	f_2(GHz)	BW_2	$Gain_2$(dBi)	f_3(GHz)	BW_3	$Gain_3$(dBi)
CPW-fed	1.93	7.3%	3.53	2.34	4.4%	4.59	3.2	22.7%	4.42
EBG-fed	1.92	11.5%	3.68	2.4	13.9%	4.51	3.22	24.1%	5.02

Table 6.2: Comparison of measured performance between reference antenna and EBG antenna.

Figs. 6.4 to 6.7 show the measured and simulated return losses of the reference antenna and EBG-fed slot antenna. As noted from these figures and Table 6.2, the EBG feedline effectively increases the impedance bandwidth for all the resonance frequencies of the antenna.

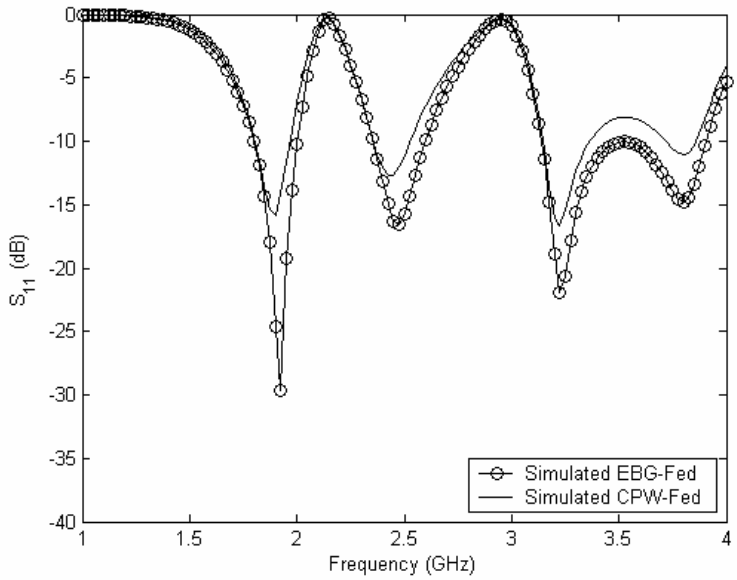

Fig. 6.4: Simulated return loss of EBG-fed slot antenna and reference antenna.

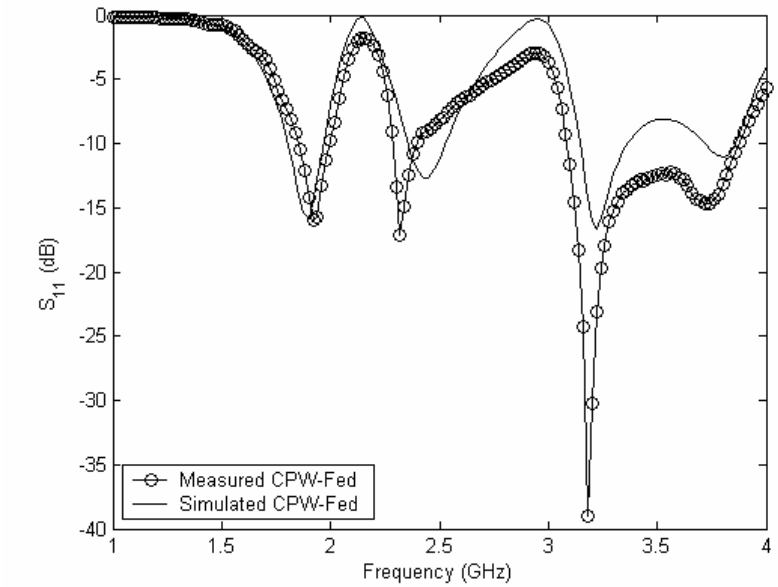

Fig. 6.5: Simulated and measured return loss of reference antenna.

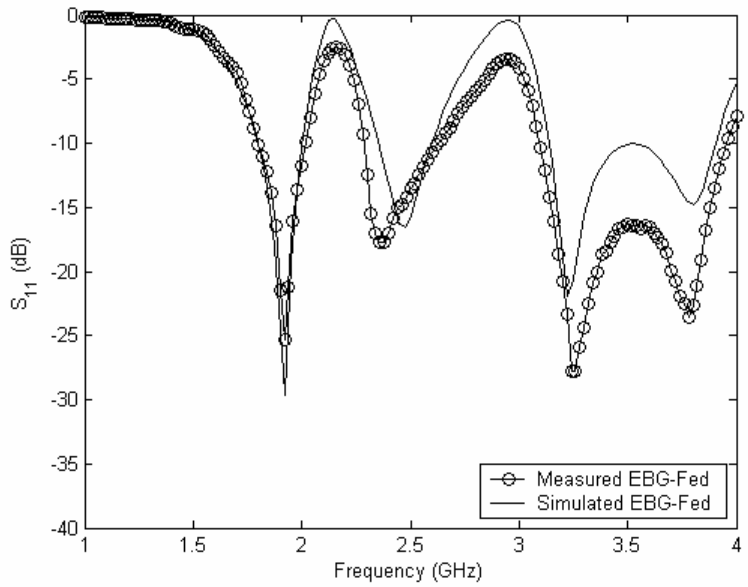

Fig. 6.6: Simulated and measured return loss of EBG-fed slot antenna.

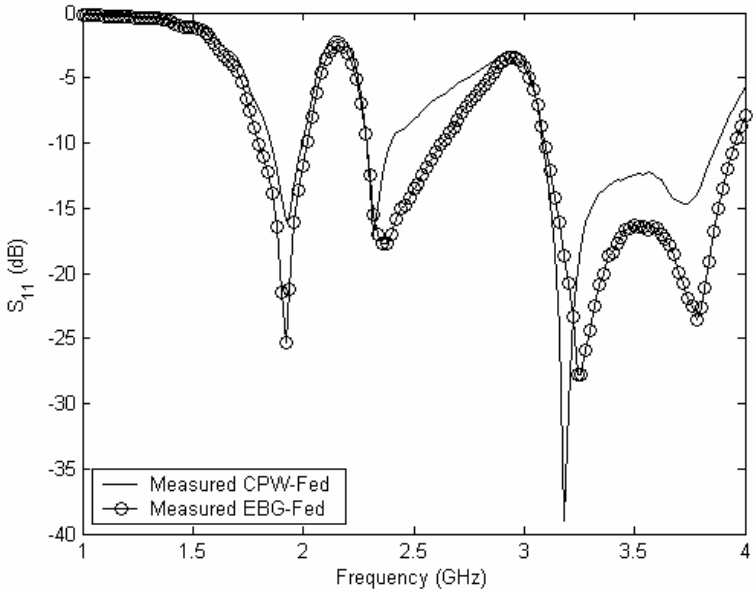

Fig. 6.7: Measured return loss of EBG-fed slot antenna and reference antenna.

Figs. 6.8 to 6.13 present the measured *E*-plane and *H*-plane radiation patterns of the EBG-fed slot antenna. From these figures, the three operation frequencies of the EBG-fed antenna have the same polarization. Compared with the results of the reference antenna

shown in [126], the radiation patterns of the modified antenna are not changed significantly. The gains of the EBG-fed and CPW-fed antennas in the broadside direction are also measured. The measurement results are tabulated in Table 6.2.

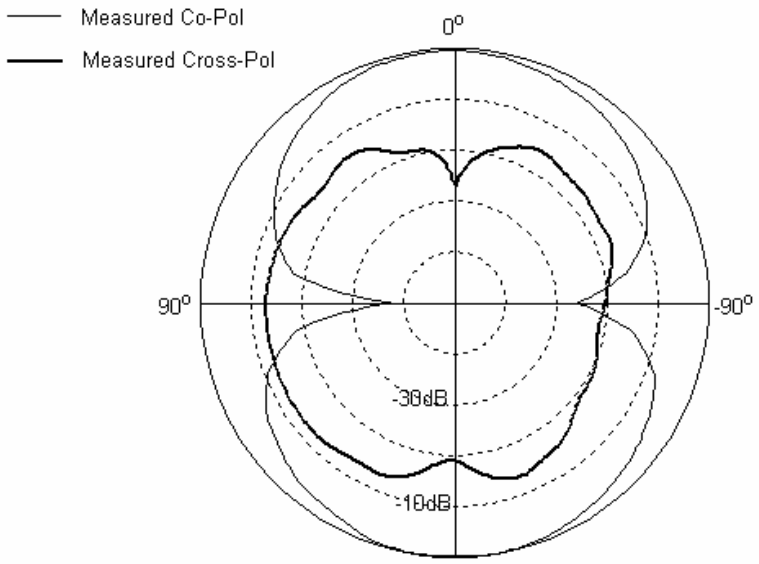

Fig. 6.8: *E*-plane of EBG-fed antenna at 1.92GHz.

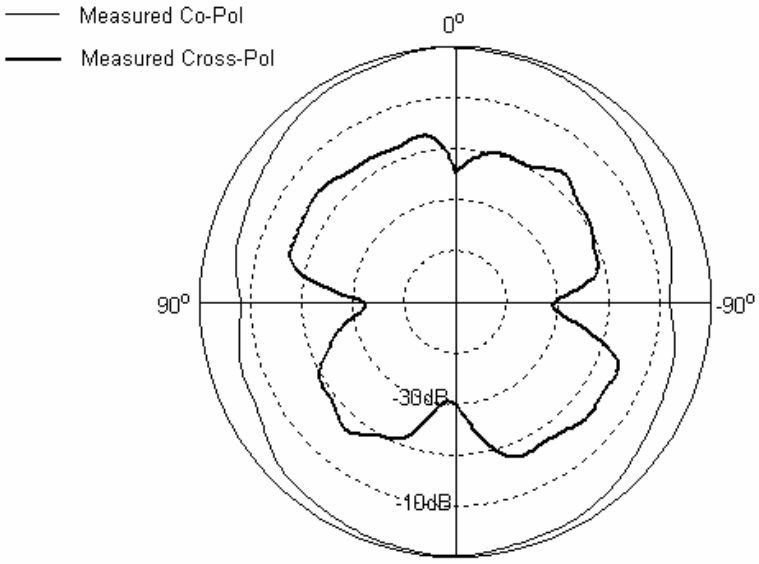

Fig. 6.9: *H*-plane of EBG-fed antenna at 1.92GHz.

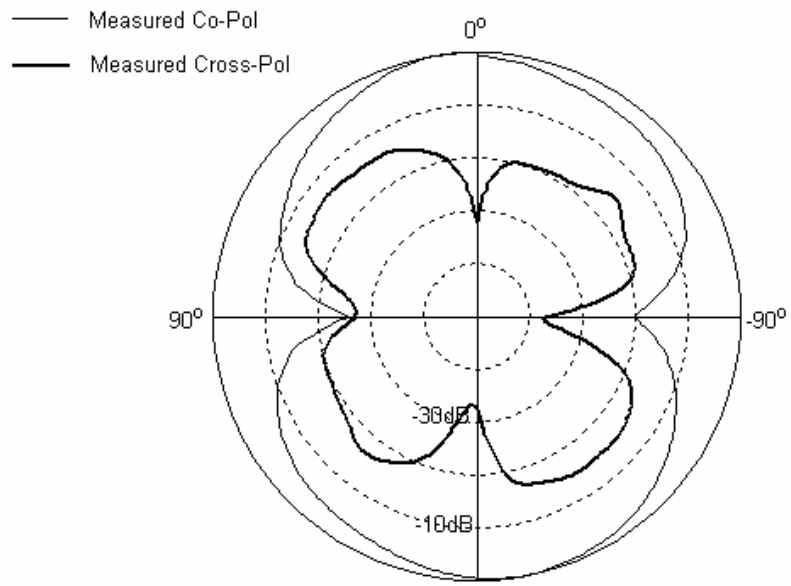

Fig. 6.10: *E*-plane of EBG-fed antenna at 2.4GHz.

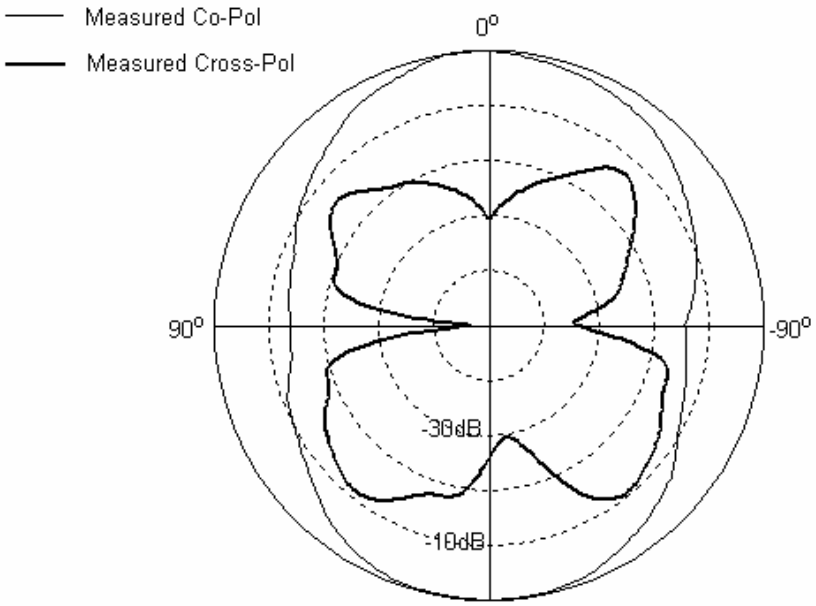

Fig. 6.11: *H*-plane of EBG-fed antenna at 2.4GHz.

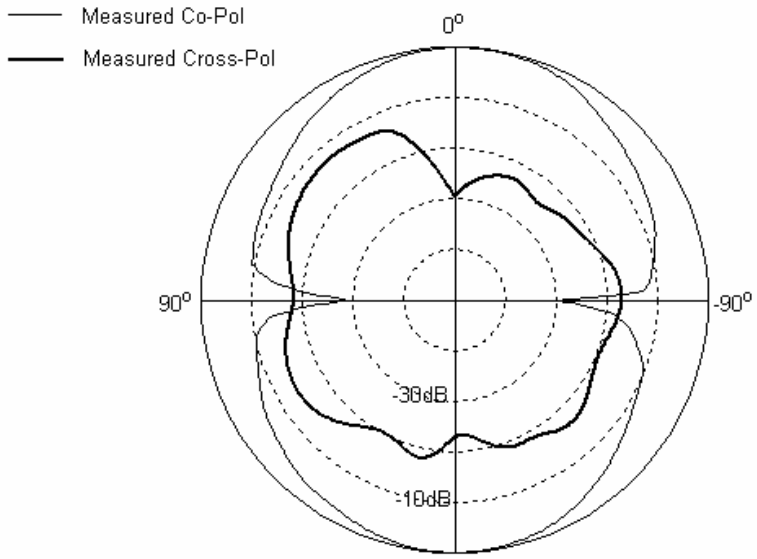

Fig. 6.12: *E*-plane of EBG-fed antenna at 3.22GHz.

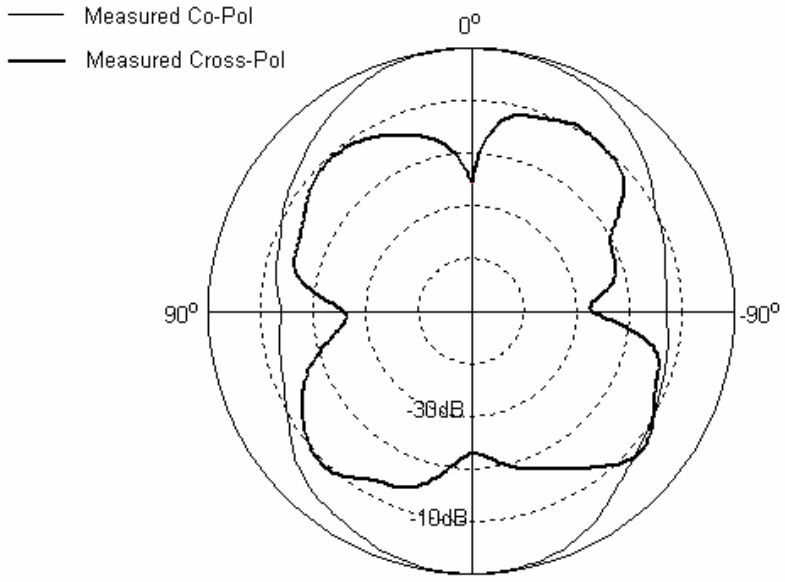

Fig. 6.13: *H*-plane of EBG-fed antenna at 3.22GHz.

6.3 Modified Wilkinson Power Divider with EBG

6.3.1 Introduction

The Wilkinson power divider and combiner have been widely used for microwave power amplifiers [93], and [127]-[128]. They have same structure, which consists of two $\lambda/4$ branches of transmission line and a termination resistor, where λ is the wavelength of the transmission line.

Fig. 6.14 shows the basic structure of a Wilkinson power divider [93], and [129]-[130]. The two transmission lines and the termination resistor *R* match all input and output ports simultaneously and provide a good isolation between the input ports of the power combiner and between the output ports of the power divider. Also, they can handle arbitrary power levels from input to output ports. If the harmonics are suppressed in the power divider or combiner structure, we can eliminate separate harmonic rejection filters from the circuit and design an area-effective power amplifier (as reported in [128]).

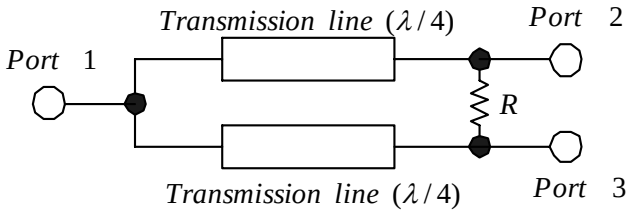

Fig. 6.14: Equivalent circuit of the Wilkinson power divider.

6.3.2 Experimental Results

In this section, we will present a type of modified EBG CPW Wilkinson power divider. The device is fabricated on a substrate of thickness *H*=62mil and relative permittivity $\varepsilon_r = 10$. The width of each EBG is 0.1mm. The circuit configuration of the proposed power divider is shown in Figs. 6.15 to 6.16 and Table 6.3. Due to the existence of the

spiral EBG, the termination resistor *R* between two outputs is re-optimized to be 82Ω with ADS. Two air bridges are added at the circuit discontinuities to prevent the coupled slotline mode from propagating on the CPW lines. Fig. 6.17 plots the computed return loss of two different power dividers of the same geometric parameters and termination resistance, but with and without EBG respectively. The simulated results show that the modified power divider with EBG near port 1 can provide relatively larger bandwidth (124.5%) of the input than the one without EBG (115%).

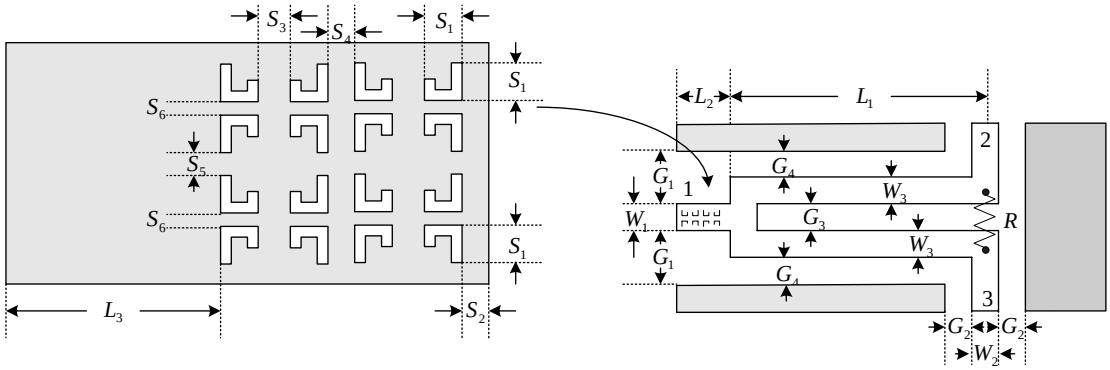

Fig. 6.15: Structure of power divider with EBG.

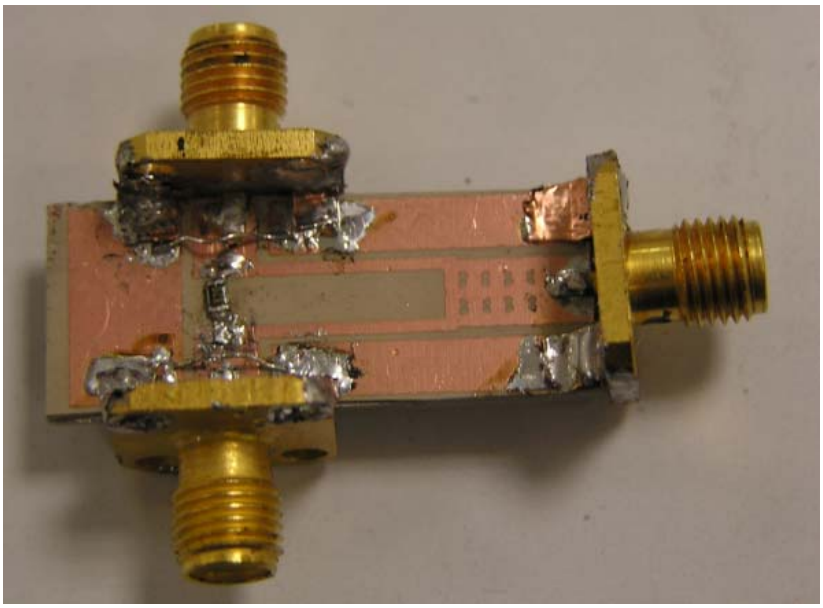

Fig. 6.16: Fabricated modified Wilkinson power divider with EBG.

L_1	L_2	L_3	W_1	W_2	W_3	G_1	G_2	G_3	G_4	S_1	S_2	S_3	S_4	S_5	S_6
13.5	7.8	3.5	4.2	3.6	0.9	0.5	0.7	2.8	0.3	0.3	0.1	1.0	1.0	0.8	0.2

Table 6.3: Geometric parameters (in mm) for the modified Wilkinson power divider with EBG.

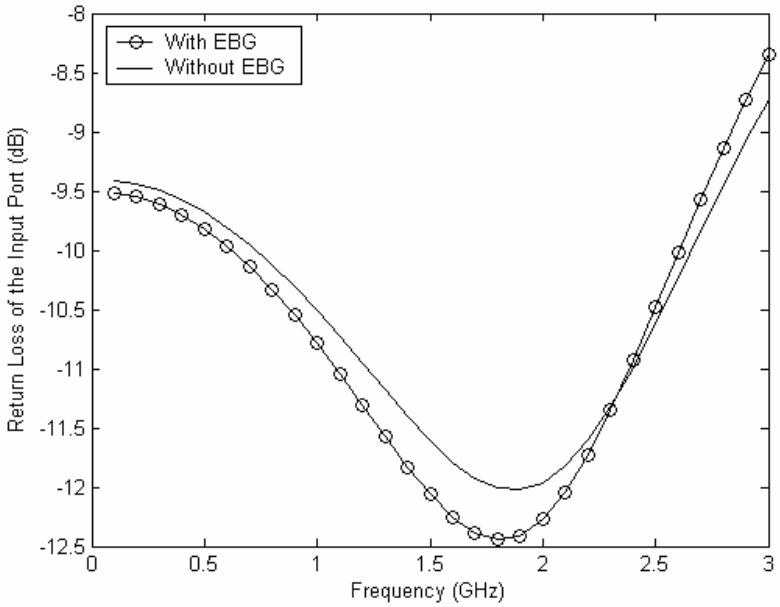

Fig. 6.17: Simulated return loss of the input port of power dividers with EBG and without EBG.

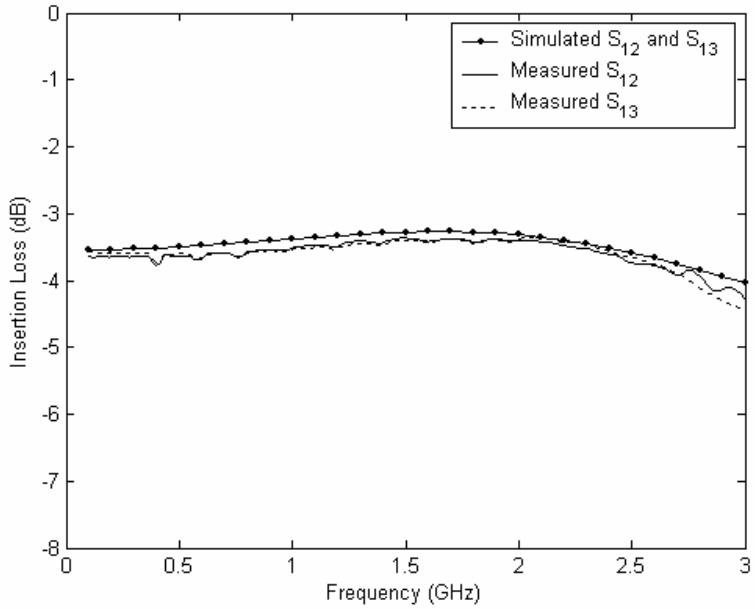

Fig. 6.18: Insertion loss of the power divider with EBG.

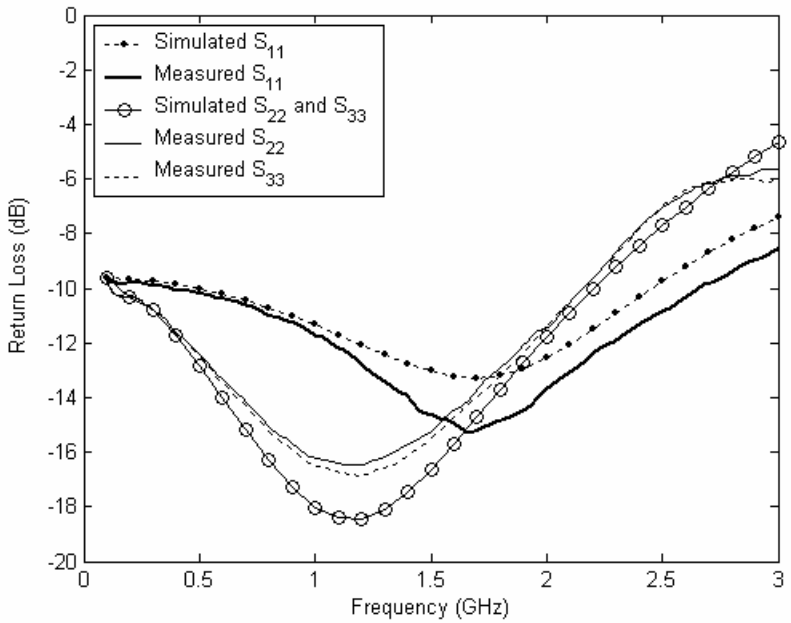

Fig. 6.19: Return loss of the power divider with EBG.

Then, our modified power divider is fabricated and tested from 0.1-3GHz with VNA. Figs. 6.18 and 6.19 provide the measured and simulated insertion and return losses of our divider. Here, the results include two 2-mm-long CPW lines for the outputs. The measured insertion loss is better than -3.5dB from 1.2GHz to 2.2GHz and the bandwidth is 58.8% centered at 1.7GHz. The measured return losses are less than -10dB from 0.4GHz to 2.6GHz for the input port and from 0.2GHz to 2.15GHz for the two output ports.

6.4 Two-Layered LTCC Transformer Design Based on the Balun Network

Transformers have been used in radio frequency (RF) circuits since the early days of telegraph. The operation of a passive transformer is based on the mutual inductance

between two or more conductors, or windings (spiral inductors). The transformer is designed to couple alternating current from one winding to the other without a significant loss of power, and impedance levels between the windings are also transformed in the process (i.e., the ratio of terminal voltage to current flow changes between windings). In addition, direct current flow is blocked by the transformer, allowing the windings to be biased at different potentials [84].

The balun is a special type of transformer, which couples a balanced circuit to an unbalance one. The well-known Marchand balun [85] is a microwave balun and is important in realizing balanced mixers [86]-[87], amplifiers, and phase shifters [88]-[90] by providing differential signals. Coupled lines are useful and widely applied structures that provide the basis for many types of balun [91].

In this study, several spiral metallic traces with different number of turns as spiral inductors were introduced in our transformer fabrications. We propose a very simple method for achieving a new type of transformer, which is based on the balun network design and able to provide one pair of non-differential signals. This makes it easy to use our new type of transformer as microwave power divider/combiner. In the design of this application, we utilized coupled spiral metallic lines instead of the conventional transmission lines in the Wilkinson power divider to reduce the total area needed for the device.

6.4.1 General Review of Monolithic Transformer

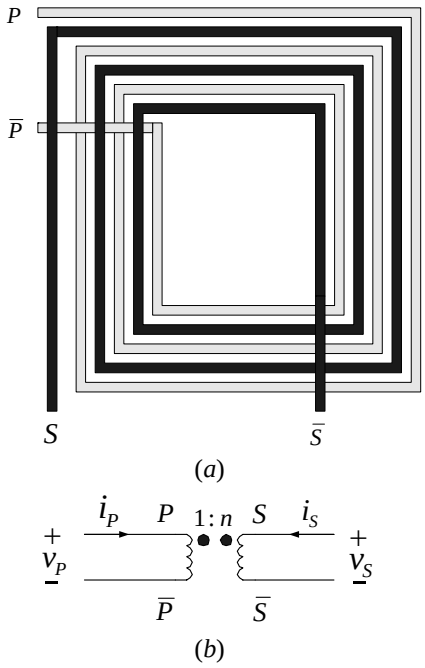

Fig. 6.20: Monolithic transformer. (*a*) Physical layout. (*b*) Circuit model.

A microstrip line is the simplest on-chip element for monolithic implementation of a transmission line inductor, and the strip is normally wound into a spiral to reduce the chip area. Interwinding microstrip spiral inductors to magnetically couple independent conductors is a logical extension of this concept, and results in the monolithic transformer, as shown in Fig. 6.20.

An early example of this type of structure is the compact spiral directional coupler reported by Shibata in 1981 [131]. This was followed by a circuit demonstration of monolithic transformer in a push-pull amplifier, and later, transmitter and image-reject mixer circuits fabricated in GaAs IC technology by Podell [132]-[133]. The first analysis of monolithic transformers was published by Frlan [134], who compared the simulation data and the experimental measurements for a monolithic spiral transformer. Boulouard and Le Rouzic [135] proposed an alternate topology and analysis technique for MMIC

spiral transformer, which was also verified experimentally. Frlan and Rabjohn [136] demonstrated square spiral transformers on alumina and GaAs substrate, and developed circuit simulation tools based upon extraction of a lumped element model for the transformer from physical and geometric parameters. This modeling technique was later extended to the analysis of planar structures on conductive substrates, such as silicon [32] and [61]. In the recent literature, there are many examples of transformers fabricated in silicon IC technology for use in RF circuits, such as preamplifiers [137]-[138], oscillators [139]-[140], mixer [64], and [141]-[142], and power amplifiers [143].

A planar monolithic transformer constructed from interwound metal conductors is shown in Fig. 6.20. Magnetic flux produced by current i_P flowing into the primary winding at terminal *P* induces a current in the secondary winding that flows out of terminal *S*. This produces a positive voltage v_S across a load connected between terminals *S* and $\overline{S}$. The main electrical parameters of interest to a circuit designer are the transformer turns ratio *n* and the coefficient of magnetic coupling k_m. The current and voltage transformations between windings in an ideal transformer are related to the turns ratio by the following equation

$$n = \frac{v_S}{v_P} = \frac{i_P}{i_S} = \sqrt{\frac{L_S}{L_P}} \tag{6.1}$$

where the primary and secondary voltages (v_P, v_S) and currents (i_P, i_S) are defined in Fig. 6.20 (*b*), and L_P, L_S are the self-inductances of the primary and secondary windings, respectively. The strength of the magnetic coupling between windings is indicated by the *k*-factor, as

$$k_m = \frac{M}{\sqrt{L_P L_S}} \tag{6.2}$$

where M is the mutual inductance between the primary and secondary windings. The self-inductance of a given winding is the inductance measured at the transformer terminals with all other windings open-circuited. If the magnetic coupling between winding is perfect (i.e., no leakage of the magnetic flux), k_m is unity, while uncoupled coils have a k-factor of zero. A practical transformer will have a k-factor somewhere between these two extremes. Since the materials used in the fabrication of an IC chip have magnetic properties similar to air, there is poor confinement of the magnetic flux in a monolithic transformer and $M < \sqrt{L_P L_S}$. Thus, the k-factor is always substantially less than one for a monolithic transformer, however, coupling coefficients as high as 0.9 are realizable on-chip [84].

The phase of the voltage induced at the secondary of the transformer depends on the choice of the reference terminal. For an *ac* signal source with the output and ground applied between terminals P and $\overline{P}$, there is a minimal phase shift of the signal at the secondary if the load is connected to terminal S (with $\overline{S}$ grounded). This is the non-inverting connection. In the inverting connection, terminal S is grounded and $\overline{S}$ is connected to the load so that the secondary output is antiphase to the signal applied to the primary. Aside from the phase shift between input and output ports, other aspects of the transformer's electrical behavior depend on the choice of terminal configuration.

6.4.2 Multifilament Transformer and Baluns

The $1:n$ transformers described in the previous section consist of two independent windings (or conducting filaments) and are classified as bifilar transformers. Multifilament transformers can also be constructed on-chip. These devices can be used to implement power dividers, combiners, and baluns [84].

A balun is a device which couples a balanced circuit to an unbalanced one. There are many structures used to implement baluns at RF and microwave frequencies, although a differential amplifier is the most commonly used method for unbalanced-to-balanced signal conversion on-chip. Microwave balun structures such as the Lange, rat-race and branch line coupler require physical dimensions on the order of the signal wavelength and so these devices consume too much chip area when operating below approximately 15GHz [144]. The transformers shown in Fig. 6.20 (*a*) can also implement a balun by grounding one of the windings at the electrical center, or canter tap.

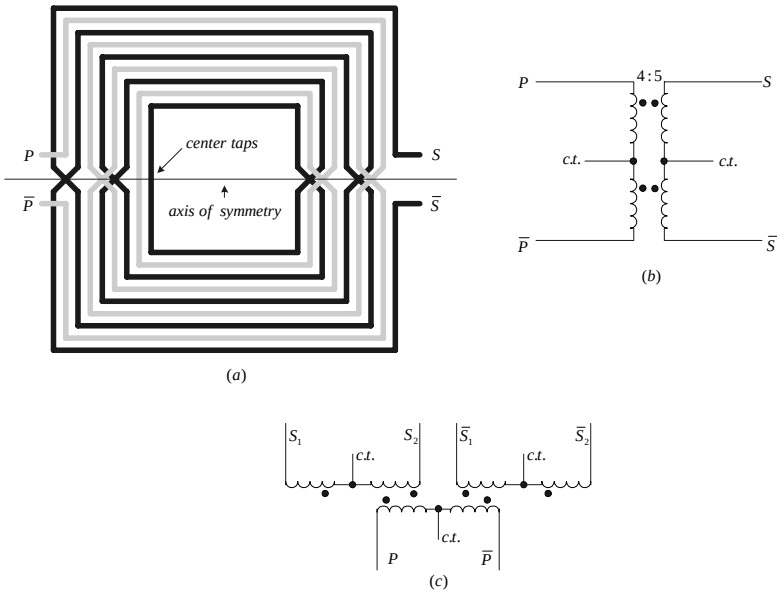

Fig. 6.21: (*a*) Square bifilar balun layout. Schematic symbols of bifilar (*b*) and trifilar (*c*) balun.

The electric and magnetic center (EMC) and physical center of a winding differ for all of the spiral designs shown in Fig. 6.21 (*a*), which is a disadvantage of asymmetrical layouts. While a square symmetrical layout, first proposed by Rabjohn [136] and illustrated in Fig. 6.21 (*a*), solves this problem. This transformer consists of two groups of interwound microstrip lines that are divided along a line of symmetry running horizontally, as shown in Fig. 6.21 (*a*). The groups of lines are interconnected in a way which brings all four terminals to the outside edge of the transformer layout, which is an advantage when connecting the transformer terminals to other circuitry. Also, the midpoint between the terminals on each winding, or the center tap, can be located precisely in the symmetrical layout as indicated in Fig. 6.21 (*a*). The turns' ratio for the example shown is $4:5$ between the primary and secondary windings. The schematic symbols of bifilar and trifilar baluns are also maintained in Figs. 6.2 (*b*) and 6.2 (*c*), respectively. For the case of a trifilar balun, the device consists of one primary and two secondary windings as shown in Fig. 6.21 (*c*).

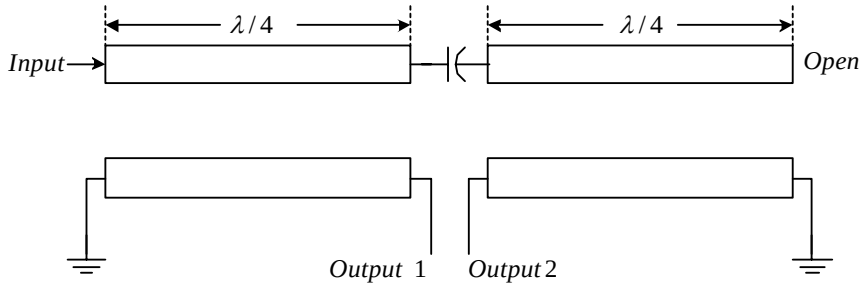

Fig. 6.22: Transmission line model for the Marchand balun.

The well-known Marchand balun [85] is most commonly used to provide balanced outputs from an unbalanced input. In the conventional Marchand balun, two conductors having equal potential with 180° phase difference constitute the balanced line. So the power going into the unbalanced input is split into outputs that are half power each and

180° out of phase with each other. A transmission line version of the Marchand balun is shown in Fig. 6.22. The Marchand balun has a better bandwidth and more balanced outputs than the coupled line baluns because the smaller differences between the even and odd mode impedances compared with what is needed for the coupled line balun case. As seen in Fig. 6.22, the Marchand balun consists of two sets of coupled lines with each being $\lambda/4$ long at the center frequency of operation. The principle of operation of the Marchand balun is very well explained in literature [85] and [145]. Usually these coupled lines are side coupled, but in recent times it has been moving towards broadside coupled lines (top and bottom). Broadside coupling, which provides a better coupling factor, is able to achieve a tighter coupling than side by side coupling and will be introduced into our new transformer design in the sections below.

6.4.3 Design and Fabrication

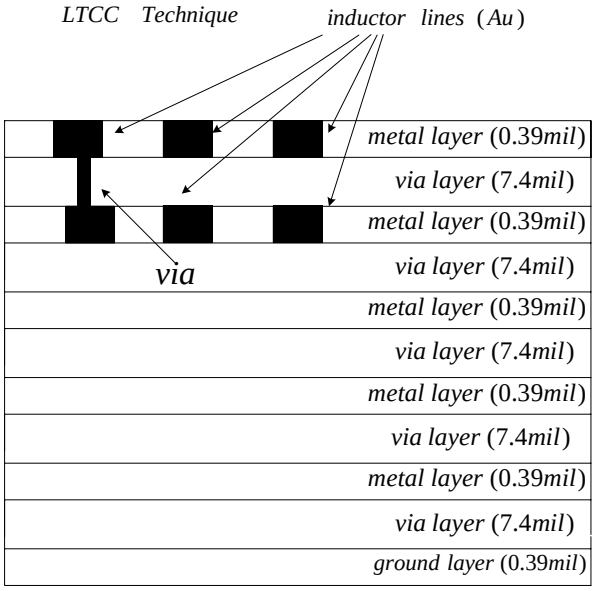

Fig. 6.23: The cross section view of the multi-layer transformer.

Fig. 6.23 shows the multilayer structure used to realize our proposed low temperature co-fired ceramic (LTCC) transformer network. The Ferro-A6 M LTCC tape is adopted and the dielectric constant for each layer is 5.9. Gold metal is used for the spiral traces. The cross section view of the proposed transformer network is illustrated in Fig. 6.23.

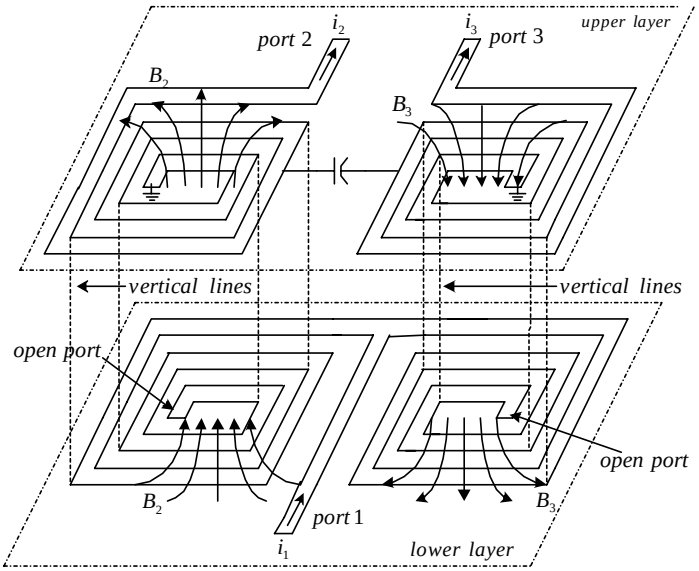

Fig. 6.24: Two-layer transformer structure with spiral inductors.

As illustrated in Fig. 6.24, due to the symmetrical structure of the two spiral traces on the lower layer, the input current i_1 generates a pair of differential magnetic field, B_2 and B_3. These differential magnetic fields will in turn induce a pair of non-differential current signals, i_2 and i_3 in ports 2 and 3 respectively on the upper layer. Due to the symmetrical but opposite spiral directions of the two spiral traces on the upper layer, the induced currents will flow in the direction indicated in Fig. 6.24.

All the spiral traces in one transformer will have the same outer dimensions, metal width, spacing, and number of turns. The spiral traces on the two layers are not entirely overlapped, in order to reduce the coupling capacitance loss between the upper and lower

layers (see the dotted “vertical lines” in Fig. 6.24). In addition, to achieve better balanced outputs, a capacitor is inserted between the two spiral traces on the upper layer.

6.4.4 Transformer Characterization

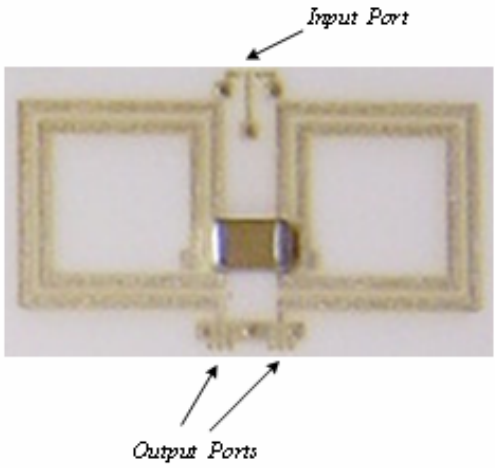

Fig. 6.25: Microphotograph of the fabricated transformer.

Fig. 6.25 shows a microphotograph of the fabricated transformer. The intrinsic area of the transformer is 0.8cm×1.3cm. The width of the gold-traced line is 10mils, the spacing between the turns of the spiral traces is 10mils, and the outer dimension of each spiral trace is 200mils. The distances between the two spiral traces in the upper and lower layers are 55mils and 35 mils, respectively. The height between the upper and lower metallic trace is 7.4mils. The numbers of turns of each spiral trace are 2.

Fig. 6.26 indicates the measured and simulated (with Sonnet and ADS) insertion losses of the transformer. The measured insertion loss is better than -4dB from 5.45GHz to 5.75GHz, with a minimum loss around -3.5dB at the center frequency of 5.6GHz. Fig. 6.27 provides the measured return losses for all the output and input ports of the

transformer. The return loss of the input port, including a minimum -16.3dB point at 5.55GHz, is less than -10dB from 5.5GHz to 5.7GHz. The return losses of the output ports are less than -10dB from 5.4GHz to 5.7GHz. The shift between the measured and simulated results, as shown in Figs. 6.8 and 6.9, is caused by the fabrication tolerances and the non-uniformity of the in-house LTCC fabrication.

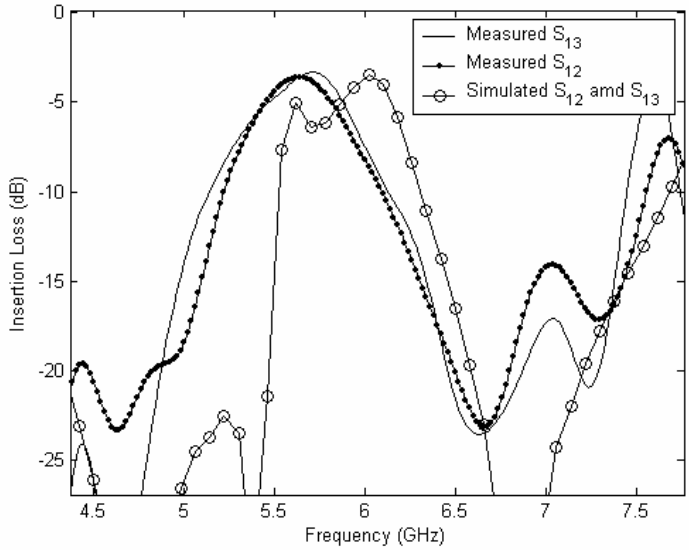

Fig. 6.26: Insertion loss of the transformer.

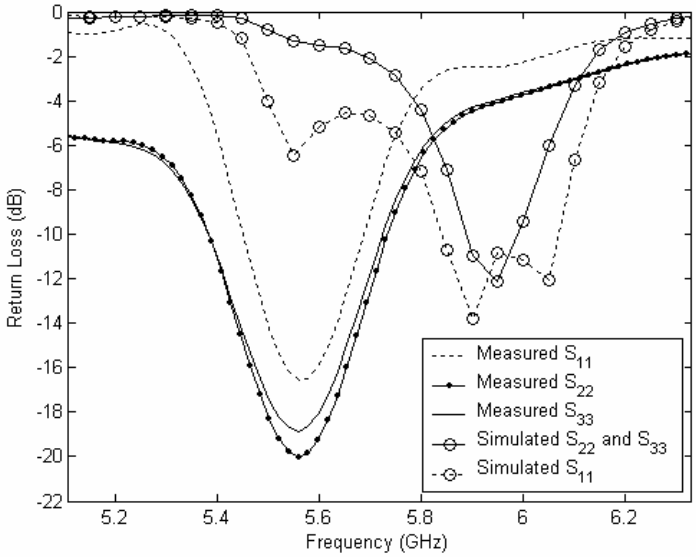

Fig. 6.27: Return loss of the transformer.

Fig. 6.28 gives the phase imbalance between two output ports. As noted from the figure, the phase imbalance is below 10 degrees from 5.18GHz to 6.4GHz.

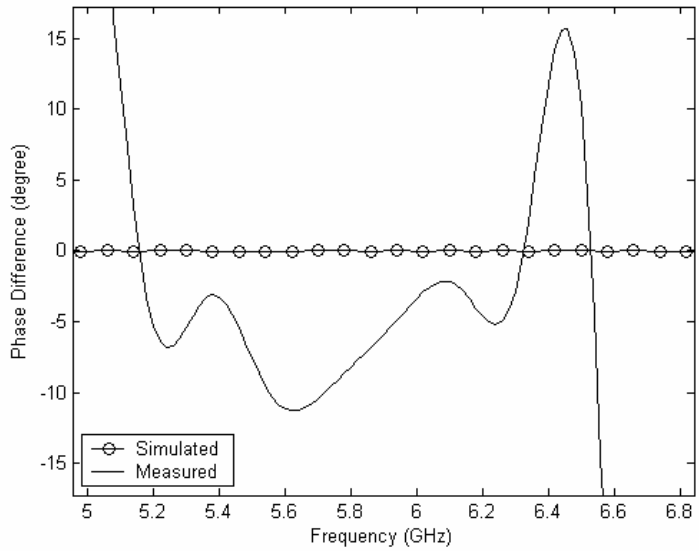

Fig. 6.28: Simulated and measured phase difference of the balanced outputs of the transformer.

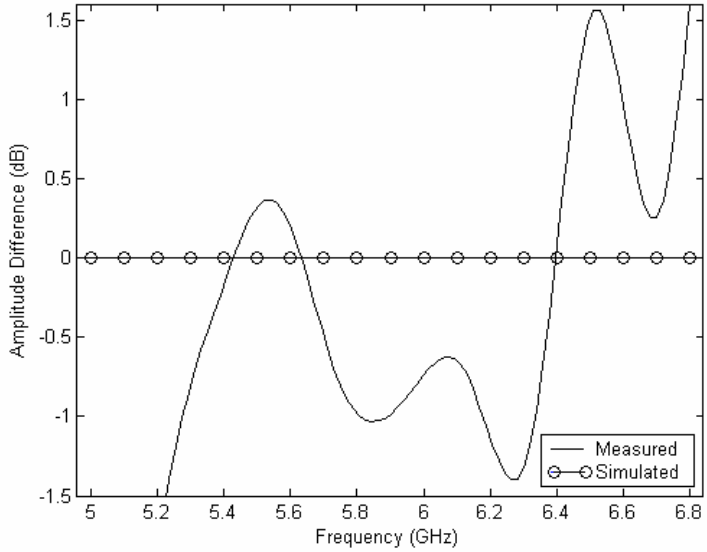

Fig. 6.29: Simulated and measured amplitude difference of the balanced outputs of the transformer.

Fig. 6.29 compares the measured and simulated amplitude imbalance between the two balanced output ports of the transformer. The amplitude imbalance is below 0.5dB from 5.33GHz to 5.7GHz and is below 1dB from 5.27GHz to 6.2GHz.

6.5 Conclusion

In conclusion, the idea of EBG is introduced into the antenna and power divider designs. The experimental results show that the spiral EBG can help to enlarge the bandwidth of the devices. As a result, we achieved a modified triple-band slot antenna and a modified CPW Wilkinson power divider.

In this Chapter, a new type of two-layer LTCC transformer, which is based on the balun network design with minimum phase difference and non-differential outputs, is proposed. A prototype of the proposed transformer was successfully designed in the band 5.45GHz to 5.75GHz. The new transformer can be used for microwave power divider design. As the two branches of transmission lines are wound as spiral metallic traces, this can reduce the fabrication area needed for the device.

CHAPTER 7

CONCLUSIONS AND SUGGESTIONS FOR FUTURE WORKS

7.1 Conclusions

In this thesis, the detailed characteristics of many general planar spiral inductors, symmetrical spiral inductors, multi-layer spiral inductors, transformers, power dividers, and baluns are investigated.

The non-uniform *B*-field around a spiral inductor will cause eddy current in the metallic trace. The appearance of eddy current will dramatically increase the transmission loss and series resistance of the metallic trace with the increasing of frequency. A new prediction for the series resistance of general microwave spiral inductor, based on the analysis of skin effect and eddy current, is derived in this thesis. This new prediction can provide more accurate frequency-dependent results for the resistance of spiral inductor than the conventional formulae. From these results, we conclude that the resistance of a spiral inductor is approximately proportional to ω^2 at low frequencies when the skin depth δ is much larger than the metal thickness *T*, and is approximately proportional to

$\omega^{1.5}$ at high frequencies when δ is much smaller than *T*. Furthermore, two innovative circuit models, which include the eddy current effects on the resistance of the spiral inductor, are obtained. Through the de-embedding technique, the measured *S*-parameters and series resistances of spiral inductors are in good agreement with our theoretical predictions.

The overall inductance of the spiral inductor can be separated into two parts, namely, the self- and mutual inductances. Based on the fundamental formulae of inductance calculations given by Grover [58], the inductance calculations of spiral inductors with non-uniform current distributions in the metallic trace have also been derived in Chapter 3. Through the detailed investigation, we found that both skin effect and eddy current in the metal cannot cause significant changes on the total external inductance of spiral inductors with the increasing of frequency. However, the internal inductances of inductor metallic trace and ground will decrease as functions of frequency; and further deviation of the inductance with frequency may be caused due to the eddy current in the substrate. For most spiral inductor simulations and measurements, the overall inductance of the spiral inductor is usually an increasing function of frequency. But in reality, it will be a decreasing function of frequency once it is computed by subtracting the effect of the parasitic capacitance in the measured *S*-parameters.

In the inductance calculation of the spiral inductor, two different improved methods, based on the magnetic flux and magnetic energy respectively, are also derived and compared with each other. The results of these two methods are found to be quite similar

in the inductance calculations for non-uniform current distribution cases. The measured data are in good agreement with the computed ones.

This thesis also studies the physical meaning of the quality factor *Q* and provides detailed interpretations of the *Q*-factors of symmetrical spiral inductors in Chapter 4. Compared with the non-symmetrical structure, symmetrical octagonal spiral inductor can reduce the coupling capacitance from the overlaps of the metallic traces. This results in an increase of the *Q*-factor of symmetrical spiral inductor. Furthermore, the concept of electric and magnetic center (EMC) is introduced in this chapter. As the EMC of the symmetrical case is the accurate geometric center of the spiral inductor which balances the effect of inductance coupling between different parts of the inductor, we can achieve high *Q*-factor and high resonance frequency from the symmetrical inductor structure. These theories are confirmed by the simulation results.

Improved analysis of the eddy current in the substrate of multi-layer spiral inductors is undertaken in Chapter 5. The effects of eddy current in the substrate of multi-layer spiral inductor are assumed to be more significant than those of the single layer case. Both the magnetic fields and the induced eddy current are found to be proportional to the excitation current in the metallic trace of spiral inductor. As such, there exists a mutual coupling factor, which can be denoted as *M* between the current flowing in the two sandwiched metallic layers and the eddy current in the substrate. Based on the previous consideration for the eddy current in the substrate, another new and more accurate circuit

model with the coupling factor *M* for the multi-layer inductors is derived. Better simulation results are achieved with our new model from the experimental data.

In Chapter 6, we introduce the idea of EBG into the antenna and power divider designs. The experimental results show that the spiral EBG can help to enlarge the bandwidth of the devices. As a result, we achieved a modified triple-band slot antenna and a modified CPW Wilkinson power divider. The measured insertion loss of the divider is better than -3.5dB from 1.2GHz to 2.2GHz and the bandwidth is 58.8% centered at 1.7GHz. The measured return losses of the divider are less than -10dB from 0.4GHz to 2.6GHz for the input port and from 0.2GHz to 2.15GHz for the two output ports.

In addition, with a type of special structure of spiral metallic traces as explained in Chapter 6, we finally design a new LTCC transformer which provides one pair of well-balanced and non-differential signals in this thesis. The measured insertion loss of the transformer is better than -4dB from 5.45GHz to 5.75GHz, with a minimum loss around -3.5dB at the center frequency 5.5GHz. The return loss of the transformer's input port, including a minimum -16.3dB point at 5.55GHz, is less than -10dB from 5.5GHz to 5.7GHz. The return losses of the output ports are less than -10dB from 5.4GHz to 5.7GHz. Compared with the conventional baluns used for microwave mixers and phase shifters, this type of transformer can be used to fabricate microwave dividers and combiners. Excellent balance performances are achieved for both the amplitude and the phase of the signals. The design is verified experimentally in Chapter 6.

7.2 Recommendations and Suggestions for Future Works

In the metallic trace of spiral inductors, the phase difference between the eddy current and excitation current is temporarily considered by us to be constant 90°. But for detailed consideration, the excitation current is delayed by the spiral inductance in its proceeding through the metal and it should have different phases in different turns of the inductor. As for a multiturn spiral inductor, the *B*-field at turn *n* is the superposition of *B*-fields from all turns, the phases of both their induced *B*-fields and the eddy current in the second-order estimations will be changed (although the most significant effect on the induced *B*-field in the *n*-th turn is from the excitation current in the *n*-th turn itself). So more precisely speaking, if the eddy current is no longer in quadrature with the excitation current, they may provide their extra contributions to the overall inductance of the inductor with the change of frequency. With these considerations, more accurate predictions on the inductance of spiral inductors should be achieved.

In addition, as *B*-field and the eddy current in the substrate usually affect the inductance and resistance of spiral inductor significantly, more attentions should be paid to the CMOS substrate effects on the series resistance, inductance, and capacitances of the inductor network. Relative discussions are proposed in Chapter 3.

More experimental data are needed to confirm our theory of high-*Q* symmetrical octagonal spiral inductors proposed in Chapter 4. Relative designs and further analysis shall be done in the future work.

On the basis of this thesis, more full-wave methods or EM simulations are still needed in the simulations and optimizations for different kinds of spiral inductors, transformers, and baluns. Proper combinations of the full-wave and circuit methods are quite important for all the MMIC studies and designs.

Finally, as the symmetrical spiral inductors can sometimes provide high *Q*s and high resonance frequencies. There is a good motivation for us to combine the symmetrical-structured spiral traces into the transformer and power divider design (as illustrated in Chapter 6). With the concept of well-balanced EMC in the geometric center of the metallic traces, this new structure should be able to provide lower insertion losses, lower return losses, and wider bandwidth for the microwave divider or combiner design.

REFERENCES

[1] B. H. Park and P. E. Allen, "Low-power, low-phase-noise CMOS voltage controlled oscillator with integrated *LC* resonator," *Proc. ISCAS'98*, vol. 4, Monterey, pp. 421-424, June 1998.

[2] W. B. Kuhn and N. M. Ibrahim, "Analysis of current crowding effects in multiturn spiral inductor," *IEEE Trans. Microwave Theory and Tech.*, vol. 49, no. 1, pp. 31-38, Jan. 2001.

[3] A. Zolfaghari, A. Chan, and B. Razavi, "Stacked inductors and transformers in CMOS technology," *IEEE J. Solid-State Circuits*, vol. 36, no. 4, pp. 620-628, Apr. 2001.

[4] Y. Papananos and Y. Kousoyannopoulos, "Efficient utilization of on-chip inductors in silicon RF IC design using a novel CAD tool; the LNA paradigm," *Proc. ISCAS'98*, vol. 6, Monterey, CA, pp. 118-121, June 1998.

[5] H. Ainspan, M. Soyuer, J. Plouchart, and J. Brughartz, "A 6.25-GHz low DC power low-noise amplifier in SiGe," *Proc. CICC 1997*, pp. 177-180, 1997.

[6] C. P. Yue and S. S. Wong, "On-chip spiral inductors with patterned ground shields for Si-based RF IC's," *IEEE J. Solid-State Circuits*, vol. 33, no. 5, pp. 743-752, May 1998.

[7] J. Y. C. Chang, A. A. Abidi, and M. Gaitan, "Large suspended inductors on silicon and their use in a $2-\mu m$ CMOS RF amplifier," *IEEE Electron Device Lett.*, vol. 4, pp. 246-248, May 1993.

[8] J. Brughartz, D. Edelstein, K. Jenkins, and Y. Kwark, "Spiral inductors and transmission lines in silicon technology using copper-damascene interconnects and low-loss substrate," *IEEE Trans. Microwave Theory Tech.*, vol. 45, pp. 1961-1968, Oct. 1997.

[9] T. Gokdemir, U. Karacaoglu, D. Budimir, S. Economides, A. Khalid, A. Rezazadeh, and I. Robertson, "Multilayer passive components for uniplanar Si/SiGe MMICs," *Proc. Dig. 1997 IEEE RFIC Symp.*, Denver, CO, June 1997.

[10] J. Burghartz, A. Ruehli, K. Jenkins, M. Soyuer, and D. Nguyen-Ngoc, "Novel substrate contact structure for high-*Q* silicon-integrated spiral inductors," *Proc. Tech. Dig. 1997, Int. Electron Devices Mtg.*, Washington, DC, pp. 55-58, Dec. 1997.

[11] M. Park, C. S. Kim, J. M. Park, H. K. Yu, and K. S. Nam, "High *Q* microwave inductors in CMOS double-metal technology and its substrate bias effects for 2 GHz RF

IC's applications," *Proc. Tech. Dig. 1997, Int. Electron Devices Mtg.,* Washing, DC, pp. 55-58, Dec. 1997.

[12] D. Pehlke, A. Burstein, and M. Chang, "Extremely high-*Q* tunable inductor for Si-based RF integrated circuit applications," *Proc. Tech. Dig. 1997, Int. electron Devices Meeting,* Washington, DC, pp. 55-58, Dec. 1997.

[13] I. Huynen, " Novel fast multiline analysis of parasitic effects in CPW inductors for MMIC's," *IEEE Microwave Guided Wave Lett.,* vol. 8, pp. 72-72, Feb. 1998.

[14] S. W. Paek and K. S. Seo, "Air-gap stacked spiral inductor," *IEEE Microwave Guided Wave Lett.,* vol. 7, pp. 329-330, Oct. 1997.

[15] L. Zu, Y. Lu, R. C. Frye, M. Y. Lau, S. S. Chen, D. P. Kossives, J. Lin, and K. L. Tai, "High *Q*-factor inductors integrated on MCM Si substrates," *IEEE Trans. Comp., and Manufact. Tech.-Pt. B,* vol. 19, pp. 635-642, Aug. 1996.

[16] M. Park, S. Lee, H. K. Yu, J. G. Koo, and K. S. Nam, "High *Q* CMOS-compatible microwave inductors using double-metal interconnection silicon technology," *IEEE Microwave Guided Wave Lett.,* vol. 7, pp. 45-47, Feb. 1997.

[17] R. B. Merrill, T. W. Lee, H. You, R. Rasmussen, and L. A. Moberly, "Optimization of high *Q* integrated inductors for multi-level metal CMOS," *Dig. 1995 Int. Electron Devices Meeting,* pp. 983-986, Dec. 1995.

[18] S. Pipolos, Y. Tsividis, J. Fenk, and Y. Papanaons, "A Si 1.8 GHz RLC filter with tunable center frequency and quality factor," *IEEE J. Solid-State Circuits,* vol. 31, pp. 1517-1525, Oct. 1996.

[19] A. C. Reyes, S. M. El-Ghazaly, S. Dorn, M. Dydyk, D. K. Schroder, and H. Patterson, "Coplanar waveguides and microwave inductors on silicon substrates," *IEEE Trans. Microwave Theory Tech.,* vol. 43, pp. 2016-2022, Sept. 1995.

[20] R. Groves, D. L. Harame, and D. Jadus, "Temperature dependence of *Q* and inductance in spiral inductors fabricated in a silicon-germanium/BiCMOS technology," *IEEE J. Solid-State Circuit,* vol. 32, pp. 1455-1459, Sept. 1997.

[21] B. Razavi, "CMOS technology characterization for analog and RF design," *Proc. CICC'98,* Santa Clara, CA, pp. 23-30, May 1998.

[22] J. Craninckx and M. Steyaert, "A 1.8-GHz low-phase-noise CMOS VCO using optimized hollow spiral inductors," *IEEE J. Solid-State Circuits,* vol. 32, pp. 736-744, May 1997.

[23] J. Brughartz, M. Soyuer, and K. Jenkins, “Microwave inductors and capacitors in standard multilevel interconnect silicon technology,” *IEEE Trans. Microwave Theory Tech.,* vol. 44, pp. 100-104, Jan. 1996.

[24] M. Park, S. Lee, C. S. Kim, H. K. Yu, and K. S. Nam, “The detailed analysis of high *Q* CMOS-compatible microwave spiral inductors in silicon technology,” *IEEE Trans. Electron Devices,* vol. 45, pp. 1953-1959, Sept. 1998.

[25] Y. Xie, M. R. Frei, A. J. Becker, C. A. King, D. Kossives, L. T. Gomez, and S. K. Theiss, “An approach for fabricating high-performance inductors on low-resistivity substrates,” *IEEE J. Solid-State Circuits,* vol. 33, pp. 1433-1438, Sept. 1998.

[26] B. K. Kim *et al.*, “Monolithic planar RF inductor and waveguide structures on silicon with performance comparable to those in GaAs MMIC,” *IEDM Tech. Dig.*, pp. 717-720, Dec. 1995.

[27] J. N. Burghartz, M. Soyuer, and K. A. Jenkins, “Integrated RF and Microwave Components in BiCMOS Technology,” *IEEE Trans. Electron Devices,* vol. 43, no. 9, pp. 1559-1570, September 1996.

[28] M. Park *et al*., “High *Q* microwave inductors in SMOS double-metal technology,” *IEDM Tech. Dig.,* pp. 59-62, Dec. 1997.

[29] D. Lovelace, N. Camilleri, and G. Kannell, “Silicon MMIC inductor modeling for high volume, low cost applications,” *Microw. J.*, pp. 60-71, Aug. 1994.

[30] K. B. Ashby, I. A. Koullias, W. C. Finley, J. J. bastek, and S. Moinian, “High Q inductors for wireless applications in a complementary silicon bipolar process,” *IEEE J. Solid-State Circuits,* vol. 31, no. 5, pp. 4-9, 1996.

[31] J. Crols, P. Kinget, J. Craninckx, and M. S. J. Steyaert, “An analytical model of planar inductors on lowly doped silicon substrates for high frequency analog design up to 3 GHz,” *1996 Symp. VLSI Circuits Dig. Tech. Papers,* pp. 28-29, June 1996.

[32] J. R. Long and M. A. Copeland, “The modeling, characterization, and design of monolithic inductors for silicon RF IC’s,” *IEEE J. Solid-State Circuits,* vol. 32, no. 3, pp. 357-369, March 1997.

[33] A. M. Niknejad and R. G. Meyer, “Analysis and optimization of monolithic inductors and transformers for RF ICs,” *Proc. IEEE 1997 Custom Integrated Circuits Conf.,* pp. 375-378, May 1997.

[34] R. D. Lutz et al., “Modeling of spiral inductors on lossy substrates for RFIC applications,” *Proc. 1998 Radio Frequency Integrated Circuits Symp.,* pp. 313-316, June 1998.

[35] J. Lescot, J. Haidar, and F. Ndagijimana, "Accurate and fast modeling of planar inductors in CMOS technologies," *Proc. 29th Eur. Solid State Device Research Conf.*, Sept. 1999.

[36] H. Heeb and A. E. Ruehli, "Three-dimensional interconnect analysis using partial element equivalent circuits," *IEEE Trans. Circuit and System—1: Fundamental Theory and Applications*, vol. 39, no. 11, pp. 974-982, Nov. 1992.

[37] A. E. Ruehli, "Equivalent circuit models for three dimensional multiconductor system," *IEEE Trans. Microwave Theory Tech.*, vol. MTT-22, pp. 216-221, Mar. 1974.

[38] Z. Yaojiang, L. Haibo, and F. Zhenghe, "Calculation of RF-MEMS inductors using partial element equivalent circuits," *2000 2nd International Conference on Microwave and Millimeter Wave Technology Procedings*, pp. 391-394, 2000.

[39] K. Y. Su and J. T. Kuo, "Analytical evaluation of inductance of spiral inductors using partial equivalent circuit (PEEC) Technique," *IEEE*, pp. 364-367, 2000.

[40] C. P. Yue *et al*., "A physical model for planar spiral inductors on silicon," *IEDM Tech. Dig.*, pp. 155-158, Dec. 1996.

[41] C. P. Yue and S. S. Wong, "Physical modeling of spiral inductors on silicon," *IEEE Trans. Electron Devices,* vol. 47, no. 3, pp. 560-568, Mar. 2000.

[42] P. Arcioni, R. Castello, L. Perregrini, E. Sacchi, and F. Svelto, "An innovative modelization of loss mechanism in silicon integrated inductors," *IEEE Trans. Circuits and Systems-II: Analog and Digital Signal Processing*, vol. 46, no. 12, pp. 1453-1460, Dec. 1999.

[43] B. L. Ooi, D. X. Xu, P. S. Kooi, and F. J. Lin, "An improved prediction of series resistances in spiral inductor modeling with eddy current effect," *IEEE Trans. Microwave Theory Tech.,* vol. 50, no. 9, pp. 2202-2206, Sep. 2002.

[44] D. X. Xu, B. L. Ooi, P. S. Kooi, and F. J. Lin, "Spiral inductor modeling with improved prediction on series resistance due to eddy current effect," *Proc. Asia Pacific Microwave Conference 2002* (in CD-format), Nov. 2002.

[45] H. S. Tsai, J. Lin, R. C. Frye, K. L. Tai, M. Y. Lau. D. Kossives, E. HHryeenko, and Y. K. Chen, "Investigation of current crowding effect on spiral inductors," *Proc. IEEE MTT-S Int. Topical Symp, Technologies for Wireless Applications*, pp. 139-142, 1997.

[46] A. M. Niknejad and R. G. Meyer, "Analysis, design, and optimization of spiral inductors and transformers for Si RF IC's," *IEEE J. Solid-State Circuits*, pp. 1470-1481, 1998.

[47] N. M. Nguyen and R. G. Meyer, “Si IC-compatible inductors and LC passive filters,” *IEEE J. Solid-State Circuit,* pp. 1028-1031, Aug. 1990.

[48] C. P. Yue, C. Ryu, J. Lau, T. H. Lee, and S. S. Wong, “A physical model for planar spiral inductors on silicon,” *Proc. IEEE Int. Electron Devices Meetings,* pp. 155-158, 1996.

[49] W. B. Kuhn and N. K. Yanduru, “Spiral inductor substrate loss modeling in silicon RFICs,” *Microwave J.*, pp. 66-81, Mar. 1999.

[50] E. Mernyei, E. Darrer, M. Pardoen, and A. Sibrai, “Reducing the substrate losses of RF integrated inductors,” *IEEE Microwave Guided Wave Lett.,* pp. 300-301, 1998.

[51] W. B. Kuhn and N. K. Yanduru, “Spiral inductor substrate loss modeling in silicon RFICs,” *Proc. IEEE Radio Wireless Conf.,* pp. 305-308, 1998.

[52] J. N. Burghartz, M. Soyuer, K. A. Jenkins, and M. D. Hulvey, “High-*Q* inductors in standard silicon interconnect technology and its application to an integrated RF power amplifier,” *Proc. Int. Electron Devices Meeting,* pp. 29.8.1-29.8.3, 1995.

[53] R. A. Johnson, C. E. Chang, P. M. Asbeck, M. E. Wood, G. A. gareia, and I. Lagnado, “Comparison of microwave inductors fabricated on silicon-on-sapphire and bulk silicon,” *IEEE Microwave guided Wave Lett.,* pp. 323-325, Sept. 1996.

[54] MayNet *5 user guide: Using the MagNet version 5 package from Infolytica,* E. M. Freeman, Infolytica Corp., Montreal, P. Q., Canada, 1993.

[55] H. M. Greenhouse, “Design of planar rectangular microelectronic inductors,” *IEEE Trans. Parts, Hybrids, Packaging,* vol. PHP-10, pp. 101-109, June 1974.

[56] H. A. Wheeler, “Simple inductance formulas for radio coils,” *Proc. IRE,* vol, 16, no. 10, pp. 29-35, Oct. 1928.

[57] S. S. Mohan, M. M. Hershenson, S. P. Boyd, and T. H. Lee, “Simple accurate expressions for planar spiral inductances,” *IEEE J. Solid-State Circuits,* vol. 34, no. 10, pp. 1419-1424, Oct. 1999.

[58] F. W. Grover, *Inductance Calculation*, New York, NY: Van Nostrand, 1962.

[59] A. E. Ruehli, “Inductance calculations in a complex integrated circuit environment,” *IBM J. Res. Develop.*, vol. 16, pp. 470-481, Sep. 1972.

[60] Ban-Leong Ooi, Dao-Xian Xu, and Li-Hui Guo, “Efficient methods for inductance calculation with special emphasis on non-uniform current distributions,” *Microwave and Optical Technology Letters,* vol. 40, no. 5, pp. 432-436, Mar. 5, 2004.

[61] J. R. Long and M. A. Copeland, "Modeling of monolithic inductors and transformers for silicon RFIC design," *Proc. IEEE MTT-S Int. Symp. Technologies for wireless Applications,* Vancouver, BC, Canada, pp. 129-134, Feb. 1995.

[62] P. Arcioni, R. Castello, G. D. Astis, E. Sacchi, and F. Svelto, "Measurement and modeling of Si integrated inductors," *IEEE Trans. Instrumentation and Measurement*, vol. 47, no. 5, pp. 1372-1378, Oct. 1998.

[63] C. J. Chao, S. C. Wong, C. H. Kao, M. J. Chen, L. Y. Leu, and K. Y. Chiu, "Characterization and modeling of on-chip spiral inductors for Si RFIC's," *IEEE Tran. Semiconductor Manufacturing*, vol. 15, no.1, pp. 19-29, Feb. 2002.

[64] J. N. Burghartz, K. A. Jenkins, and M. Soyuer, "Multilevel-spiral inductors using VLSI interconnect technology," *IEEE Electron Device Letters*, vol. 17, no. 9, pp. 428-430, Sep. 1996.

[65] J. Sieiro, J. M. L. Villegas, J. Cabanillas, J. A. Osorio, and J. Samitier, "A physical frequency-dependent compact model for RF integrated inductors," *IEEE Trans. Microwave Theory Tech.*, vol. 50, no. 1, pp. 384-392.

[66] D. Melendy, P. Francis, C. Pichler, K. Hwang, G. Srinsivasan, and A. Weisshaar, "A new wide-band compact model for spiral inductors in RFICs," *IEEE Electron Device Letters*, vol. 23, no. 5, pp. 273-275, May 2002.

[67] L. Wiemer and R. H. Jansen, "Determination of coupling capacitance of underpass, air bridges and crossing in MICs and MMICs," *Electron. Lett.*, vol. 23, pp. 344-346, Mar. 1987.

[68] M. W. Green *et al.*, "Miniature multilayer spiral inductors for GaAs MMICs," *GaAs IC Symp.*, pp. 303-306, 1989.

[69] S. M. Jenei, B. S. Aleksic, L. D. Zivanov, "Modeling and optimization of multilayer thick film inductor," *Proc. 21st International Conf. on Microelectron CS (MIEL'97), Yugoslavia*, vol. 1, pp. 417-420, Sep. 1997.

[70] G. L. Hui, Y. M. Bin, C. Zhen, H. Han, and Z. Yi, "High *Q* multilayer spiral inductor on silicon chip for 5~6 GHz," *IEEE Electron Device Letters*, vol. 23, no. 8, pp. 470-472, Aug. 2002.

[71] R. D. Lutz, Y. Hahm, A. Weisshaar, V. K. Tripathi, "Modeling and analysis of multilevel spiral inductors for RFIC's," *Tech. Dig. IEEE Int. Microwave Symp.*, pp. 43-46, 1999.

[72] Y. Koutsoyannopoulos, Y. Papananos, S. Bantas, and C. Alemanni, "Performance limits of planar and multilayer integrated inductors," *IEEE Int. Circuits and System*, pp. 160-163, 2000.

[73] B. Breen, “Multi-layer inductor for high frequency applications,” *IEEE*, pp. 551-553, 1991.

[74] J. R. Long and M. A. Copeland, “A 1.9 GHz low-voltage silicon bipolar receiver front-end for wireless personal communication systems,” *IEEE J. Solid-State Circuits*, vol. 30, pp. 1438-1448, Dec. 1995.

[75] Y. Koutsoyannopooulos, Y. Papananos, S. Bantas, and C. Alemanni, “Novel Si integrated inductor and transformer structure for RF IC design,” *Proc. of the 1999 IEEE International Symposium on Circuits and Systems*, pp. 573-576, 1999.

[76] S. G. Lee, G. J. Ihm, and W. C. Song, “Design and analysis of symmetric dual-layer spiral inductor for RF integrated circuit,” *The First IEEE Asia-Pacific Conference on ASICs*, pp. 5-8, Aug. 1999.

[77] S. J. Pan, L. W. Li, and W. Y. Yin, “Compact equivalent circuit model of two-layer spiral inductors,” *Wiley InterScience*, pp. 148-153, July 2002.

[78] I. J. Bahl, “High current handling capacity multilayer inductors for RF and microwave circuits,” *Int J. RF Microwave CAE*, pp. 139-146, 2000.

[79] Y. Koutsoyannopoulos, *et al.*, “A generic CAD model for arbitrary shaped and multilayer integrated inductors on silicon substrates,” *Proc. ESSDERC*, pp. 320-323, 1997.

[80] K. T. Ng, B. Rejaei, and J. N. Burghartz, “Substrate effects in monolithic RF transformers on silicon,” *IEEE Trans. Microwave Theory Tech.*, vol. 50, no. 1, pp. 377-383, Jan. 2002.

[81] C. P. Yue and S. S. Wong, “A study on substrate effects of silicon-based RF passive components,” *1999 IEEE MTT-S International Microwave Symposium Digest*, pp. 1625-1628, 1999.

[82] K. Schimpf, B. Benna, D. Proetel, “A new approach to characterize substrate losses of on-chip inductor,” *Proc IEEE 2001 Int. Conference on Microelectronic Test Structures*, vol. 14, pp. 115-118, Mar. 2001.

[83] A. M. Niknejad and R. G. Meyer, “Analysis of eddy-current losses over conductive substrates with applications to monolithic inductors and transformer,” *IEEE Trans. Microwave Theory Tech.*, vol. 49, pp. 166-176, Jan. 2001.

[84] J. R. Long, “Monolithic transformers for silicon RF IC design,” *IEEE Journal of Solid Circuits*, vol. 35, no. 9, pp. 1368-1382, Sep. 2000.

[85] N. Marchand, “Transmission-line conversion transformers,” *Electronics*, vol. 17, no. 12, pp. 142-145, 1944.

[86] T. Chen, K. W. Chang, s. B. Bui, H. Wang, G. S. Dow, L. C. T. Liu, T. S. Lin, and W. S. Titus, “Broad-band monolithic passive baluns and monolithic double-balance mixer,” *IEEE Trans. Microwave Theory Tech.*, vol. 39, pp. 1980-1986, Dec. 1991.

[87] S. A. Maas and K. C. Chen, “A broad-band, planar, doubly balanced monolithic *Ka*-band diode mixer,” *IEEE Trans. Microwave Theory Tech.*, vol. 41, pp. 2330-2335, Dec. 1993.

[88] A. M. Pavio and A. Kikel, “A monolithic or hybrid broadband compensated balun,” *MTT-S*, pp. 483-486, 1990.

[89] W. R. Brinlee, A. M. Pavio, and K. R. Varian, “A novel planar double-balanced 6-18GHz MMIC mixer,” *IEEE International Microwave Symposium Digest*, pp. 9-12, 1993.

[90] M. C. Tsai, M. J. Schindler, W. Struble, M. Ventresca, R. binder, R. Waterman, and D. Danzilio, “A compact wideband balanced mixer,” *IEEE International Microwave Symposium Digest*, pp. 5-8, 1994.

[91] K. S. Ang and I. D. Robertson, “Analysis and design of impedance-transforming Marchand balun,” *IEEE Trans. Microwave Theory Tech.*, vol. 49, pp. 402-405, Feb. 2001.

[92] C. M. Tsai and K. C. Gupta, “A generalized model for coupled lines and its applications to two layer planar circuit,” *IEEE Microwave Theory Tech.*, vol. 20, pp. 2190-2199, Dec. 1992.

[93] E. Wilkinson, “An N-way hybrid power divider,” *IRE Trans. Microwave Theory Tech.*, vol. MTT-8, pp. 116-118, Jan. 1960.

[94] J. E. Garrett, A. E. Ruehli, and C. R. Paul, “Accurary and stability improvement of integral equation models using the partial element equivalent circuit approach,” *IEEE Trans. Antennas Propagat.*, vol. 46, no. 12, pp. 1824-1832, Dec. 1998.

[95] J. F. Janak, D. D. Ling, and H. M. Huang, “C3DSTAR: A 3D wiring capacitance calculator,” *Proc. IEEE Int. Conf. Computer-Aided Design*, pp. 530-533, 1989.

[96] P. K. Wolff and A. E. Ruehli, “Inductance computations for complex three dimensional geometries,” *Proc. IEEE Int. Symp. Circuits and Systems*, pp. 16-19, 1981.

[97] C. P. Paul, *Introduction to Electromagnetic Compatibility*. New York: Wiley, 1992.

[98] R. D. Lutz, Y. Hahm, A. Weisshaar, V. K. Tripathi, A. Grzegorek, W. McFarland, “Modeling of spiral inductors on lossy substrates for RFIC,” *IEEE J. MTT-S Dig.*, pp. 1855-1858, May 1998.

[99] A. M. Niknejad, R. Gharpurey, and R. G. Meyer, "Numerically stable Green function for modeling and analysis of substrate coupling in integrated circuits," *IEEE Transactions on Computer-Aided Design of Integrated Circuit and Systems,* vol. 17, pp. 305-315, Apr. 1998.

[100] A. Ruehli, C. Paul, and J. Garrett, "Inductance calculation using partial inductances and macromodels," *1995 IEEE Symposium on Electromagnetic Compatibility,* pp. 23-28, July 1995.

[101] F..B. J. Leferink, "Inductance calculation; method and equations," *1995 IEEE Symposium on Electromagnetic Compatibility,* pp. 16-22, Aug. 1995.

[102] A. Ruehli, C. Paul, and J. Garrett, "Inductance calculations using partial inductances and Macromodels," *1995 IEEE International Symposium,* pp. 23-28, Aug. 1995.

[103] R. A. Pucel, D. J. Masse, and C. P. Hartwig, "Losses in microstrip," *IEEE Trans. Microwave Theory Tech.,* vol. 16, pp. 342-350, June 1968.

[104] R. Faraji-Dana and Y. L. Chow, "The current distribution and ac resistance of a microstrip structure," *IEEE Trans. Microwave Theory Tech.,* vol. 38, pp. 1268-1277, Sept. 1990.

[105] Y. Eo and W. R. Eisenstadt, "High-speed VLSI interconnect modeling based on S-parameter measurements," *IEEE Trans. Comp., Hybrids, Manufact. Technol.,* vol. 16, pp. 555-562, Aug. 1993.

[106] C. L. Holloway and G. A. Hufford, "Internal inductance and conductor loss associated with the ground plane of a microstrip line," *IEEE Trans. Electromagnetic Compatibility*, vol. 39, no. 2, pp. 73-78, May 1997.

[107] B. Mukherjee, L. Wang, and A. Pacelli, "A practical approach to modeling skin effect in on-chip interconnects," *14th ACM GLSVLSI'04*, pp. 266-270, Boston, Massachusetts, USA, April 26-28, 2004.

[108] S. Mei and Y. I. Ismail, "Modeling skin effect with reduced decoupled *R-L* circuits," *Proc. Intl. Symp. on Circuit and Systems (ISCAS),* pp. 588-591, 2003.

[109] B. K. Sen and R. L. Wheeler, "Skin effects models for transmission line structures using generic SPICE circuit simulators," *IEEE 7th topical Meeting on Electrical Performance of Electronic Packaging,* pp. 128-131, Oct. 26-28, 1998.

[110] S. Kim and D. P. Neikirk, "Compact Equivalent circuit model for the skin effect," *1996 IEEE MTT-S Digest,* pp. 1815-1818, 1996.

[111] H. A. Wheeler, “Formulas for the skin effect,” *Proc. IRE*, vol. 30, pp. 412-424, Sept. 1942.

[112] C. S. Yen, Z. Fazarinc, and R. L. Wheeler, “Time-domain skin-effect model for transient analysis of lossy transmission line,” *Proc. IEEE*, vol. 70, pp. 750-757, July 1982.

[113] M. Kamon, M. Tsuk, and J. White, “FASTHENRY: A multipole accelerated 3-D inductance extraction program,” *IEEE Trans. Microwave Theory Tech.*, vol. 42, no. 9, pp. 1750-1758, Sept. 1994.

[114] C.-J. Chao, S.-C. Wong, C.-H. Kao, M.-J. Chen, L.-Y. Leu, and K.-Y. Chiu, “Characterization and modeling of on-chip spiral inductors for Si RFICs,” *IEEE Trans. Semiconductor Manufacturing*, vol. 15, no. 1, pp. 19-29, Feb. 2002.

[115] K. O, “Estimation methods for quality factors of inductors fabricated in silicon integrated circuit process technologies,” *IEEE J. Solid-State Circuits*, vol. 33, pp. 1249-1252, Aug. 1998.

[116] S. Chaki, S. Aono, N. Andoh, Y. Sasaki, N. Tanino, and O. Ishihara, “Experimental study on spiral inductors,” *IEEE MTT-S Int. Microwave Symp. Dig.*, pp. 753-756, June 1995.

[117] A. M. Niknejad, *ASITIC FAQ*.

[118] S. Jenei, B. K. J. C. Nauwelaers, and S. Decoutere, “Physics-based closed-form inductance expressions for compact modeling of integrated spiral inductors,” *IEEE J. Solid-State Circuits*, vol. 37, pp. 77-80, Jan. 2002.

[119] J. N. Burghartz, “Spiral inductors on silicon-status and trends,” *Int. J. RF Microwave Computer-Aided Eng.*, vol. 8, pp. 422-432, Nov. 1998.

[120] J. Y. Park and M. G. Allen, “Packaging-compatible high-*Q* microinductors and microfilters for wireless applications,” *IEEE Trans. Adv. Packag.*, vol. 22, pp. 207-213, May 1999.

[121] S. S. Mohan, M. D. M. Hershensen, S. P. Boyd, and T. H. Lee, “Simple accurate expressions for planar spiral inductors,” *IEEE J. Solid-State Circuits*, vol. 34, pp. 1419-1424, Oct. 1999.

[122] J. S. J. Chen, K. Zhang, M. N. O. Sadiku, and A. A. Tseng, “The electromagnetic enhancement of melt spinning and strip casting,” *JOM-e*, vol. 50, no. 2, Feb. 1998.

[123] J. Tani, M. Minagawa, and K. Ohtomo, “Dynamic behavior of thin plates under impulsive magnetic field,” *IEEE Transactions on Magnetics*, vol. 26, no. 2, pp. 544-547, 1990.

[124] A. R. B. Rocha and H. C. C. Fernandes, "Dynamic method for antennas with PBG," *Twenty Seventh International Conference on Infrared and Millimeter Waves*, pp. 89-90, Sept. 2002.

[125] L. C. Kretly and A. Tavora. A. S., "A PBG-photonic band gap-static phase-shifter for steerable antenna array," *Microwave and Optoelectronics Conference*, vol. 1, pp. 211-214, Sept. 2003.

[126] J. S. Chen, and S. Y. Lin, "Triple-frequency rectangular-ring slot antennas fed by CPW and microstrip line," *Microwave and Optical Technology Letter*, vol. 37, pp. 243-246, May 2003.

[127] D. M. Pozar, *Microwave Eng.*: Addison-Wesley, 1990, pp. 395-399.

[128] K. H. Yi and B. Kang, "Modified Wilkinson power divider for *n*th harmonic suppression," *IEEE Microwave and Wireless Components Letters*, vol. 13, no. 5, pp. 178-180, May 2003.

[129] K. Nishikawa, T. Tokumitsa, I. Toyoda, "Miniaturized Wilkinson power divider using three-dimensional MMIC techonology," *IEEE Microwave and Guided Wave Letters*, vol. 6, no. 10, pp. 372-374, Oct. 1996.

[130] H. Ogawa, T. Hirota, and M. Aikawa, "New MIC power dividers using coupled microstrip-slot lines: Two-sided MIC power dividers," *IEEE Trans. Microwave Theory Tech.*, vol. MTT-33, pp. 1155-1164, Nov. 1985.

[131] K. Shibata, K. Hatori, Y. Tokumitsu, and H. Komizo, "Microstrip spiral directional coupler," *IEEE Trans. Microwave Theory Tech.,* vol. 29, pp. 680-689, July 1981.

[132] S. A. Jamison, A. Podell, M. Helix, P. Ng, and C. Chao, "Inductively coupled push-pull amplifiers for low cost monolithic microwave ICs," *Proc. IEEE GaAs IC Symp.*, pp. 91-93, Oct. 1982.

[133] D. Ferguson, P. Bauhahn, J. Keuper, R. Lokken, J. Culp, C. Chao, and A. Podell, "Transformer coupled high-density circuit technique for MMIC," *Proc. Monolithic Microwave IC Symp.*, pp. 34-36, May 1984.

[134] E. Frlan, S. Meszaros, M. Cuhaci, and J. Wight, "Computer-aided design of square spiral transformers and inductors," *Proc. IEEE MTT-S*, pp. 661-664, June 1989.

[135] A. Boulouard and M. Le Rouzic, "Analysis of rectangular spiral transformers for MMIC applications," *IEEE Trans. Microwave Theory Tech.,* vol. 37, pp. 1257-1260, Aug. 1989.

[136] G. G. Rabjohn, "Monolithic microwave transformers," M.Eng. thesis, Carleton University, Ottawa, ON, Canada, Apr. 1991.

[137] J. R. Long, M. A. Copeland, S. J. Kovacic, D. S. Mahli, and D. L. Harame, "RF analog and digital circuits in SiGe technology," *Proc. ISSCC*, pp. 82-83, Feb. 1996.

[138] J. J. Zhou and D. J. Allstot, "Monolithic transformers and their application in a differential CMOS RF low-noise amplifier," *IEEE J. Solid-State Circuits*, vol. 33, pp. 2020-2027, Dec. 1998.

[139] B. Jansen, K. Negus, and D. Lee, "Silicon bipolar VCO family for 1.1 to 2.2 GHz with full-integrated tank and tuning circuits," *Proc. ISSCC*, pp. 392-393, Feb. 1997.

[140] M. Zannoth, B. Kolb, J. Fenk, and R. Weigel, "A fully integrated VCO at 2 GHz," *IEEE J. Solid-State Circuits*, vol. 33, pp. 1987-1991, Oct. 1998.

[141] J. R. Long and M. Maliepaard, "A 1-V 900-MHz image-reject downconverter in $0.5-\mu m$ CMOS," *Proc. CICC*, pp. 665-668, May 1999.

[142] D. T. S. Cheung, J. R. Long, R. Hadaway, and D. Harame, "Monolithic transformers for Silicon RF IC design," *IEEE Bipolar and BiCMOS Technology Meeting*, pp. 105-108, Sept. 1998.

[143] W. Simbuerger, H. D. Wohlmuth, and P. Weger, "A monolithic 3.7-W Silicon power amplifier with 59% PAE at 0.9 GHz," *Proc. ISSCC*, pp. 230-231, Feb. 1999.

[144] R. Mongia, I. Bahl, and P. Bhartia, *RF and Microwave Coupled-Line Circuits*, Boston, MA: Artech House, 1999, ch. 8.

[145] W. K. Roberts, "A new wide-band balun," *Proc. IRE*, vol. 45, pp. 1628, Dec. 1957.

[146] M. Danesh, J. R. Long, R. A. Hadaway, and D. L. Harame, "A Q-factor enhancement technique for MMIC inductors," *IEEE MTT-S International Microwave Symposium Digest*, pp.183-186, June 1998.

[147] O. M. O. Gatous and J. Pissolato, "Frequency-dependent skin-effect formulation for resistance and internal inductance of a solid cylindrical conductor," *IEE Proc.-Microw. Antennas Propag.*, vol. 151, no. 3, pp. 212-216, June 2004.

[148] H. A. Wheeler, "Transmission-line properties of a strip on a dielectric sheet on a plane," *IEEE Trans. Microwave Theory Tech.*, vol. 25, pp. 631-647, 1977.

[149] F. Lin and G. Kompa, "FET model parameter extraction based on optimization with multiplane data-fitting and bidirectional search-a new concept," *IEEE Trans. Microwave Theory Tech.*, vol. 42, no. 7, pp. 1114-1121, July 1994.